# Natural Circulation Air-Cooled Two-Phase Closed-Loop Thermosyphon Heat Transfer System

by
Taneha Mae Abrahams

*Thesis presented in partial fulfilment of the requirements for the degree of Master of Engineering (Mechanical) in the Faculty of Engineering at Stellenbosch University*


Supervisor: Mr Robert T Dobson

March 2017

## DECLARATION

By submitting this thesis electronically, I declare that the entirety of the work contained therein is my own, original work, that I am the sole author thereof (save to the extent explicitly otherwise stated), that reproduction and publication thereof by Stellenbosch University will not infringe any third party rights and that I have not previously in its entirety or in part submitted it for obtaining any qualification.

Date: .....March 2017.....

## ABSTRACT

Development of a Natural Circulation Air-Cooled Two-phase Closed-Loop Thermosyphon Heat Transfer System

T.M. Abrahams

*Department of Mechanical and Mechatronic Engineering,*
*University of Stellenbosch,*
*Private Bag X1, MATIELAND 7602, South Africa.*

Thesis: MEng Mechanical (Research)

March 2017

This project considers the passive cooling aspects of a small-scale inherently safe, light water, 100 $MW_e$, modular nuclear reactor concept. This concept uses triple containment of the core and consists of three integrated natural circulation loops, namely the primary, secondary and tertiary loops.

The tertiary loop was designed, built, commissioned and tested to measure the temperature and flow rate response at different operating conditions. The tertiary loop functioned successfully with the average heat transfer rate out of the air-cooled condensers measured at 89.5% of the electrical power input into the system. A quasi-steady state, three-dimensional, separated flow, thermal-hydraulic numerical simulation of the tertiary loop system is developed. The numerical simulation captures the thermal-hydraulic behaviour of the working fluid within the tertiary loop well. The temperature response has an average error of 5.73% and the mass flow rate has an average error of 1.86%. The simulation can be used with reasonable certainty to determine the behaviour of the tertiary loop for various input values.

A steady state numerical simulation model of the primary, secondary and tertiary loops operating together was developed to predict the behaviour of the complete passive cooling system and shows encouraging results. The passive cooling concept can now be scaled to the dimensions of a full size nuclear reactor plant and its thermal-hydraulic behaviour confidently determined using the simulation models developed.

## UITTREKSEL

Ontwikkeling van 'n Natuurlike Sirkulasie Lugverkoelde Twee-fase Geslotelus Termoheweleffek Warmteoordrag Sisteem

T.M. Abrahams

*Departement Meganiese en Megatroniese Ingenieurswese,*
*Universiteit van Stellenbosch,*
*Private Bag X1, MATIELAND 7602, South Africa.*

Proefskrif: MEng Mechanical (Navorsing)

Maart 2017

Hierdie projek neem in ag die passiewe verkoelings aspekte van 'n kleinskaalse inherent veilige, ligte water, 100 MWe, modulêre kernreaktor konsep. Hierdie konsep gebruik drie-dubbele inperking van die kern en bestaan uit drie geïntegreerde natuurlike sirkulasie kringlope, naamlik die primêre, sekondêre en tersiêre sirkelroetes.

Die tersiêre lus is ontwerp, gebou, inwerking gestel en getoets om die temperatuur en vloeitempo reaksie op verskillende bedryfstoestande te meet. Die tersiêre lus het suksesvol gefunksioneer met die gemiddelde warmteoordrag uitdie tersiêre lus gemeet teen 89,5% van die elektriese krag wat tot die sisteem toe gevoeg word. 'n Kwasi-gestadigde omgewing, drie-dimensionele, geskeide-vloei, termo-hidrouliese numeriese simulasie van die tersiêre lus stelsel is ontwikkel. Die numeriese simulasie voorspel die termo-hidrouliese gedrag van die werksvloeistof binne die tersiêre lus goed. Die temperatuur reaksie het 'n gemiddelde fout van 5.73% en die massa vloeitempo 1.86%. Die simulasie kan dus gebruik word met redelike sekerheid om die gedrag van die tersiêre lus met verskillende insetwaardes te bepaal.

'n Bestendige toestand numeriese simulasie model van die gekombineerde primêre, sekondêre en tersiêre kringlope is ontwikkel om die gedrag van die volledige passiewe verkoeling stelsel te voorspel. Hierdie simulasie model toon bemoedigende resultate. Die passiewe verkoeling konsep kan nou opgeskaal word teen die afmetings van 'n volskaal kernreaktor en sy termo-hidrouliese gedrag kan met vertroue deur bepaal word die gebruik van die simulasie modelle.

## ACKNOWLEDGEMENTS

I would like to acknowledge the following students for their contribution to this body of work: Constant Waal, Karl Loubser, Kyle Davis and Reeve Duligal.

I would like to thank the employees of the Mechanical and Mechatronic Engineering Department at Stellenbosch University, specifically:

Anton van den Berg for his expertise and advice in the manufacture of the experimental set up.

Ferdi Zietsman and Cobus Zietsman for their technical expertise and assistance in the manufacture and assembly of the experimental set up.

Julian Stanfliet, Nathi Hlwempu and Onalena Motsuminyane for their assistance during the assembly, calibration and testing of the experimental set up.

I would like to thank my supervisor, Mr Dobson for his guidance, expertise, patience and support throughout the project and for his financial support of this research.

I would like to acknowledge the National Research Foundation for their contribution towards financing this research.

I would like to thank Déilen Hans, Kieran Cairncross and Beverley Abrahams for their support, encouragement and appraisal on the production of this report.

# TABLE OF CONTENTS

## LIST OF FIGURES

Page

## LIST OF TABLES

Page

## NOMENCLATURE

### ACRONYMS

| | |
|---|---|
| BWR | Boiling water reactor |
| CDI | Compound dynamic instabilities |
| DWO | Density wave oscillations |
| FDI | Fundamental dynamic instability |
| FNR | Fast neutron reactor |
| GHG | Greenhouse gas |
| IAEA | International Atomic Energy Agency |
| IMR | Pressurised water reactor |
| IRP | Integrated resource plan |
| LWR | Light water reactor |
| MSR | Molten salt reactor |
| NCL | Natural circulation loop |
| PCU | Power conversion unit |
| PDO | Pressure drop oscillations |
| PWR | Pressurised water reactor |
| RES | Renewable energy sources |
| SMR | Small and medium reactors |

### SYMBOLS

| | |
|---|---|
| $A$ | Area, $m^2$ |
| $C_f$ | Friction coefficient |
| $C_p$ | Specific heat at constant pressure, J/kg K |
| $d$ | Diameter, m |
| $g$ | Gravity, $m/s^2$ |
| $h$ | Heat transfer coefficient, $W/m^2.K$, enthalpy, J/kg |
| $k$ | Thermal conductivity, $W/m^2$ K |
| $l$ | Length, m |
| $m$ | Mass, kg |
| $\dot{m}$ | Mass flow rate, kg/s |
| $\dot{m}'''$ | Mass flow rate per unit volume, $kg/m^3$ s |
| $N$ | Number of control volumes |
| $Nu$ | Nusselt number |
| $P$ | Pressure, Pa |
| $Pr$ | Prandlt number |
| $\dot{Q}$ | Heat transfer rate, W |

| | |
|---|---|
| $\dot{Q}'''$ | Heat transfer rate per unit volume, W/m$^3$ |
| $R$ | Thermal resistance, K/W |
| $Ra$ | Raleigh number |
| $Re$ | Reynolds number |
| $S$ | Source term |
| $s$ | Fin spacing, m |
| $T$ | Temperature,˚C |
| $u$ | Internal energy, J/kg |
| $v$ | Velocity, m/s |
| $V$ | Volume, m$^3$, Voltage, V |
| $W$ | Work done, J |
| $x$ | Mass fraction |

## GREEK SYMBOLS

| | |
|---|---|
| $\alpha$ | Void fraction |
| $\beta$ | Volume expansion coefficient, K$^{-1}$ |
| $\delta$ | Length of control volume, m |
| $\theta$ | Angle, ° |
| $\mu$ | Dynamic viscosity, Pa s |
| $\nu$ | Kinematic viscosity, N s/m kg |
| $\rho$ | Density, kg/m$^3$ |
| $\sigma$ | Surface tension |
| $\tau$ | Shear stress, Pa |
| $\varphi$ | Condenser angle, ° |
| $\Phi$ | Frictional multiplier |
| $\eta$ | Efficiency |

## SUBSCRIPTS

| | |
|---|---|
| $a$ | Air |
| $a$ | Axial |
| $c$ | Condenser |
| $cond$ | Conduction |
| $dc$ | Downcomer |
| $e$ | Evaporator, east |
| $elec$ | electrical |
| $env$ | Environment |
| $evap$ | Evaporation |

| | |
|---|---|
| $f$ | Friction |
| $fin$ | fin |
| $ft$ | Flash tube |
| $g$ | Gaseous |
| $h$ | hydraulic |
| $h$ | Heat transfer coefficient |
| $h$ | Hoop |
| $hp$ | Heat pipe |
| $i$ | Inner |
| $l$ | Liquid |
| $L$ | length |
| $lo$ | Liquid only |
| $o$ | Outer |
| $p$ | primary |
| $p$ | Pressure |
| $s$ | Secondary |
| $sd$ | Steam drum |
| $t$ | Tertiary, thermal |
| $tot$ | total |
| $U$ | Overall heat transfer coefficient |
| $w$ | West, wall |
| $x$ | Flow direction |
| $y$ | Flow direction |
| $z$ | Flow direction |

# 1 INTRODUCTION

Population growth and the resultant demand on energy cannot be met by today's electricity production methods without serious long-term consequences to the environment. Nuclear energy produces the largest share of electricity by non-greenhouse-gas (GHG)-emitting sources. This project develops a heat removal system for a modular nuclear reactor that has passive, transparent safety features that are easily understood by non-experts. This would result in better accident management, minimal consequences and an elimination of the need for off-site emergency response through prevention of a reactor meltdown. Development of such a system could lead to greater acceptance of nuclear power plants by the public, leading to greater application and reduced dependence on GHG producing power sources.

## 1.1 BACKGROUND AND MOTIVATION

The report from Generation IV International Forum (2002) determined that clean, safe and cost-effective energy production sources are needed for global sustainability, and that nuclear energy is a viable approach. To develop nuclear energy systems for future use, ten countries, including South Africa, came together in the year 2000 to agree on a framework for international cooperation. This Generation IV roadmap aims to provide competitively priced and reliable nuclear systems (Generation IV International Forum, 2004). The different generations of nuclear reactors are shown along a timeline in Figure 1.

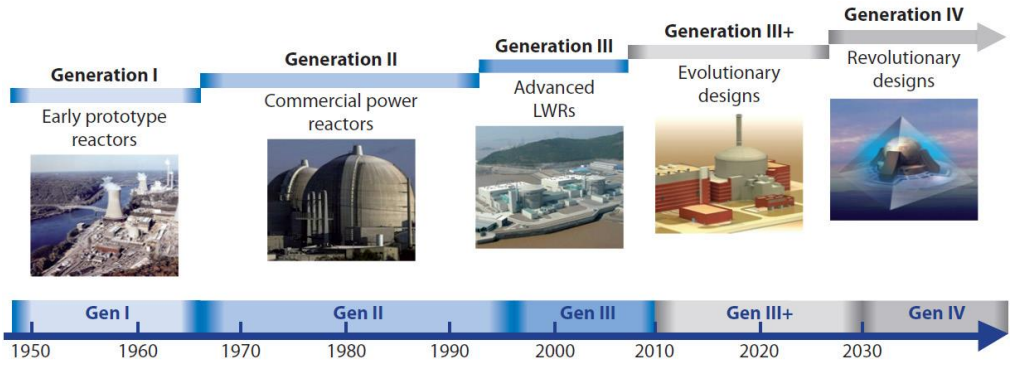


**Figure 1:** Generations of nuclear power stations
(Generation IV International Forum, 2004)

Generation I reactors are the early prototype reactors. They preceded the large commercial power plants that are still operative today, known as Generation II reactors. Generation III reactors have a number of progressive design features that offer substantial advances in safety and economics compared to generation II reactors. Improvements to these have resulted in a group of plants, labelled Generation III+. Generation IV systems, envisioned for future use, will provide

reliable energy products while satisfactorily addressing public perception concerns. These have the following objectives (Generation IV International Forum, 2004):

- To deliver sustainable energy production by using fuel effectively.
- To minimise radioactive waste.
- To have an apparent cost advantage over other power production systems.
- To have similar levels of financial risk as other power production systems.
- To have excellent safety and reliability of the operating system.
- To have a low chance of reactor core damage.
- To have no need for offsite emergency response.
- To provide increased resistance against the production and diversion of weapons grade nuclear material.

In 2010, the Inter-Ministerial Committee on Energy of South Africa tabled the Integrated Resource Plan (IRP). In an attempt to limit GHG emissions, there is a plan to shift the base load away from coal to nuclear, gas, solar and wind. They plan to build an additional 9.6 GW of nuclear power by 2020, allowing nuclear energy to be the base load option from 2023 onwards. Accordingly, development of local knowledge in the relevant technologies is necessary for the success of the IRP (RSA Department of Energy, 2010).

In 2012, a new concept was proposed at Stellenbosch University to cater for the energy needs in South Africa while adhering to the Generation IV objectives. It utilises an inherently safe, natural circulation, flash-tube type system for reactor cavity cooling and steam generation in a nuclear plant, as shown in Figure 2. The concept at Stellenbosch University was based on the GYSER concept by Vécsey and Doroszlai (1988), Yadigaroglu, and Zeller (1994).

The system concept has triple containment of the reactor core and three integrated loops that facilitate heat transfer from the core to either the Power Conversion Unit (PCU) or heat removal system. The three levels of containment are the TRISO® type fuel itself, the primary loop and the steel enclosure. They prevent the release of radiation into the environment. The three loops operate as thermosyphons and are namely the primary loop, secondary loop and tertiary loops.

A system such as this, which makes use of natural forces such as gravity and convection, is considered passive. Not being reliant on mechanical devices, such as pumps to circulate the working fluid, results in simpler designs and improved economics. The resulting system can cool a nuclear reactor in the event of a power failure. The driving forces that cause fluid flow in passive systems are weak, therefore, careful design and analysis of the systems is necessary to ensure they function as intended (IAEA, 2009).

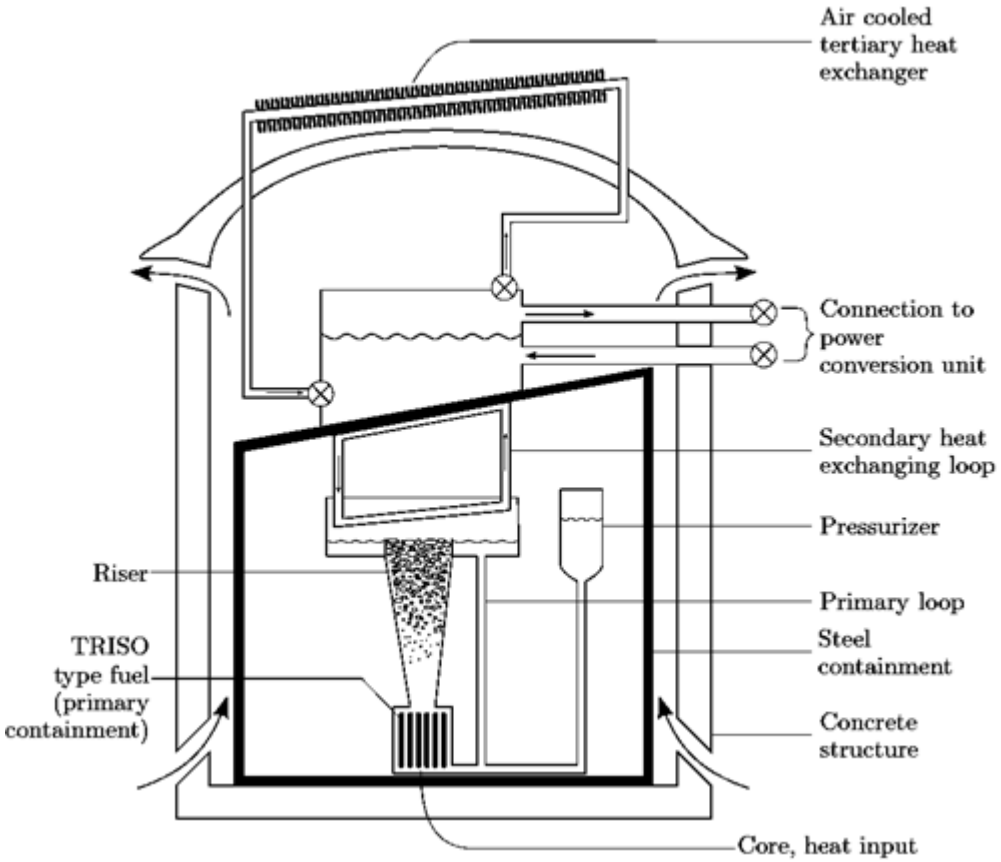


**Figure 2:** Nuclear reactor concept showing major components (Loubser, 2014)

The primary loop has flashing-driven flow. The water is heated within the reactor vessel and rises up into the flash tube. The hydrostatic pressure decreases as the fluid moves upward and once the hydrostatic pressure drops below saturation pressure, rapid steam generation (flashing) occurs (Zhang *et al*., 2012). The steam produced during this flashing process rises into the steam drum and then condenses on the interface with the secondary loop, transferring thermal energy to the fluid within the secondary loop. The secondary loop's function is to transfer heat from the primary loop to the tertiary loop while ensuring that the working fluids within them remain separated. It is a simple thermosyphon using methanol as its working fluid. Its evaporator is in the primary loop's steam drum and its condenser in contact with the tertiary loop's steam drum. The tertiary loop's steam drum is heated by the secondary loop's condenser and produces steam that rises into the natural-convection air-cooled condenser where it is condensed and the heat is transferred to the environment.

Loubser (2014) and Whal (2012) designed and constructed the primary loop and the evaporator of the secondary loop. This project focuses on the building, assembling and testing of the tertiary loop, as well as the development of a numerical simulation model for the tertiary loop. The condenser  However, the project also briefly delves into developing a new simulation to better model the

primary loop so that a holistic idea of how the concept model works becomes apparent.

## 1.2 OBJECTIVES

The problem statement can be postulated by two questions. Firstly, does the tertiary loop system developed successfully cool itself through the air-cooled condensers? Secondly, does the simulation developed successfully reflect the thermal-hydraulic behaviour of the tertiary natural circulation system? To answer these questions, the following objectives have been set.

1. To design, build, commission and test the tertiary loop under safe experimental operating conditions.
2. To develop a theoretical model of the thermal-hydraulic performance of the as-built tertiary loop system.
3. To build a transient, semi-explicit numerical simulation based on the tertiary loop theoretical model developed.
4. To establish the validity of the theoretical simulation by comparing the theoretical results to and with the experimentally determined values.

Secondary objectives are formulated to gain a holistic understanding of the passive nuclear cooling system, comprising the primary, secondary and tertiary loops.

5. To develop a transient, semi-explicit theoretical simulation of the as-built primary loop system and investigate how well the numerical simulation compares with the experimental test results.
6. To develop, an implicit, steady state simulation model of the primary, secondary and tertiary loops to predict how the complete passive cooling system would operate.

## 1.3 THESIS LAYOUT

A brief overview of the thesis is discussed in this section. A literature survey is prepared to review the existing research in the relevant fields. It looks at the need for nuclear energy sources and some of the reactors in use today. Natural circulation loops (NCLs) are investigated. The different types of modelling techniques for NCL flow are discussed. The types of instabilities expected in NCL flow are briefly covered, as well as the means with which to mitigate them. There is discussion of the theory used to model the systems for the primary loop, secondary loop and tertiary loop. A layout of the experimental setup is then given to show how the system was designed and commissioned. The experimental results from the tertiary loop are analysed and compared to the theoretical numerical simulation developed. The primary loop numerical simulation is validated against experimental results and a projection is made of how all three loops would function together.

# 2 LITERATURE SURVEY

This section looks into nuclear energy sources and some of the new generation reactors in use today. Natural circulation loops (NCLs) are investigated. The complexity of two-phase flow through a NCL makes design and modelling very difficult. The different types of modelling techniques for NCLs, and which is best for the purposes of this project, are discussed. Finally, a discussion on instabilities in natural circulation flow and how to mitigate them is covered.

## 2.1 RENEWABLE AND NUCLEAR TECHNOLOGIES

The world requires more sustainable methods of producing electricity, and nuclear power sources are becoming attractive options for doing so. Karakosta *et al.*, (2013) did a comparison of various renewable energy sources (RES) and two advanced nuclear technologies. Their assessment concluded that nuclear technologies compare favourably to the solar, wind, biomass and fuel cell RES that they investigated. Nuclear plants have starting costs similar to other RES, however, the economics improve with time. Once running the average electricity costs is lower than 50% of the RES. Furthermore, the nuclear reactors have an electricity generation capacity approximately 50 times higher than the other RES and the second largest baseline energy output after biomass. In terms of greenhouse gas (GHG) mitigation, the nuclear technologies outperformed the RES, with emissions of 5 $gCO_2$ eq/$kWh_e$ over their full life cycle.

Van der Zwaan (2013) also investigated the role of nuclear power in alleviating emissions from power generation. The GHG emissions for several power production options are shown in Figure 3, based on data from Weisser (2007). A close correlation for the reported GHG emissions exists. The mean GHG emissions from nuclear energy were found to be approximately 10 g $CO_2$ eq/$kWh_e$ with a variance of 5 g $CO_2$ eq/$kWh_e$.

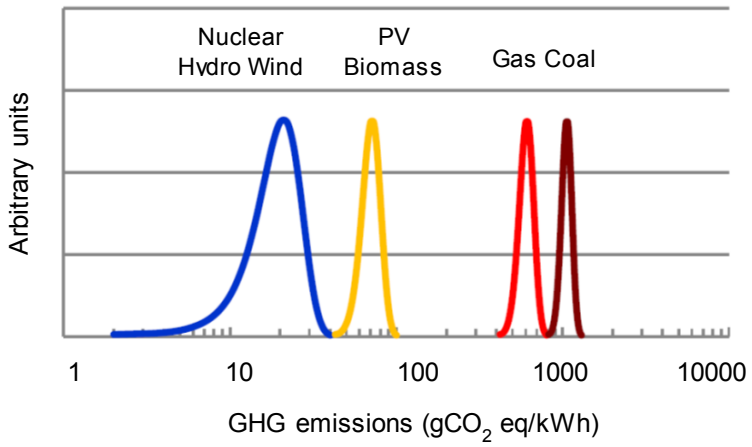


**Figure 3:** Life cycle analysis results for power production methods (adapted from Van der Zwaan, 2013)

Despite the benefits of nuclear power when compared to RES, there are problems associated with it such as nuclear waste disposal, public acceptance and weapons proliferation. The strong adverse reactions to nuclear power sources are mainly due to the accidents, which gained widespread attention: Three Mile Island, Chernobyl and, most recently, the Fukushima Daiichi incident in 2011. Providing better understanding of new generation plants may help change public opinion. The generation III and III+ reactors, which have been in operation since 1996, have perfect safety records.

Strupczewski (2003) argued that the media's depiction of nuclear accident consequences is skewed from the actual safety level of modern nuclear power plants. Despite the reactor-core melt at Three Mile Island, the remaining barrier's (reactor vessel and containment) integrity was intact. There have been no health effects attributed to the incident, since the radiation released was limited. The cancer risk was below $10^{-6}$ per lifetime, less than that of a coal-fired power plant's normal yearly emission at that time.

In contrast, the Chernobyl incident released significant quantities of fission products, resulting in 28 men on the rescue team dying due to radiation exposure. Subsequently, another 10 people died of thyroid cancer by the year 2003. People living in the contaminated areas received low doses of radiation, less than the naturally occurring amount in many parts of the world, as shown in Figure 4.

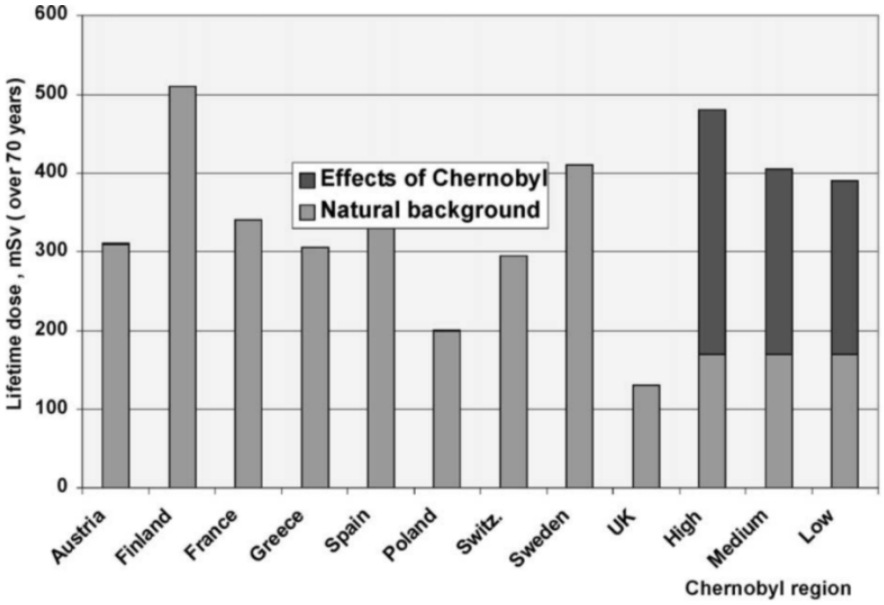


**Figure 4:** Lifetime radiation dose in various regions of Europe (Strupczewski, 2003)

Rogner (2013) studied the outlook for nuclear power in light of the Fukushima accident. He noted that the incident caused a great deal of reflection about nuclear power but did not cause significant retraction of national nuclear

programs around the globe. Some countries with existing nuclear plants decided to phase out the use of nuclear technologies, namely Germany, Switzerland and Belgium. The countries moving forward with their nuclear plans are nevertheless incorporating lessons learnt from the Fukushima Daiichi accident. There were 444 nuclear reactors being used for electricity generation as of May 2016, with a further 63 new reactors under construction (Nuclear Energy Institute, 2016), demonstrating that it is a commercially viable and established source of energy.

## 2.2 NEW GENERATION NUCLEAR REACTORS

Inherently safe nuclear reactors are not a new idea. Taube *et al.* (1986) presented a nuclear reactor with passive decay heat removal. Loss of coolant or pump pressure would result in immediate removal of the fuel so the system would become subcritical. Removal of decay heat and loss of coolant heat generation would be done through conduction, radiation and natural convection. Notable passive systems include:

- AP1000 (Advanced Passive 1000 $MW_e$) and its forerunner, AP600, were the first licenced nuclear reactor designs using passive safety. The AP1000 is a two-loop pressurised light water reactor (PWR). Ensuring that the primary and secondary coolants do not mix reduces the risk of radioactive particle transmittance (Schultz, 2006).
- The Advanced Pressurised Water Reactor (APWR+) is a 1560 $MW_e$, four loop PWR under development in Japan that produces 1500 $MW_e$ (Dobson and Sittmann, *nd*).
- The Economic Simplified Boiling Water Reactor (ESBWR) is a 1535 $MW_e$, Gen III+, modular reactor developed by General Electric Hitachi and can keep the reactor subcritical with decay heat removal for up to 7 days (Barrett and Marquino, 2013).
- KERENA is a 1250 $MW_e$ Boiling Water Reactor (BWR) developed by the French plant supplier AREVA. It has two active safety systems that require manual operation and four passive safety systems that act as backup (IAEA, 2015).

There is today a growing interest in small and medium reactors (SMRs) for modular plants. Small reactors produce less than 300$MW_e$, and medium, less than 700$MW_e$. They have shorter and cheaper construction times, as well as the flexibility of adding electricity capacity as it is required. They also allow maintenance of individual reactors without a significant effect on electricity output. Furthermore, these SMRs are easily slotted in sites of decommissioned coal-fired plants (World Nuclear Association, 2016). Notable SMR systems include:

- The CAREM project: a small 25 $MW_e$ Pressurised Water Reactor (PWR) under construction in Argentina (Mutsumi and Alberto, 2000).
- The IMR (Integrated Modular water Reactor) being developed in Japan to produce 350 $MW_e$ (Koki *et al.*, 2004).

- The Advanced Heavy Water Reactor (AHWR): a 300 $MW_e$ reactor being developed in India.
- The Small Modular Advanced Reactor Technology (SMART) being studied in South Korea for seawater desalination and small scale power generation. It has a thermal power output of 330 $MW_t$ (Seo, 2013).

Most of the passive nuclear reactor cavity cooling systems of these reactors make use of natural circulation loops (NCL) for heat transfer. There are many innovative, inherently safe, SMR concepts being researched and developed at the moment. These fall into the categories of Light water reactors (LWR), Fast neutron reactors (FNR), Molten salt reactors (MSR) and graphite moderated high temperature reactors. LWRs have the lowest technological risk (World Nuclear Association, 2016) thus the reactor concept being developed was chosen to be a LWR.

## 2.3 NATURAL CIRCULATION LOOPS

Natural circulation is an intricate set of thermal-hydraulic phenomena occurring when a fluid under the influence of gravity connects distinct heat sources and heat sinks (IAEA, 2009). For reactor core heat removal, NCLs can be either integrated, separated or make use of heat pipes. Integrated loops have the primary fluid flowing through the core and the heat is transferred by direct contact, i.e. the circulation takes place within a single containment vessel as shown in Figure 5(a). In separated NCLs the primary fluid is separated from the core as seen in Figure 5 (b).

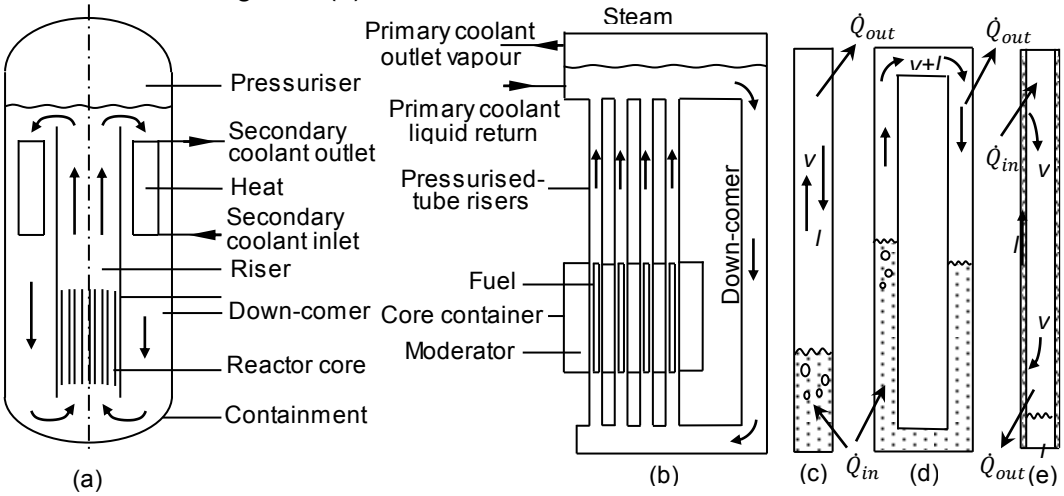


**Figure 5:** Natural circulation loops, (a) integrated, (b) separated, (c) heat pipe, (d) thermosyphon and (e) wicked heat pipe (Dobson, 2016)

Heat pipes, as shown in Figure 5(c) and (e), work as superconductors; they are able to transfer large amounts of heat over long distances without a need for pumping or electricity. Figure 5(c) makes use of gravity driven flow while Figure 5(e) uses capillary action in the wick. Vasiliev (2003) describes them as very

flexible thermal control devices that are easily implemented in heat exchangers. For evaporator and condenser zones they have large heat transfer coefficients of $10^3$ –$10^5$ W/m$^2$K, leading to smaller areas and lighter, more compact structures. They also have low maintenance costs, are reliable and function at low temperatures depending on the working fluid.

A wickless, looped, gravity assisted heat pipe as seen in Figure 5 (d) is known as a thermosyphon. The thermosyphon's lack of a wick reduces the flow resistance for condensate, resulting in higher heat flow (Pioro and Pioiro, 1997). With the condenser above and the evaporator below, two-phase flow systems working under the influence of gravity do not require any pump or capillary action (Franco and Filippeshi, 2011) making them ideal for use in nuclear reactor systems. They are, however, prone to bifurcation and stability problems. Design considerations for the concept being developed attempt to redress these issues.

NCLs have been in use for a long time, but early ones used single-phase fluids. This meant operation was limited by the saturation criterion of the working fluid (Bhattachryya *et al.*, 2012). Through the use of two-phase fluids, a larger pressure gradient can be obtained than for a single-phase fluid in a NCL, which means better circulation and improved overall performance. Two-phase NCLs are simple, passive and have a high heat transfer capacity, resulting in their having many industrial and energy applications; however, the complexity of two-phase flow through a NCL makes design and modelling very difficult.

## 2.4 THEORETICAL SIMULATIONS OF NCLS

There are three methods used to model two-phase NCLs, namely the homogenous, the drift flux and the slip-flow model. The homogenous model assumes that the working fluid is a single compressible fluid that has a cross-sectional averaged density. This model can only be justified for flows having rapid interfacial rates of energy and momentum transfer, that is, well mixed flows (Bhattachryya *et al.*, 2012).

Loubser (2014) when modelling the primary loop used the homogenous model as it is the simplest, however it was only successful while the experiment was in the liquid only regime. Once the phase change started taking place, it was found to give unrealistic results. This is thought to be due to the time dependent, rapid expansion and collapse of vapour bubbles and the poor performance of the homogenous model for flows with large differences in liquid and vapour densities. He found that although the solution converged as the time step was reduced, it diverged as the size of the control volumes was decreased.

The slip-flow or separated flow model is the most successful and has a wide range of applications. It assumes segregated liquid and vapour streams travelling at different velocities but in thermal equilibrium. It incorporates the slip ratio, which is the ratio of vapour to liquid velocity. The introduction of two mass, momentum and energy equations means that there is great complexity. There is

also uncertainty surrounding the interfacial interaction terms, most often, this is a slip ratio correlation involving the pressure and mass quality. If the right terms are used, then this model can generate very realistic results. However, there is no universally acceptable slip ratio correlation available yet, therefore, researchers must depend on empirical relations, which are dependent on specific configurations (Bhattachryya *et al.*, 2012).

The drift-flux model considers the flow of the entire system, rather than separate phases. This eliminates the use of the interfacial terms found in the slip-flow model. A momentum equation is applied to the mixture and a kinematic constitutive equation is used to capture the relative motion. This model should be used when the motion of the phases are greatly coupled (Bhattachryya *et al.*, 2012). It is possible to write out exact conservation equations, but Yadigaroglu and Lahey (1976) show that the level of complexity associated with them requires a large amount of detailed, local and statistical data. This proscribes their use in practical applications requiring simplification of the conservation equations.

To improve on Loubser's theoretical model, a separated flow model simulation is recommended for the primary loop. The tertiary loop will also be modelled using the separated flow model to build a three-dimensional simulation. According to Manera (2003), the separated model is sufficiently complex to take into account the essential phenomena encountered during single- and two-phase flow. The use of the empirical correlations, such as void fraction and the two-phase frictional multiplier, will allow better assessment of the cause-effect relationship in NCL flow.

## 2.5 INSTABILITIES

Modelling is difficult because regenerative feedback is inherent in NCLs, where there is prominent coupling between the flow and its driving force (Nayak and Vijayan, 2008). Instabilities are present in both forced and natural circulation loops but due to the low driving force in the latter, they are more pronounced.

Instabilities are classified in many ways and there is substantial literature on the subject. Vijayan and Nayak (2010) classify them depending on analysis method, propagation method, nature and number of unstable zones, loop geometry and disturbances. Figure 6 shows the types of instabilities experienced in natural circulation loops. Within thermo-hydraulic instabilities there are either static, step change from the original, or dynamic instabilities.

In Figure 6 FDI stands for Fundamental dynamic instability, PDO for Pressure drop oscillations, CDI for Compound dynamic instabilities and DWO for Density Wave Oscillations (Prasad *et al*., 2007).

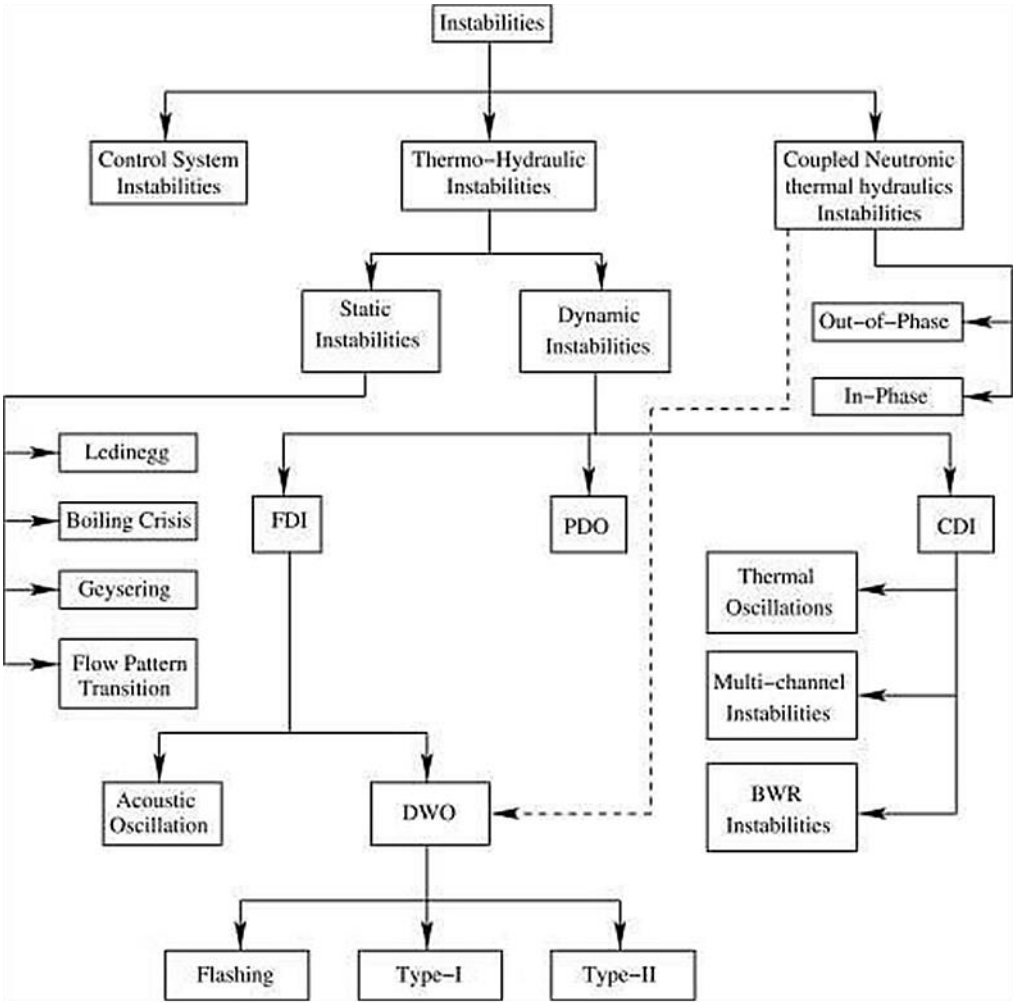


**Figure 6:** Types of flow instabilities (Prasad *et al*., 2007)

Vijayan (2008) shows a stability map based on experimental data. It shows the pressure difference response across a flow meter while varying power supplied to a NCL. Type-I and Type-II flow instabilities can be seen in Figure 7.

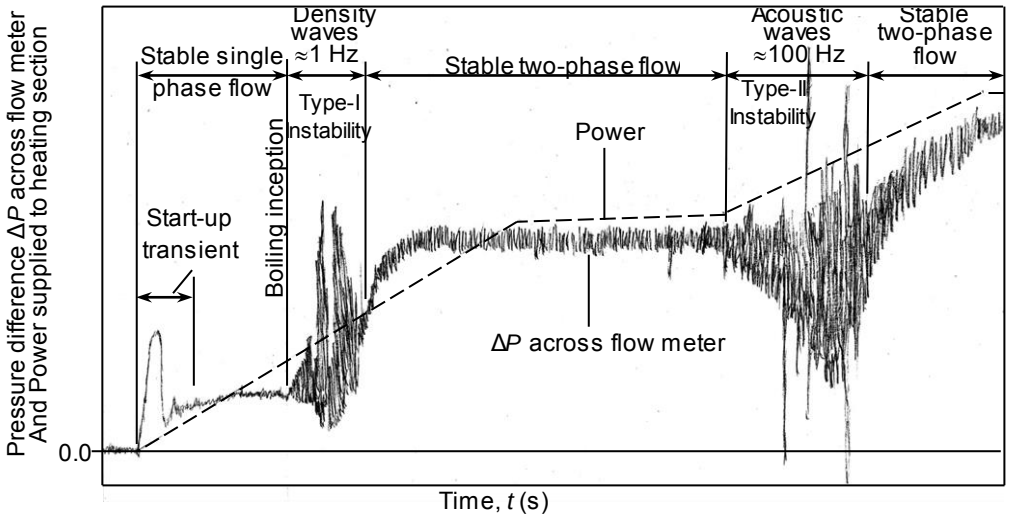


**Figure 7:** Qualitative representation of the pressure difference ΔP across the flow meter and the power supplied to heating section as a function of time (adapted from Vijayan *et al*. 2008)

For any mechanical system, instabilities and oscillations are undesirable, more so in two-phase NCLs where vapour quality is greatly affected by small fluctuations in flow rate. The pressure drop along the flow path is greatly affected by these oscillations, as there is no other device to boost the pressure. As a result, two-phase NCLs often exhibit large oscillations, which can lead to vulnerability, especially for use in nuclear systems (Bhattachryya *et al.*, 2012). The oscillations may also result in vibration and loosening of the components, and possible reduction of the critical heat flux of the system (Nayak *et al.*, 2008).

Stability can be achieved through increasing the system pressure, lowering the heat flux and by sub-cooling the return condensate to a precise range. Sinusoidal oscillations are present with low sub-cooling and intermittent oscillations present with significant sub-cooling (Furuya *et al.*, 2005).

## 2.6 CONCLUSION AND RECOMMENDATIONS

There is clearly a need for more research into passive systems in South Africa for the further development of nuclear power systems for the mitigation of GHG emissions. Despite the difficulties associated with natural circulation loops, they are ideal for use in passive nuclear heat removal systems.

Application of this project may lead to developmental concepts, which may in turn, be used for reactor cavity cooling and steam generation for electricity production. The concept looked at in this project will be for use in a small, 100 $MW_e$, modular LWR. It will make use of three integrated thermosyphon loops for cooling of the reactor cavity and hydrostatic pressure to ensure flash-driven flow. The three thermosyphons that make up the primary, secondary and tertiary loops have different vapour formation characteristics and working fluids so the simulations will differ.

The primary loop will be modelled using a one-dimensional, two-phase, separated-flow model to accurately capture the flashing characteristics. The secondary loop is a simple thermosyphon and will be modelled in terms of its heat transfer capabilities. The tertiary loop will be modelled using a three-dimensional, two-phase, separated-flow model to capture the boiling and condensate formation.

Stability can be improved by increasing the system pressure, lowering the heat flux and by sub-cooling the return condensate to a precise range (Furuya *et al.*, 2005). The stable region in natural circulation systems is larger for higher system pressures (Furuya, Inda and Hagen, 2005). However, operating the system at high pressures creates safety concerns, such as leakage of pressurised steam and bursting of the steam drum. Therefore, increased heat transfer areas are desirable to accommodate a lower heat flux and to facilitate sub-cooling of the return condensate. This must be taken into consideration during the design of the remainder of the secondary loop and the entirety of the tertiary loop.

# 3 THEORETICAL MODELLING

## 3.1 PRIMARY LOOP THEORETICAL MODEL

The theoretical model for the primary loop shown in Figure 8 is developed in this section. It makes use of two-phase, separated flow conservation equations. To refine the solution space some necessary assumptions are made. The conservation equations are then derived and put in their necessary forms for the numerical simulation.

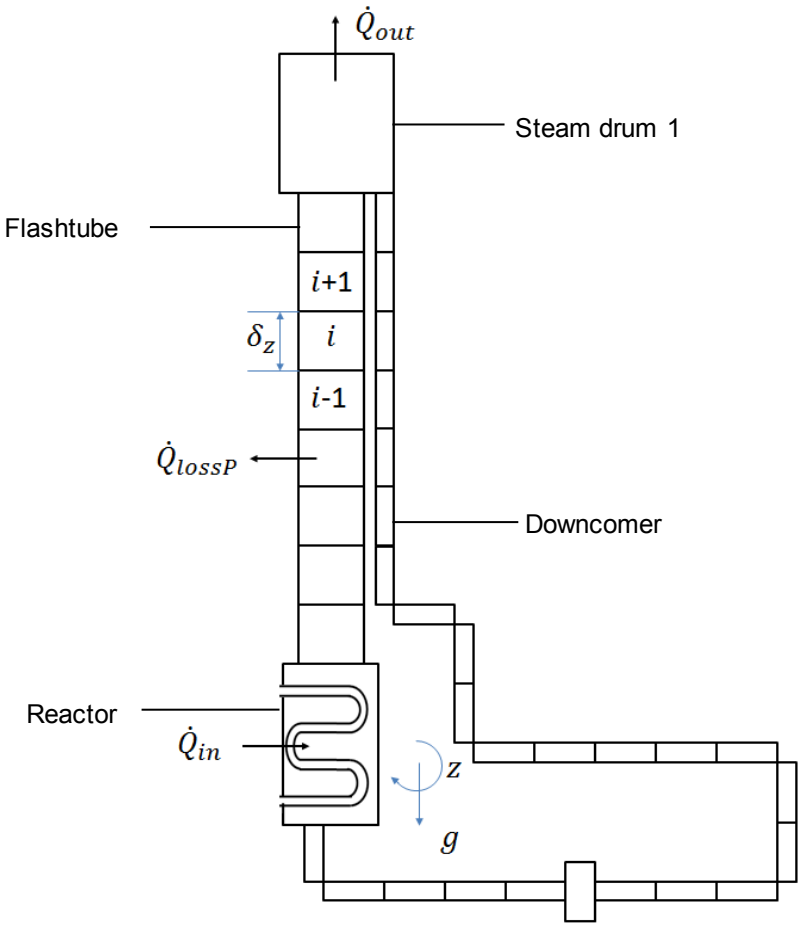


**Figure 8:** Primary loop discretisation scheme

The primary loop is discretised into cylindrical control volumes as shown in Figure 8. The equations developed in this section will be applied to each control volume in turn. As illustrated in Figure 8, the working fluid moves in the z-direction with control volume heights being a length of $\delta z$ and $N_{tot}$ being the number of control volumes in the loop. The reactor and steam drum are modelled as single control volumes with the riser and downcomer being discretised into numerous, smaller control volumes.

### 3.1.1 Assumptions

- The flow path consists of cylindrical one-dimensional control volumes.
- The system is best simulated using a separated flow model.
- The fluid particle velocity is much slower than the speed of sound in the fluid, thus the flow exhibits quasi-steady state behaviour. Thus, at any instant in time the mass flow rate in the loop is independent of its position in the loop.
- At any instant in time, the fluid is essentially incompressible and displaced out of the control volume by the steam formed and into the steam drum instantaneously and at constant pressure.
- As the vapour is formed, the internal energy of the displaced fluid is assumed to find its way instantaneously into the steam drum, without affecting the energy of the control volumes between it and the steam drum.
- The amount of liquid in the steam drum is sufficiently large that the liquid or vapour displaced into it does not affect its internal energy. Neither does it affect the height of the liquid in the steam drum.
- The flow is primarily in the positive z-direction shown in Figure 8.
- The heat transfer due to conduction is negligible.

### 3.1.2 Conservation of mass

Conservation of mass is applied to the control volume shown in Figure 9 consisting of part liquid water and part steam. Figure 9 shows the mass flows across the control volume interface as well as the liquid-gas interface inside it. It has a cross-sectional area of $A_x = \pi\, d^2/4$ and a circumferential shear stress area of $A_z = \pi d\delta z$. For non-circular section's the loop diameter, $d$, can be replaced by the hydraulic diameter, $d_h = 4A_x/A_z$. The control volume's inclination changes around the loop so the conservation equations will be developed for an arbitrary inclination of $\theta$ referenced from the horizontal plane.

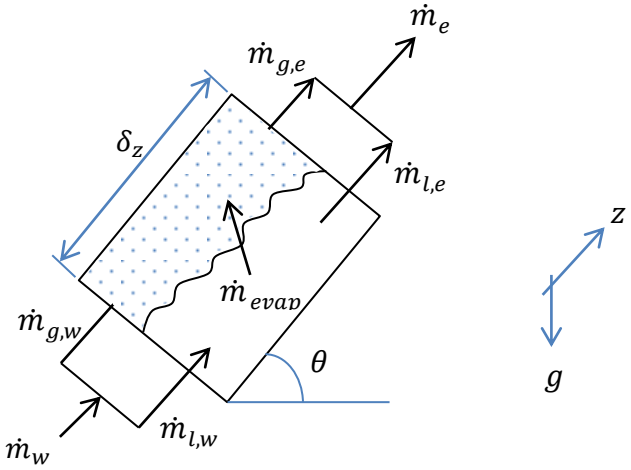


**Figure 9:** Conservation of mass control volume

The conservation of mass equation can be derived from the differential continuity transport equation for compressible Newtonian fluids, given by Equation 3.1.1 adapted from Versteeg and Malalasekera (2007), where $S_m$ represents any other sources of mass per unit volume.

$$\frac{\partial(\rho)}{\partial t} + div(\rho v) = S_m \tag{3.1.1}$$

When applied to the one-dimensional vapour control volume it becomes

$$\frac{\partial(\rho)}{\partial t} + \frac{\partial(\rho v)}{\partial z} = S_m \tag{3.1.2}$$

When applying the equation to two-phase flow, Equation 3.1.2 is applied to each phase individually and then the phases added together. The void fraction, $\alpha$, is needed for the continuity equations and is defined as the gas volume fraction. Since $\delta z$ is the same for both flow components the volume fraction can be redefined in terms of area as Equation 3.1.3.

$$\alpha = \frac{V_g}{V_g + V_l} = \frac{A_{xg}}{A_{xg} + A_{xl}} = \frac{A_{xg}}{A_x} \tag{3.1.3}$$

For the gaseous phase the continuity equation is given in terms as

$$\frac{\partial(\alpha\rho_g)}{\partial t} + \frac{\partial(\alpha\rho_g v_g)}{\partial z} = \dot{m}_{evap} \tag{3.1.4}$$

For the liquid phase conservation of mass is similarly given by

$$\frac{\partial[(1-\alpha)\rho_l]}{\partial t} + \frac{\partial[(1-\alpha)\rho_l v_l]}{\partial z} = -\dot{m}_{evap} \tag{3.1.5}$$

where $\dot{m}_{evap}$ is the rate of liquid evaporation and adds to the existing vapour. When Equation 3.1.4 and Equation 3.1.5 are added together, they become

$$\frac{\partial}{\partial t}\left[\alpha\rho_g + (1-\alpha)\rho_l\right] + \frac{\partial}{\partial z}\left[\alpha\rho_g v_g + (1-\alpha)\rho_l v_l\right] = 0 \tag{3.1.6}$$

Assuming quasi steady state behaviour implies that the time differential can fall away, giving the final differential equation for the conservation of mass in Equation 3.1.7.

$$\frac{\partial}{\partial z}\left[\alpha\rho_g v_g + (1-\alpha)\rho_l v_l\right] = 0 \tag{3.1.7}$$

Integrating Equation 3.1.7 across the spatial domain of a single control volume and simplifying results in Equation 3.1.8.

$$\left\{\left[\alpha\rho_g v_g + (1-\alpha)\rho_l v_l\right]_e - \left[\alpha\rho_g v_g + (1-\alpha)\rho_l v_l\right]_w\right\} A_x = 0 \tag{3.1.8}$$

The void fraction is needed to determine the mass flow rate. A formula for void fraction is now developed in terms of the mass fraction, $x$, and the slip ratio, $v_g/v_l$. The first step is to break down the liquid and gaseous mass flow rates in terms of their velocities and $\alpha$, as given in Equation 3.1.9 and 3.1.10.

$$\dot{m}_g = \rho_g v_g A_g = \rho_g v_g \alpha A \tag{3.1.9}$$

$$\dot{m}_l = \rho_l v_l A_l = \rho_l v_l (1-\alpha) A \tag{3.1.10}$$

The mass fraction of the flow is given by

$$x = \frac{m_g}{m_g + m_l} = \frac{\dot{m}_g}{\dot{m}_g + \dot{m}_l} \tag{3.1.11}$$

Thus, the liquid and gaseous mass flow rates can be expressed in terms of $x$ as

$$\dot{m}_g = x\dot{m} \tag{3.1.12}$$

$$\dot{m}_l = (1-x)\dot{m} \tag{3.1.13}$$

Combining Equation 3.1.9 and 3.1.12 gives

$$x\dot{m} = \rho_g v_g \alpha A \tag{3.1.14}$$

Combining Equation 3.1.10 and 3.1.13 gives

$$(1-x)\dot{m} = \rho_l v_l (1-\alpha) A \tag{3.1.15}$$

Dividing Equation 3.1.15 by 3.1.14 gives the final formulation for void fraction and is given by Equation 3.1.16.

$$\alpha = 1 + \frac{1}{\frac{v_g}{v_l}\left(\frac{1-x}{x}\right)\left(\frac{\rho_g}{\rho_l}\right)} \tag{3.1.16}$$

There are numerous formulas available in literature to determine the slip ratio, but they are limited to flow in small tube diameters. The primary loop's riser has a large diameter and as such, the bubble velocity is high due to the negligible wall shear stress. The bubbles move through a liquid phase that is approximately stagnant and these formulas under-predicted the slip ratio substantially. Duligal (2016) performed experiments on the primary loop and determined that a slip ratio of 21 provided a feasible correlation for the slip experienced during flashing with slug flow.

The conservation of mass formula developed is used in conjunction with the momentum and energy equations. The next chapter deals with the development of the momentum conservation equation.

### 3.1.3 Conservation of momentum

Conservation of momentum principles are applied to the control volume given in Figure 10. It shows the surface and body forces acting on the control volume as well as the momentum flows across the cross-sectional areas.

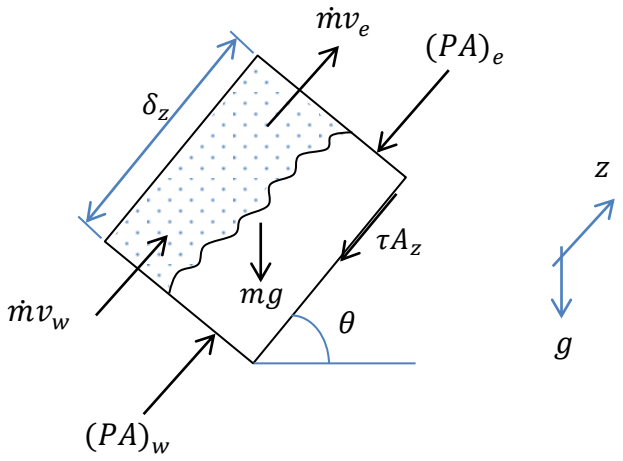


**Figure 10:** Conservation of momentum control volume

The differential form of the momentum conservation equation for compressible Newtonian fluids from Versteeg *et al.* (2007) is given as

$$\frac{\partial(\rho v)}{\partial t} + div(\rho v v) = -\frac{\partial P}{\partial z} + \frac{\partial \tau}{\partial z} + S_M$$

where $S_M$ represents any other sources of momentum per unit volume. The shear term will be rewritten as a momentum source term with an average shear stress for each control volume. Another source term is the body force due to gravity. Thus the general conservation of momentum equation can be reformulated as Equation 3.1.17.

$$\frac{\partial(\rho v)}{\partial t} + div(\rho v v) = -\frac{\partial P}{\partial z} - \frac{\tau \pi d}{A} - \rho_g g \sin\theta \qquad (3.1.17)$$

When applied to the one dimensional vapour control volume it becomes Equation 3.1.18.

$$\frac{\partial(\rho v)}{\partial t} + \frac{\partial(\rho v v)}{\partial z} = -\frac{\partial P}{\partial z} + \frac{\tau \pi d}{A} - \rho_g g \sin\theta \qquad (3.1.18)$$

Integrating Equation 3.1.18 spatially and temporally across the control volume and time step gives the conservation of momentum for the primary loop.

$$\frac{(mv)^{t+\Delta t} - (mv)^t}{\Delta t} + (\dot{m}v)_e - (\dot{m}v)_w = (PA)_w - (PA)_e - \tau \pi d \delta_z - mg \sin\theta \qquad (3.1.19)$$

The change in momentum with time is then expanded to take into account both phases and factor out the mass flow rate.

$$\frac{d(mv)^{t+\Delta t}-(mv)^{t}}{\Delta t}=\frac{\Delta}{\Delta t}\left\{\dot{m}\left[\left(1+\frac{\rho_l}{\rho_g}\frac{1-\alpha}{\alpha}\right)x^2+\left(1+\frac{\rho_g}{\rho_l}\frac{\alpha}{1-\alpha}\right)(1-x)^2\right]\delta z\right\} \quad (3.1.20)$$

Using the term $C$ as defined in Equation 3.1.21, the expression in Equation 3.1.20 can be compacted. It is convenient to simplify the equation in this way because $C$ is equal to $\delta z$ for single-phase fluids.

$$C=\left[\left(1+\frac{\rho_l}{\rho_g}\frac{1-\alpha}{\alpha}\right)x^2+\left(1+\frac{\rho_g}{\rho_l}\frac{\alpha}{1-\alpha}\right)(1-x)^2\right]\delta z \quad (3.1.21)$$

Thus the change in momentum with time can be expressed as

$$\frac{d(mv)^{t+\Delta t}-(mv)^{t}}{\Delta t}=\frac{(\dot{m}\mathrm{C})^{t+\Delta t}-(\dot{m}\mathrm{C})^{t}}{\Delta t} \quad (3.1.22)$$

The flow of momentum into and out of the control volume is similarly expanded to take into account both phases and factor out the mass flow rate.

$$(\dot{m}v)_e-(\dot{m}v)_w=\frac{\dot{m}^2}{A_x}\left[\frac{x^2}{\alpha\rho_g}+\frac{(1-x)^2}{(1-\alpha)\rho_l}\right]_e-\frac{\dot{m}^2}{A_x}\left[\frac{x^2}{\alpha\rho_g}+\frac{(1-x)^2}{(1-\alpha)\rho_l}\right]_w \quad (3.1.23)$$

Using the term $M$ as defined in Equation 3.1.24 for two-phase flow, equation 3.1.23 can be compacted.

$$M=\frac{1}{A_x}\left[\frac{x^2}{\alpha\rho_g}+\frac{(1-x)^2}{(1-\alpha)\rho_l}\right] \quad (3.1.24)$$

For single-phase flow $M=1/(\rho A_x)$. The momentum flow terms can be given as

$$(\dot{m}v)_e-(\dot{m}v)_w=\dot{m}^2\mathrm{M}_e-\dot{m}^2\mathrm{M}_w \quad (3.1.25)$$

Thus Equation 3.1.19, can be expressed in terms of $C$ and $M$ as Equation 3.1.26.

$$\frac{(\dot{m}\mathrm{C})^{t+\Delta t}-(\dot{m}\mathrm{C})^{t}}{\Delta t}=[\dot{m}^2(\mathrm{M}_w-\mathrm{M}_e)+(PA)_w-(PA)_e-\tau\pi d\delta_z-\mathrm{m}g\sin\theta]^t \quad (3.1.26)$$

The shear stress, $\tau$, is given in Equation 3.1.27 in terms of liquid-only shear stress, $\tau_{lo}$, and the two-phase liquid-only frictional multiplier, $\phi_{lo}^2$.

$$\tau=\tau_{lo}\phi_{lo}^2 \quad (3.1.27)$$

Where the liquid-only shear stress is determined from the local Fanning friction factor formula from Cengel and Cimbala (2006) as Equation 3.1.28.

$$\tau_{lo}=C_{flo}\frac{\dot{m}^2}{2\rho_l A_x^2} \quad (3.1.28)$$

The friction factor for the liquid, $C_{flo}$, given in Equation 3.1.29 is dependent on whether the flow is laminar or turbulent. For laminar flow, it is taken as the commonly used $16/Re$. However, at very small liquid velocities, such as those experienced at start up conditions, it results in very small Reynolds numbers, which results in very large friction factors. These enormous friction factors hinder the simulation by over-predicting the shear forces experienced. Thus the laminar flow regime is broken up further into flows with Reynolds numbers less than 1

and those above 1. Blasius coefficient of friction is used for turbulent flow and is taken from Blasius, (1913).

$$\begin{aligned} C_{flo} &= 16 && for\ Re_{lo} < 1 \\ &= \frac{16}{Re_{lo}} && for\ Re_{lo} \leq 1181 \\ &= 0.079 Re_{lo}^{-0.25} && for\ Re_{lo} > 1181 \end{aligned} \tag{3.1.29}$$

where the Reynolds number for liquid only, $Re_{lo}$, is given by Equation 3.1.30.

$$Re_{lo} = \frac{(1-x)\dot{m}d}{\mu_l A_x} \tag{3.1.30}$$

For separated flow the two-phase liquid-only frictional multiplier, $\phi_{lo}^2$, is obtained by making use of empirical correlations. A number of correlations were investigated and it was found that the Wallis correlation in Equation 3.1.31 gave the best results for the primary loop simulation. The Wallis correlation discussed in Wallis (1969) was formed by evaluating the 5th Fanning friction factor using the Blasius equation with $n = 0.25$.

$$\phi_{lo}^2 = \left(1 + x\frac{\rho_l - \rho_g}{\rho_g}\right)\left(1 + x\frac{\mu_l - \mu_g}{\mu_g}\right)^{-1/4} \tag{3.1.31}$$

To account for minor losses in the flow an extra length, $l_m$, is added to $\delta z$ in the shear term. Minor losses are experienced due to bends and changes in cross-sectional areas of the flow path. $l_m$ is based on the flow velocity and the type of features the flow experiences. It is calculated using Equation 3.1.32 from Cengel and Cimbala (2006).

$$l_m = K_L \frac{v^2}{2g} \tag{3.1.32}$$

$K_L$ is the loss coefficient and depends on the flow features. Table 1 shows the loss coefficients that are used in the primary loop simulation.

**Table 1:** Loss coefficients (adapted from Cengel and Cimbala, 2006)

| Flow feature | Image | $K_L$ |
|---|---|---|
| Sharp-edged contraction | 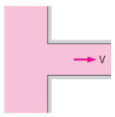 | 0.5 |
| Sharp-edged expansion | 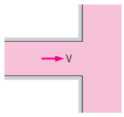 | 2.0 |
| 90° smooth bend | 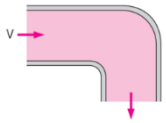 | 0.3 |

From the state of the fluid, $C$ and $M$ can be calculated as they are both functions of density, mass fraction and void fraction. The momentum equation is used to solve the pressure drop across the control volume and mass flow rate. The first aspect to be determined is the pressure drop. Equation 3.1.26 is rearranged to make $P_e$ the subject of the formula in Equation 3.1.33.

$$(PA)_e - (PA)_w = -\frac{(\dot{m}\mathrm{C})^{t+\Delta t} - (\dot{m}\mathrm{C})^t}{\Delta t} + [\dot{m}^2(\mathrm{M}_w - \mathrm{M}_e) - \tau_{\wp}\delta z - \mathrm{m}g\sin\theta]^t$$

$$P_e = \frac{(PA)_w - \left[\frac{(\dot{m}\mathrm{C})^{t+\Delta t} - (\dot{m}\mathrm{C})^t}{\Delta t} - [\dot{m}^2(\mathrm{M}_w - \mathrm{M}_e)]^t + \tau^t_{\wp}(\delta z + l_m) + m^t g\sin\theta\right]}{A_e} \quad (3.1.33)$$

However, the mass flow rate at the new time step, $\dot{m}^{t+\Delta t}$, needs to be determined first. In order to determine the mass flow rate, Equation 3.1.18 is integrated across all the control volumes in the loop. The pressure, when integrated around the loop, will be zero and can be removed from the conservation of momentum equation as shown in Equation 3.1.34.

$$\int_t \sum_{i=1}^{Ntot} \int_w^e \frac{\partial(\rho v)}{\partial t} + \frac{\partial(\rho v v)}{\partial z} A\, dz dt = \int_t \sum_{i=1}^{Ntot} \int_w^e \left(-\frac{\partial P}{\partial z} - \frac{\tau_{\wp}}{A} - \rho g\sin\theta\right) A dz\, dt$$

$$\sum_{i=1}^{Ntot} \frac{(\dot{m}\mathrm{C})^{t+\Delta t} - (\dot{m}\mathrm{C})^t}{\Delta t} = \sum_{i=1}^{Ntot} [\dot{m}^2(\mathrm{M}_w - \mathrm{M}_e) - \tau_{\wp}(\delta z + l_m) - \mathrm{m}g\sin\theta]^t \quad (3.1.34)$$

Rearranging Equation 3.1.34 to make $\dot{m}^{t+\Delta t}$ the subject of the formula gives Equation 3.1.35 to calculate the mass flow rate around the loop.

$$\dot{m}^{t+\Delta t} = \frac{\dot{m}^t \sum_{i=1}^{Ntot} C^t + \left[\dot{m}^2 \sum_{i=1}^{Ntot} (\mathrm{M}_e - \mathrm{M}_w) - \sum_{i=1}^{Ntot} \tau_{\wp}(\delta z + l_m) - \sum_{i=1}^{Ntot} \mathrm{m}g\sin\theta\right]^t}{\sum_{i=1}^{Ntot} C^{t+\Delta t}} \Delta t \quad (3.1.35)$$

The fluid's state is needed at the new time step in order to calculate $C^{t+\Delta t}$. The development of the conservation of energy equation is needed to determine the state of each control volume.

### 3.1.4 Conservation of energy

The conservation of energy principle is then applied to the control volume given in Figure 11. It shows the energy flows across the control volume interface as well as the energy converted to heat due to friction.

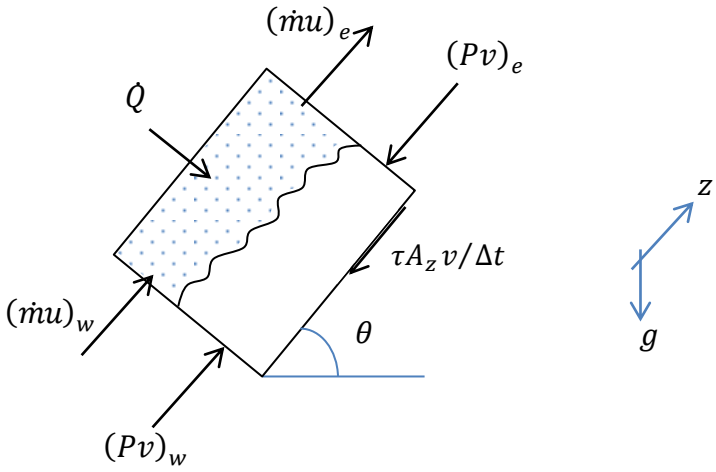


**Figure 11:** Conservation of energy control volume

The conservation of energy for compressible Newtonian fluids is given by the differential governing Equation 3.1.36 from Versteeg *et al.* (2007).

$$\frac{\partial}{\partial t}(\rho u) + div(\rho u v) = div(k\ grad\ T) - P\ div(v) + \tau_z\ div(v) + \dot{Q}''' \qquad (3.1.36)$$

When applied to the one dimensional vapour control volume it becomes Equation 3.1.37.

$$\frac{\partial}{\partial t}(\rho u) + \frac{\partial}{\partial z}(\rho u v) = k\frac{\partial T}{\partial z} - P\frac{\partial v}{\partial z} + \tau_z\frac{\partial v}{\partial z} + \dot{Q}''' \qquad (3.1.37)$$

The conservation of energy principle is applied to the control volume given in Figure 11 and the heat transfer and work done are accounted for. Integrating Equation 3.1.37 with respect to time and over the control volume results in Equation 3.1.38.

$$\frac{(mu)^{t+\Delta t} - (mu)^t}{\Delta t} = \left[(\dot{m}u)_w - (\dot{m}u)_e + k(T_e - T_w) - PA_x(v_e - v_w) + \tau_z A_x(v_e - v_w) + \dot{Q}\right]^t \qquad (3.1.38)$$

Assuming incompressible flow $u = C_p T$ where $C_p$ is the specific heat.

$$k(T_e - T_w) = k\left(\frac{u_e}{C_p} - \frac{u_w}{C_p}\right) = \frac{k}{C_p}(u_e - u_w) \qquad (3.1.39)$$

Work done through expansion/contraction is already accounted for in the 4th term on the right hand side of Equation 3.1.38. To express it in terms of flow rate, pressure and density the following manipulation is done:

$$PA_x(v_e - v_w) = PA_x\left[\left(\frac{\dot{m}}{\rho A_x}\right)_e - \left(\frac{\dot{m}}{\rho A_x}\right)_w\right] = P\dot{m}\left(\frac{1}{\rho_e} - \frac{1}{\rho_w}\right) \tag{3.1.40}$$

Similarly, the work done against friction is expressed as

$$\tau_z A_x(v_e - v_w) = \tau_z A_x\left[\left(\frac{\dot{m}}{\rho A_x}\right)_e - \left(\frac{\dot{m}}{\rho A_x}\right)_w\right] = \tau_z\dot{m}\left(\frac{1}{\rho_e} - \frac{1}{\rho_w}\right) \tag{3.1.41}$$

The conservation of energy equation can then be written as

$$\frac{(mu)^{t+\Delta t} - (mu)^t}{\Delta t} = \left(\dot{m} - \frac{k}{C_p}\right)(u_w - u_e) - P\dot{m}\left(\frac{1}{\rho_e} - \frac{1}{\rho_w}\right) + \tau_z\dot{m}\left(\frac{1}{\rho_e} - \frac{1}{\rho_w}\right) + \dot{Q}_{ht} \tag{3.1.42}$$

However, at the operation conditions of the primary loop $\frac{k}{C_p}$ is found to be negligible compared to the flow rate. Thus, the energy transfer due to conduction can be assumed to be negligible.

$$\frac{(mu)^{t+\Delta t} - (mu)^t}{\Delta t} = \dot{m}(u_e - u_w) + \dot{Q}_{elec} - \dot{Q}_{loss,P} - \dot{Q}_{ps} + \dot{m}(\tau_z - P)\left(\frac{1}{\rho_e} - \frac{1}{\rho_w}\right) \tag{3.1.43}$$

Electrical energy input from the heating elements is represented by $\dot{Q}_{elec}$, which can be varied from 0 to 9 kW. The energy transferred from the primary to secondary loop, $\dot{Q}_{ps}$ is given in Section 3.3, Equation 3.3.1. Energy lost to the environment from the primary loop, $\dot{Q}_{loss,p}$, was determined semi-empirically by Loubser (2014) as Equation 3.1.44.

$$\dot{Q}_{loss,P} = 0.02019\left(\mathrm{T}_p - \mathrm{T}_{env}\right)^2 + 3.111\left(\mathrm{T}_p - \mathrm{T}_{env}\right) \tag{3.1.44}$$

The conservation equations developed for the primary loop are simulated in numerical simulation using the solution algorithm described in Appendix A.

## 3.2 TERTIARY LOOP THEORETICAL MODEL

The theoretical model for the tertiary loop is developed in this section and simulates the fluid flow and heat transfer in the steam inside the air-cooled condensers and the air flowing outside the condenser. Its theoretical model is derived from general fluid flow conservation equations. In order to refine the solution space, some necessary assumptions are made. Subsequently, the conservation equations are derived and put in their necessary forms for the numerical simulation.

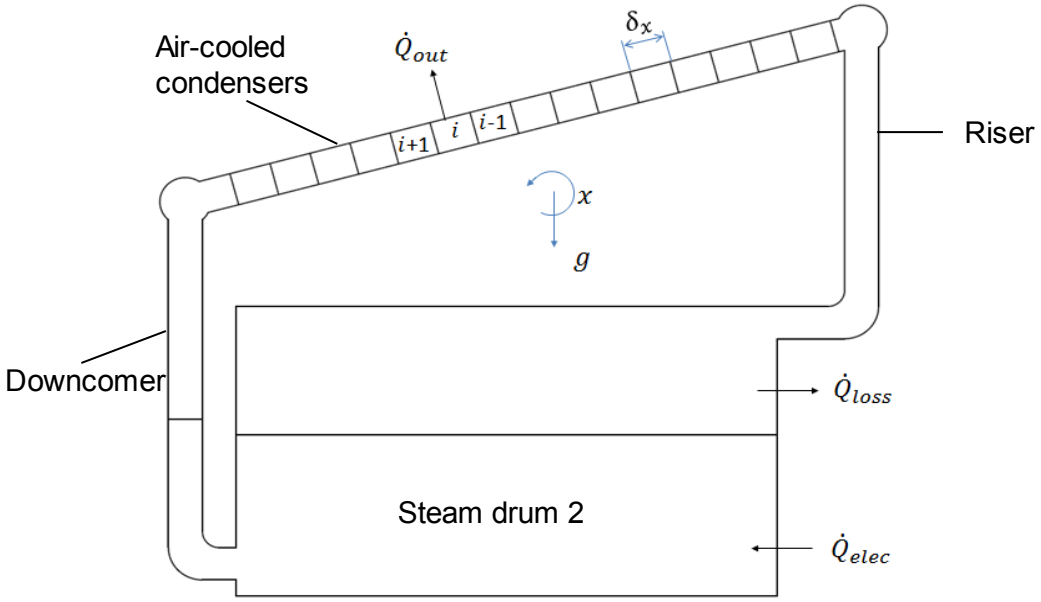


**Figure 12:** Tertiary loop discretisation scheme

### 3.2.1 Assumptions:

- The flow path consists of cylindrical one-dimensional control volumes of vapour and a condensate film flowing along the tube walls in two directions as shown in Figure 14.
- The liquid and vapour are best modelled separately since they flow at different velocities and in different directions.
- The fluid particle velocity is much slower than the speed of sound in the fluid, thus the flow exhibits quasi-steady state behaviour. Thus, at any instant in time the mass flow rate in the loop is independent of its position in the loop.
- Since the system starts at vacuum conditions, the flow entering the condenser is saturated vapour.
- The pressure of the steam and condensate varies in the axial direction only.
- The momentum change of the liquid is negligible compared to the forces due to the pressure drop, friction and gravity.
- Steam drum two is at a vacuum therefore boiling starts as soon as heat is transferred to the system.

- The heat transfer in the air-cooled condenser tubes is only in the radial direction.
- Condensation occurs symmetrically in the condenser tubes.
- The air around the condenser is hydrostatic.
- There is a straight line temperature gradient of the air between the inlet and outlet of the fin space.
- The air flow is modelled as being primarily in the vertical direction even though the condenser is actually at an angle of 15°.
- The flow path of the air consists of rectangular one-dimensional control volumes as shown in Figure 13.
- The velocity of the density wave in the air flow is negligible compared to the acoustic wave velocity. This implies that fluid particle velocity is much slower than the speed of sound in the fluid and the system can be assumed to be in a state of quasi-equilibrium.
- The amount of air in the room is sufficiently large that the heating would not affect the air inlet temperature.

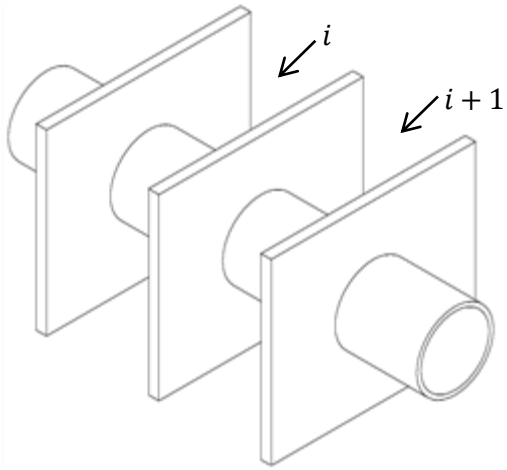


**Figure 13:** Air flow path over condensers

Upon reaching the condenser manifold, the vapour is assumed to split up and flow equally through each of the 16 condenser tubes, where it condenses in a thin film. The liquid condensate forms in an annular layer bound by the inside of the pipe and the inner vapour core. The tertiary simulation models the vapour core in one dimension but the flow of the condensate in two dimensions. As the fluid runs down due to gravity and forward due to the shear force exerted from the flowing vapour, the liquid distribution develops as shown in Figure 14.

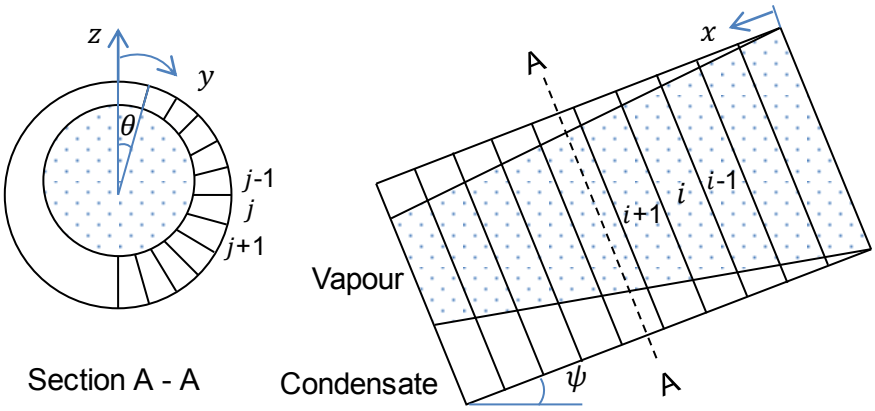


**Figure 14:** Cross-sectional and longitudinal discretised condenser tube

Assuming the liquid film flow is symmetric on either side of the condenser tube, only half of the film will be simulated, as shown in Figure 15. The film forming on the copper tube is discretised and then modelled in two-dimensions with the gravity term changing based on the position of the control volume along the tube wall. The gravity terms in the x-direction and y-direction are given by Equation 3.2.1 and 3.2.2 respectively. The angle of the condenser from the horizontal is given by $\psi$, and the angle that the control volume makes along the wall from the vertical plain is $\theta$.

$$g_x = g \sin \psi \tag{3.2.1}$$

$$g_y = g \cos \psi \sin \theta \tag{3.2.2}$$

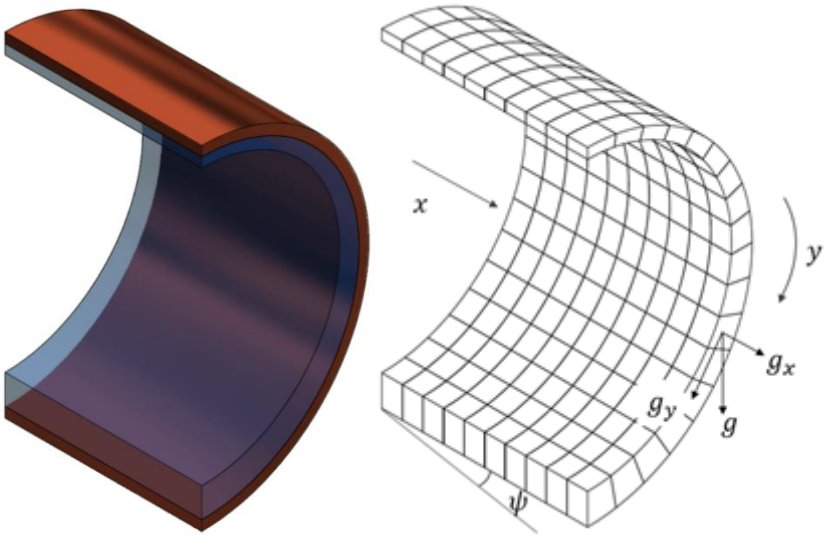


**Figure 15:** Liquid condensate and its discretisation

### 3.2.2 Conservation of mass

Conservation of mass is applied to the vapour control volume shown in Figure 16 consisting of pure steam. Figure 16 shows the mass flows across the control volume interface.

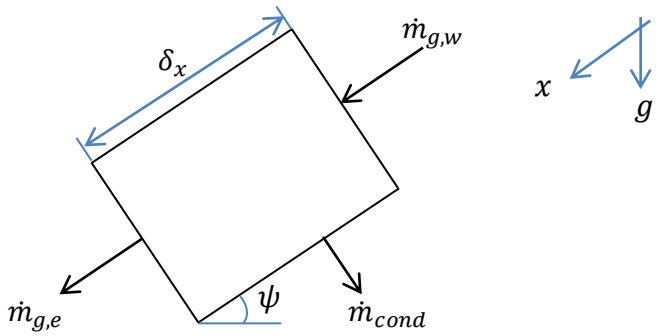


**Figure 16:** Vapour control volume

The flow of the vapour as it leaves the steam drum and through the condensers is modelled. The conservation of mass equation for the vapour flow can be derived from its general continuity form for compressible Newtonian fluids, given by Equation 3.1.4, where the mass source term, $\dot{m}'''_{cond}$, is the rate of condensation per unit volume. Since the simulation is quasi-steady state, the transient term falls away, giving the one-dimensional conservation of mass equation in Equation 3.2.3.

$$\frac{\partial(\rho_g v_g)}{\partial x} = -\dot{m}'''_{cond} \tag{3.2.3}$$

Integrating Equation 3.2.3 across the spatial domain of a single control volume and simplifying gives the final mass conservation for the gas in Equation 3.2.4.

$$\left[(\rho_g v_g)_e - (\rho_g v_g)_w\right] \delta y \, \delta z = -\dot{m}_{cond} \tag{3.2.4}$$

The liquid control volume with mass flows across its boundary is given in Figure 17, where the y-direction is from north to south and x-direction from west to east.

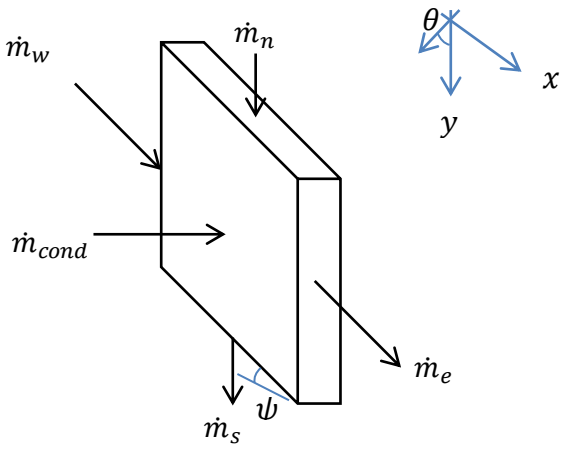


**Figure 17:** Liquid control volume

The film flows along the axis of the condenser tube (x-direction) and circumferentially along the tube wall (y-direction) with condensation taking place radially (z-direction). Therefore, a two dimensional conservation equation is used for the condensation simulation resulting in Equation 3.1.1 being expressed as follows:

$$\frac{\partial(\rho v_x)}{\partial x} + \frac{\partial(\rho v_y)}{\partial y} + \frac{\partial(\rho v_z)}{\partial z} = \dot{m}'''_{cond} \tag{3.2.5}$$

where the condensation is treated as a source term. Integrating Equation 3.2.5 across the spatial domain of a single control volume results in Equation 3.2.6.

$$[(\rho v_x)_e - (\rho v_x)_w]\delta y\,\delta z + \left[(\rho v_y)_s - (\rho v_y)_n\right]\delta x\,\delta z = \dot{m}_{cond} \tag{3.2.6}$$

The conservation of mass principle is now applied to the air control volume given in Figure 18 where the Shear area is given by $A_z = w_{fin}h - \pi d\delta z$ and the average cross-sectional area, $\bar{A}_x$, is found by taking the volume of the control volume divided by the height, $h$: $\bar{A}_x = A_z \frac{\mathrm{s}}{\mathrm{h}}$.

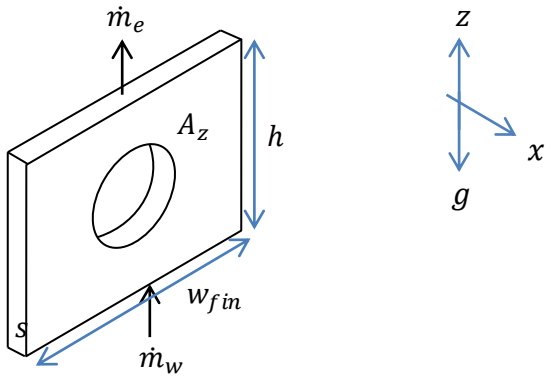


**Figure 18:** Air control volume showing mass transfers

The conservation of mass equation for the air flow can be derived from its general continuity form for compressible Newtonian fluids, given by Equation 3.1.1. Since the simulation is quasi-steady state, the transient term falls away. There is no generation of mass giving the one-dimensional conservation of mass formulated in Equation 3.2.7.

$$[\rho_e v_e - \rho_w v_w] w_{fin} s = 0 \tag{3.2.7}$$

The conservation of mass equations do not give sufficient information about how to determine that actual flow rate. The next Section covers the conservation of momentum principle in order to develop equations for the mass flow rate.

### 3.2.3 Conservation of momentum

The control volume in Figure 19 shows the forces working on the vapour control volume as well as the momentum flows across its cross-sectional area.

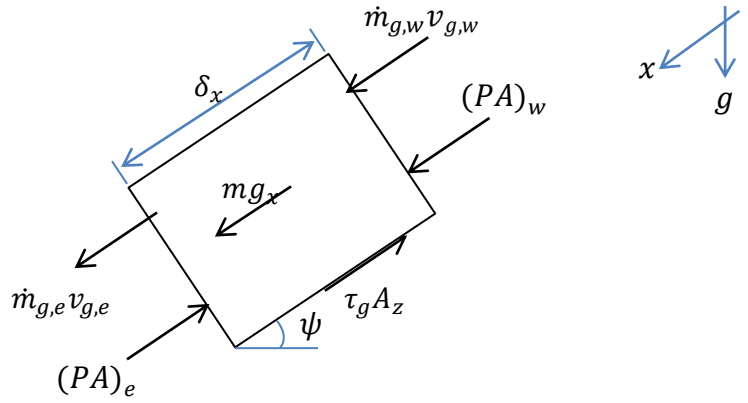


**Figure 19:** Vapour control volume with momentum flows and forces

The general form of the momentum conservation equation for compressible Newtonian fluids is given by Equation 3.1.17. When applied to the one-dimensional vapour control volume it becomes

$$\frac{\partial(\rho_g v_g)}{\partial t} + \frac{\partial(\rho_g v_g v_g)}{\partial x} = -\frac{\partial P}{\partial z} + \frac{\tau_g \wp_g}{A_g} - \rho_g g \sin\theta \tag{3.2.8}$$

The change in density of the vapour with time is negligible and due to the small velocities experienced, the transient term can be removed from the equation.

$$\frac{\partial(\rho_g v_g v_g)}{\partial x} = -\frac{\partial P}{\partial z} + \frac{\tau_g \wp_g}{A_g} - \rho_g g \sin\theta \tag{3.2.9}$$

The vapour mass is sufficiently small that the gravity term can be assumed to be negligible compared to the pressure and shear forces and Equation 3.2.9 can be expressed as

$$\frac{\partial(\rho_g v_g v_g)}{\partial x} = -\frac{\partial P}{\partial z} + \frac{\tau_g \wp_g}{A_g} \tag{3.2.10}$$

Integrating Equation 3.2.10 spatially across the control volume gives the conservation of momentum for the primary loop.

$$\left(\dot{m}_g v_g\right)_e - \left(\dot{m}_g v_g\right)_w = -[(PA)_e - (PA)_w] - \tau_g \wp_g \delta_x \tag{3.2.11}$$

The mass flow rates on the east and west interfaces are derived from the conservation of mass and so Equation 3.2.11 will be expressed in terms of the pressure gradient across the control volume.

$$\frac{dP}{dx} = \left(\frac{\dot{m}_g{}^2}{\rho_g A^2 \delta_x}\right)_w - \left(\frac{\dot{m}_g{}^2}{\rho_g A^2 \delta_x}\right)_e - \frac{\tau_g \wp_g}{A} \tag{3.2.12}$$

This same pressure drop experienced over the gaseous control volumes in the x-direction can be applied in the liquid momentum conservation. The shear stress on the gas, $\tau_g$, is given by

$$\tau_g = C_f \frac{\rho_g v_g{}^2}{2} \tag{3.2.13}$$

where the coefficient of friction is given as

$$\begin{aligned} C_f &= 16 && for\ Re < 1 \\ &= \frac{16}{Re} && for\ Re \leq 1181 \\ &= 0.079 Re^{-0.25} && for\ Re > 1181 \end{aligned} \tag{3.2.14}$$

where the Reynolds number is given as

$$Re = \frac{\rho_g v_g d_g}{\mu_g} \tag{3.2.15}$$

The momentum flows and forces experienced by the liquid control volume are shown in Figure 20. In order to derive the mass flow equations, the differential momentum equations are integrated twice across the film thickness. This is similar to the method used by Groenewald (2001).

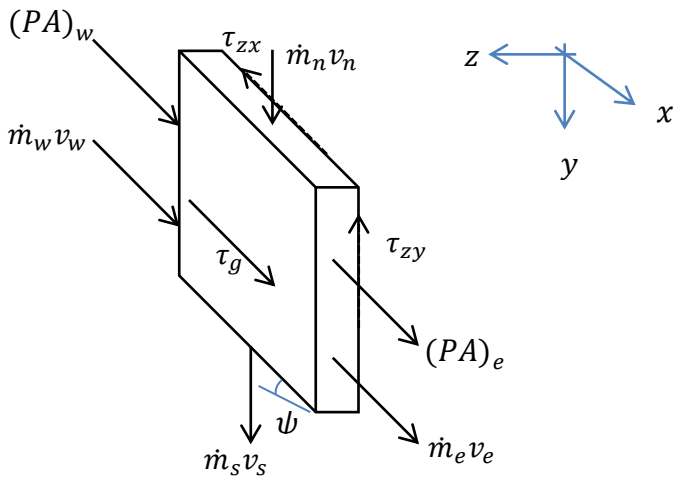


**Figure 20:** Liquid control volume with momentum flows and forces

The conservation of momentum in the x- and y-directions is given in Equations 3.2.16 and 3.2.17 respectively.

$$\frac{\partial(\rho_l v_x)}{\partial t} + \frac{\partial(\rho_l v_x v_x)}{\partial x} = -\frac{\partial P}{\partial x} + \frac{\tau_{xx}}{\partial x} + \frac{\tau_{yx}}{\partial y} + \frac{\tau_{zx}}{\partial z} + \rho_l g_x \tag{3.2.16}$$

$$\frac{\partial(\rho_l v_y)}{\partial t} + \frac{\partial(\rho_l v_y v_y)}{\partial y} = -\frac{\partial P}{\partial y} + \frac{\tau_{xy}}{\partial x} + \frac{\tau_{yy}}{\partial y} + \frac{\tau_{zy}}{\partial z} + \rho_l g_y \tag{3.2.17}$$

There is a negligible change in density and velocity with time; consequently, the transient terms can fall away. The momentum change of the liquid is negligible compared to the forces due to the pressure drop, friction and gravity. Thus, the conservation of momentum differential equations can be expressed as

$$0 = -\frac{\partial P}{\partial x} + \frac{\tau_{zx}}{\partial z} + \rho_l g_x \tag{3.2.18}$$

$$0 = -\frac{\partial P}{\partial y} + \frac{\tau_{zy}}{\partial z} + \rho_l g_y \tag{3.2.19}$$

Assuming that pressure varies in the x-direction only, then $\frac{\partial P}{\partial x} = \frac{dP}{dx}$ and $\frac{\partial P}{\partial y} = 0$. Given that $\tau_{zx} = \mu_l \frac{\partial v_x}{\partial z}$ and $\tau_{zy} = \mu_l \frac{\partial v_y}{\partial z}$ Equation 3.2.18 and 3.2.19 can be expanded to the following forms.

$$0 = -\frac{dP}{dx} + \mu_l \frac{\partial^2 v_x}{\partial z^2} + \rho_l g_x \tag{3.2.20}$$

$$0 = \mu_l \frac{\partial^2 v_y}{\partial z^2} + \rho_l g_y \tag{3.2.21}$$

Integrating Equation 3.2.20 twice with respect to $z$, gives

$$-\frac{dP}{dx} z + \mu_l \frac{\partial v_x}{\partial z} + \rho_l g_x z + C_1 = 0 \tag{3.2.22}$$

$$-\frac{dP}{dx} \frac{z^2}{2} + \mu_l v_x + \rho_l g_x \frac{z^2}{2} + C_1 z + C_2 = 0 \tag{3.2.23}$$

The boundary conditions are evaluated at the tube wall and the liquid-gas boundary. At the tube wall the velocity in the x-direction is zero and the shear force experienced in the fluid is equal to the shear force from the wall on the fluid, $\tau_{w,x}$.

$$\text{at } z = 0;\ v_x = 0, \tau_{zx} = \tau_{w,x}$$

At the film surface, the shear stress in the x-direction is equal to that experienced by the vapour and the shear stress in the y-direction is zero.

$$\text{at } z = \delta_z;\ \tau_{zx} = \tau_g;$$

Using the boundary conditions at $z = \delta_z$ in Equation 3.2.22, $C_1$ is evaluated as

$$C_1 = \left(\frac{dP}{dx} - \rho g_x\right)\delta_z - \tau_g$$

Using the boundary conditions at $z = 0$ in Equation 3.2.23, $C_2$ is evaluated as

$$C_2 = 0$$

Substituting $C_1$and $C_2$ into Equations 3.2.23 an expression can be developed for the velocity in the x-direction

$$v_x = \frac{1}{\mu_l}\left[\left(\frac{z^2}{2} - z\delta_z\right)\left(\frac{dP}{dx} - \rho_l g_x\right) + z\tau_g\right] \tag{3.2.24}$$

Using the boundary conditions at $z = 0$ in Equation 3.2.22 $\tau_{w,x} = -C_1$ thus the shear stress at the wall can be expressed in term of the shear force of the vapour on the liquid.

$$\tau_{w,x} = \tau_g - \left(\frac{dP}{dx} - \rho_l g_x\right)\delta_z \tag{3.2.25}$$

Integrating the y-momentum Equation 3.2.21 twice in the z-direction, through the film thickness, gives

$$\mu_l \frac{\partial v_y}{\partial z} + \rho_l g_y z + C_3 = 0 \tag{3.2.26}$$

$$\mu_l v_y + \rho_l g_y \frac{z^2}{2} + C_3 z + C_4 = 0 \tag{3.2.27}$$

The boundary conditions are evaluated at the tube wall and the film surface. At the tube wall velocity in the y-direction is zero.

$$\text{at } z = 0;\ v_y = 0, \tau_{zy} = \tau_{w,y}$$

At the film surface, the shear stress in the y-direction is zero.

$$\text{at } z = \delta_z;\ \tau_{zy} = 0$$

Applying the boundary conditions at $z = \delta_z$ to Equation 3.2.26, $C_3$ is evaluated as

$$C_3 = -\rho_l g_y \delta_z$$

Applying the boundary conditions at $z = 0$ to Equation 3.2.27, $C_4$ is evaluated as

$$C_4 = 0$$

Having determined $C_3$ and $C_4$ an expression can be developed for the velocity in the y-direction by substituting them into Equation 3.2.27

$$v_y = \frac{\rho_l g_y}{\mu_l}\left[\left(\delta_z z - \frac{z^2}{2}\right)\right] \tag{3.2.28}$$

Using the boundary conditions at $z = 0$ in Equation 3.2.26, $\tau_{w,y} = -C_3$ thus the shear stress at the wall can be expressed in term of the shear force of the vapour on the liquid.

$$\tau_{w,y} = \rho_l g_y \delta_z \tag{3.2.29}$$

The x-component of the mass flow rate is evaluated as:

$$\dot{m}_x = \int_0^{\delta_z} \rho_l \, v_x \delta_y dz$$

$$\dot{m}_x = \frac{\rho_l \delta_y}{\mu_l}\left[-\frac{{\delta_z}^3}{3}\left(\frac{dP}{dx} - \rho_l g_x\right) + \frac{{\delta_z}^2}{2}\tau_g\right] \tag{3.2.30}$$

Similarly, the y-component of the mass flow rate is evaluated as:

$$\dot{m}_y = \int_0^{\delta_z} \rho_l \, v_y \delta_x dz$$

$$\dot{m}_y = \frac{{\rho_l}^2 \delta_x g_y {\delta_z}^3}{3\mu_l} \tag{3.2.31}$$

The conservation of momentum principle is applied to the air control volume given in Figure 21. The general form of the momentum conservation equation for compressible Newtonian fluids is given by Equation 3.1.17. When the air is stationary, the one-dimensional conservation of momentum can be expressed as:

$$0 = -\frac{\partial P}{\partial x} + \frac{\tau_g \wp_g}{A_g} - \rho g \tag{3.2.32}$$

Integrating Equation 3.2.32 across the control volume gives

$$0 = P_e - P_w - \rho h g \frac{\overline{A_x}}{A_x} \tag{3.2.33}$$

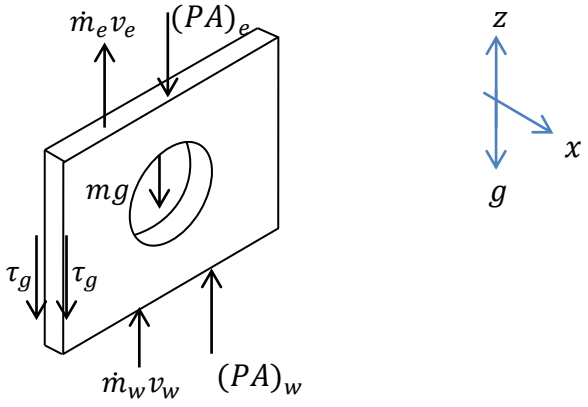


**Figure 21:** Air control volume with momentum flows

Applying Equation 3.1.17 to the control volume shown in Figure 21, when there is heat transfer from the condensers and the air is flowing, gives

$$\frac{\partial(\rho v)}{\partial t} + \frac{\partial(\rho v v)}{\partial x} = -\frac{\partial P}{\partial z} + \frac{\tau \rho}{A_x} - \rho g \tag{3.2.34}$$

Given that the flow is modelled as being quasi-steady state, the first term falls away and the vapour mass is sufficiently small that the gravity term can be assumed to be negligible compared to the pressure and shear forces, therefore, the last term falls away.

$$\frac{\partial(\rho v v)}{\partial x} = -\frac{\partial P}{\partial x} + \frac{2\tau A_z}{A_x} - \rho g \tag{3.2.35}$$

Integrating Equation 3.2.35 spatially across the control volume results in

$$\left(\frac{\dot{m}}{A_x}\right)^2 \left(\frac{1}{\rho_e} - \frac{1}{\rho_w}\right) = P_e - P_w - \rho h g \frac{\overline{A_x}}{A_x} + \frac{2\tau A_z}{A_x} \tag{3.2.36}$$

Under the assumption of hydrostatic flow, Equation 3.2.36 can be substituted into Equation 3.2.33.

$$\left(\frac{\dot{m}}{A_x}\right)^2 \left(\frac{1}{\rho_e} - \frac{1}{\rho_w}\right) = \frac{2\tau A_z}{A_x} \tag{3.2.37}$$

Rearranging Equation 3.2.37 to make the mass flow rate, the subject of the formula gives the final formula for the mass flow rate of the air through the condensers.

$$\dot{m} = \sqrt{2\tau A_z A_x \left(\frac{1}{\rho_e} - \frac{1}{\rho_w}\right)^{-1}} \tag{3.2.38}$$

The next chapter deals with the development of the energy conservation equations for the tertiary loop.

### 3.2.4 Conservation of energy

The conservation of energy principle is now applied to the control volume given in Figure 22.

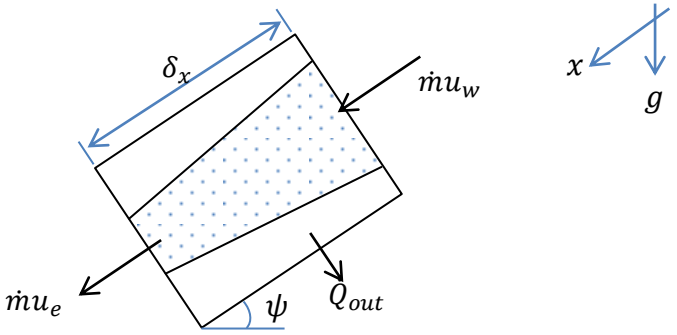


**Figure 22:** Control volume with energy flows

The conservation of energy equation for compressible Newtonian fluids is structured similarly to Equation 3.1.43 in Section 3.1.

$$\frac{(mu)^{t+\Delta t}-(mu)^{t}}{\Delta t}+\dot{m}(u_e-u_w)=\dot{Q}_{elec}-\dot{Q}_{loss,T}-\dot{Q}_{out}+\dot{m}(\tau_z-P)\left(\frac{1}{\rho_e}-\frac{1}{\rho_w}\right) \quad (3.2.39)$$

Heat transfer through the condensers is given by:

$$\dot{Q}_{out}=\frac{T_{sd2}-T_{env}}{R_{out}} \quad (3.2.40)$$

where the thermal resistance for the conduction heat transfer, $R_{out}$, is a combination of the resistances through the film, the copper wall and off surface to the environment.

$$R_{out}=R_{film}+R_w+R_{fin} \quad (3.2.41)$$

$$R_{film}=\frac{k_{film}}{\delta_{film}} \quad (3.2.42)$$

$$R_w=\frac{k_{copper}}{t} \quad (3.2.43)$$

$$R_{fin}=\frac{1}{h_{tco}A_{fin}\eta_{fin}} \quad (3.2.44)$$

The air heat transfer coefficient based on fin spacing, $h_{tco}$, uses the theory of natural convection between finned surfaces from Cengel and Ghajar (2011).

$$h_{tco}=\frac{Nu_L k_{air}}{s} \quad (3.2.45)$$

where the Nusselt number is given by

$$Nu_s=\left[\frac{576}{\left(Ra_s{}^{s}/_{L}\right)^2}+\frac{2.873}{\left(Ra_s{}^{s}/_{L}\right)^{0.5}}\right]^{-0.5} \quad (3.2.46)$$

The Rayleigh, $Ra_s$, number is given in terms of the fin spacing, s, as

$$Ra_s=\frac{g\beta(T_{co}-T_{env})S^3}{v^2{}_{air}}Pr \quad (3.2.47)$$

The fin does not have a uniform temperature over its entire surface but the heat transfer rate is proportional to the temperature difference between the finned surface and the ambient air. Cengel *et al.* (2011) use a fin efficiency, $\eta_{fin}$, to account for the drop in temperature in the radial direction of the fin. The fin efficiency is determined to be 95%. For detailed calculations, refer to Appendix D.4.

The conservation of energy principle is now applied to the air control volume given in Figure 23.

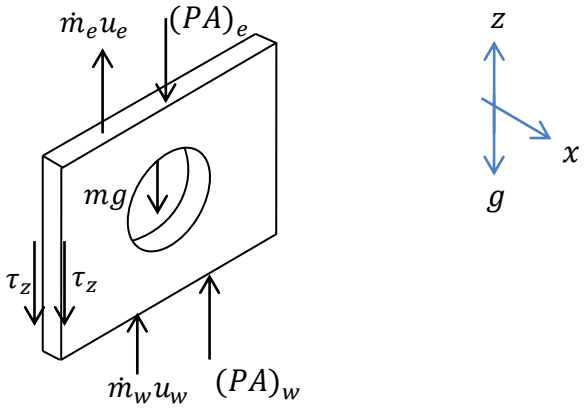


Figure 23: Air control volume for energy conservation

The conservation of energy equation for the air is structured as:

$$\frac{(mu)^{t+\Delta t}-(mu)^{t}}{\Delta t}+\dot{m}(u_e-u_w)=\dot{Q}_{out}+\dot{m}(2\tau_z-P)\left(\frac{1}{\rho_e}-\frac{1}{\rho_w}\right) \tag{3.2.48}$$

The transient term can be removed from Equations 3.2.48, under the assumption of quasi-steady state flow to give

$$u_e=u_w+\frac{\dot{Q}_{out}}{\dot{m}}+(2\tau_z-P)\left(\frac{1}{\rho_e}-\frac{1}{\rho_w}\right) \tag{3.2.49}$$

The conservation equations developed for the tertiary loop are used in a numerical simulation, using the solution algorithm described in Appendix B.

## 3.3 COMPLETE PASSIVE SYSTEM THEORETICAL MODEL

This section develops formulas for the heat transfer coefficients in the evaporator and condenser of the secondary loop. The complete passive cooling system is shown in Figure 24. To refine the solution space, necessary assumptions are made. The heat transfer equations are then determined for the numerical simulation.

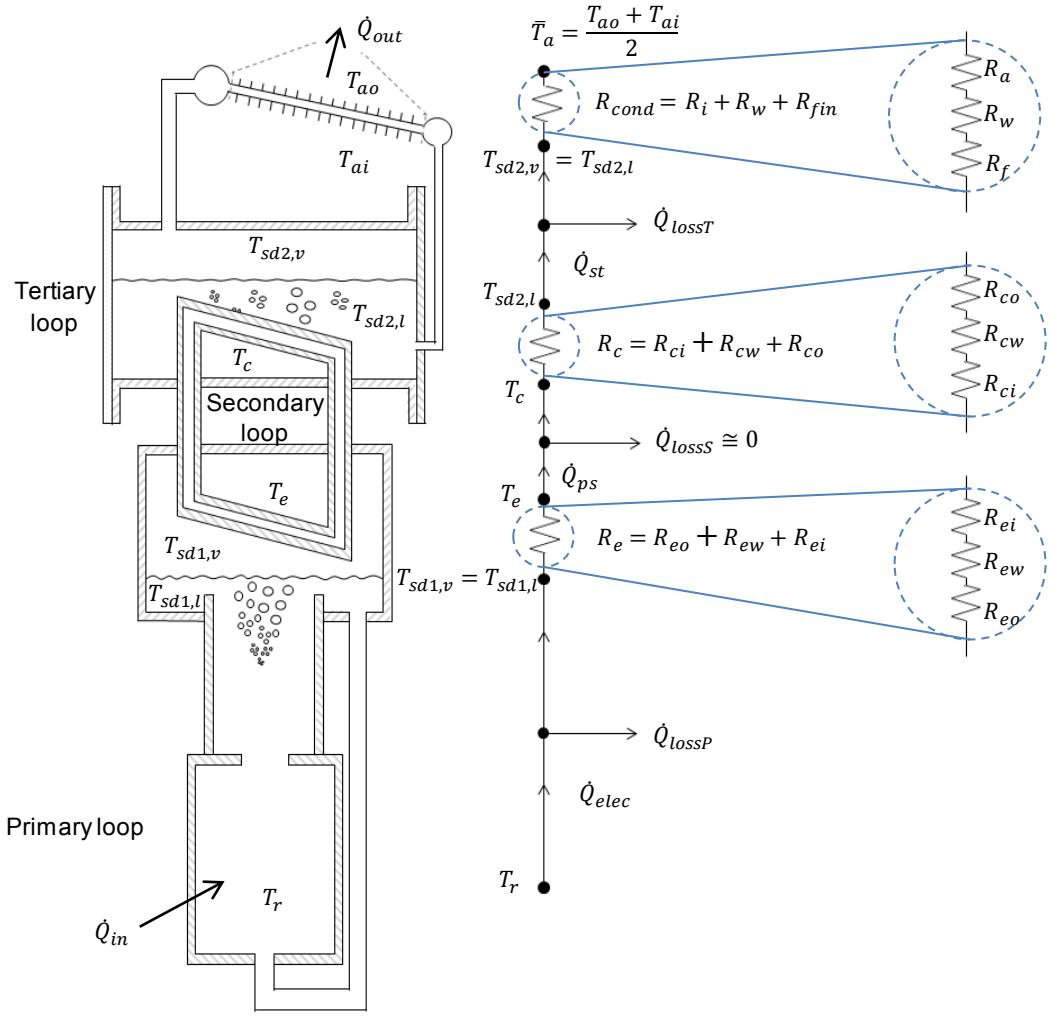


**Figure 24:** Heat transfer model for the complete passive cooling system

### 3.3.1 Assumptions:

- The temperature of the vapour formed in the evaporator is maintained until the vapour reaches the condenser, that is, $T_e = T_c$ and $\dot{Q}_{loss,S} \cong 0$.
- Heat conduction through the walls of the evaporator and condenser is considered to be steady.
- The evaporator section is submerged in vapour at saturation conditions.
- The condenser is submerged in liquid water at saturation conditions.

### 3.3.2 Evaporator heat transfer theory

Energy transfer from the primary to the secondary loop is expressed in terms of a thermal resistance and the temperature gradient from steam drum one to the secondary loop's evaporator.

$$\dot{Q}_{ps} = \left(\mathrm{T}_{sd1,g} - \mathrm{T}_e\right)/R_e \tag{3.3.1}$$

The thermal resistance of the evaporator, $R_e$, from steam drum one to the secondary loop evaporator has three components. The first term in Equation 3.3.2 represents convection heat transfer as the steam condenses on the outside of the evaporator. The second term represents conduction through the evaporator wall. The last term represents convection heat transfer from the inside of the evaporator to the methanol inside the secondary loop.

$$R_e = \frac{1}{\mathrm{h}_{eo} A_z} + \frac{\ln(d_o/d_i)}{2\pi k_c L} + \frac{1}{\mathrm{h}_{ei} A_z} \tag{3.3.2}$$

The heat transfer coefficient on the outside of the evaporator, $\mathrm{h}_{eo}$, is taken from Stephan (1992). This is the mean value over the entire circumference of the tube and is therefore applicable per length of the evaporator tube.

$$\mathrm{h}_{eo} = 0.728\left[\frac{{\rho_l}^2 g h_{fg} {k_l}^3}{\mu(T_{sd1,v} - T_w)} \frac{1}{d}\right]^{1/4} \tag{3.3.3}$$

The heat transfer coefficient on the inside of the evaporator, $h_{ei}$, is expressed in Equation 3.3.4 in terms of the temperature difference between the evaporator wall and the temperature in the evaporator, $(T_{ewi} - T_e)$. It is derived from Cengel and Ghajar (2011) assuming that the boiling would be within the nucleated regime. To ensure this the heat pipe must be charged such that the evaporator would always be immersed in methanol.

$$h_{ei} = \mu_l \, h_{fg}\left[\frac{g(\rho_l - \rho_v)}{\sigma}\right]^{1/2}\left[\frac{C_{pl}}{C_{sf}\, h_{fg}\, {Pr_l}^n}\right]^3 (T_{ewi} - T_e)^2 \tag{3.3.4}$$

where $\sigma$ is the surface tension of the liquid-vapour interface. $C_{sf}$ is an experimental constant that is dependent on the surface-fluid combination, whereby a value of $1.5573\times10^{-3}$ was used for methanol on copper. $n$ is another experimental constant that depends on the liquid chosen and is given by 2.6967. These values were determined from a linear regression model by Loubser (2014) applied to experimental results from the given set up.

### 3.3.3 Condenser heat transfer theory

Energy transferred from the secondary to the tertiary loop, $\dot{Q}_{st}$, is expressed in terms of a thermal resistance and the temperature gradient from the condenser to the liquid in steam drum two in the tertiary loop.

$$\dot{Q}_{st} = \left(\mathrm{T}_c - \mathrm{T}_{sd2,l}\right)/R_c \tag{3.3.5}$$

where the thermal resistance of the condenser, $R_c$, from the secondary loop condenser to steam drum two is given by Equation 3.3.6.

$$R_c = \frac{1}{\mathrm{h}_{ci}A_z} + \frac{\ln(d_o/d_i)}{2\pi k_c L} + \frac{1}{\mathrm{h}_{co}A_z} \tag{3.3.6}$$

The heat transfer coefficient on the inside of the condenser, $\mathrm{h}_{ci}$, is given by Cengel and Ghajar (2011). This is for annular condensation on the inside of vertical or horizontal tubes at low velocities. At low velocities, the condensate becomes stratified and is unevenly distributed.

$$\mathrm{h}_{ci} = 0.555\left[\frac{g\rho_l(\rho_l-\rho_v)k_l^3}{\mu(T_c-T_{cwi})d}\left(h_{fg} + C_{pl}(T_c - T_{cwi})\right)\right]^{1/4} \tag{3.3.7}$$

The heat transfer coefficient on the outside of the condenser is expressed in terms of the temperature difference between the outside of the condenser and the temperature in the steam drum two, $(T_{cwo} - T_{sd2})$. It is derived from Cengel *et al.* (2011) for nucleate boiling.

$$\mathrm{h}_{co} = \mu_l\, h_{fg}\left[\frac{g(\rho_l-\rho_v)}{\sigma}\right]^{1/2}\left[\frac{C_{pl}}{C_{sf}\, h_{fg}\, Pr_l^{\,n}}\right]^3 (T_{cwo} - T_{sd2})^2 \tag{3.3.8}$$

where $\sigma$ is the surface tension of the liquid-vapour interface. A value of 0.013 was used for $C_{sf}$ for water on stainless steel and $n$ is given as 1.0 for water. The next section deals with the experimental set-up used for the validation of the numerical simulation models.

# 4 EXPERIMENTAL SETUP

The experimental setup consists of three loops: the primary, secondary and tertiary loops. This section covers the layout of these loops as well as the design and construction of the secondary condenser and the tertiary loop.

## 4.1 PRIMARY LOOP

The primary loop of the system was designed and built by Loubser (2014) and Whal (2012). It consists of the components shown in Figure 25, namely the reactor, riser or flash tube, steam drum one and the downcomer. Water was used as the working fluid in the primary loop as it is a widely used coolant and neutron moderator making this concept fall into the category of light-water reactors (LWR). Furthermore, water is cheap and relatively easily accessible in South Africa compared to other moderators.

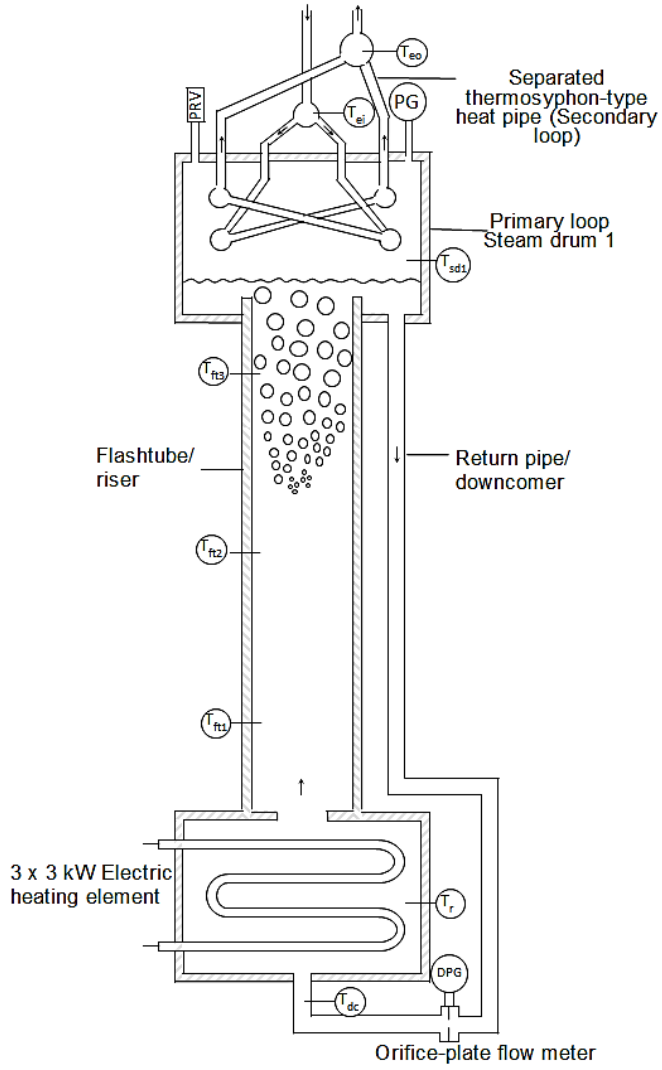


**Figure 25:** Primary loop system showing instrumentation placement

The reactor vessel is a 0.288 by 0.288 by 0.512 m high steel container that is powered by 6 resistance heating elements each rated at 1.5 kW. The elements have a surface heat flux of 3.2 W/cm$^2$. Water enters through the bottom of the reactor vessel and is driven upward when heated. Two sides of the box are made of sight glass as shown in Figure 26. This allows for easy observations of fluid behaviour around the heating elements, as well as characterisation of the flow patterns within the reactor vessel. The window is made of Naxel, a type of polycarbonate chosen for its strength and ability to resist degradation at high operating temperatures. A 4 mm thick, silicone rubber gasket is placed between the Naxel window and the steel to seal the surface. A thick gasket is used due to its ability to seal better against an uneven surface.

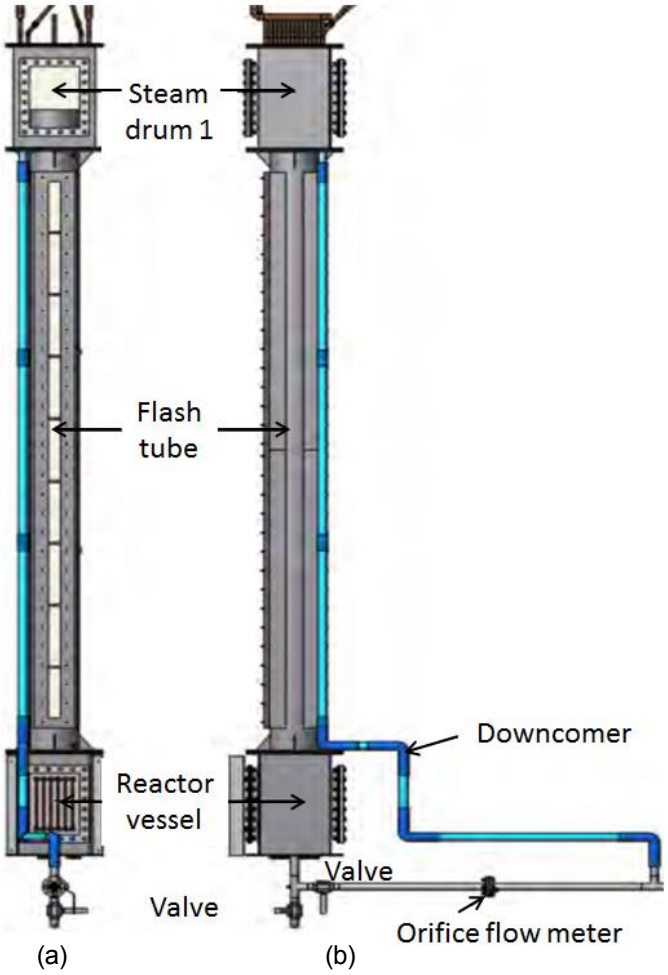


**Figure 26:** Primary system a) front view b) side view

The flash tube or riser extends above the reactor and consists of a 3.2 m long stainless steel pipe. It has an inside diameter of 200 mm with two 50 mm slots opposite each other along its length as shown in Figure 26. This is important as it allows observation and characterisation of the two-phase flow pattern within the riser. The riser was designed sufficiently long to avoid boiling in the reactor

(17 m) but, due to the height restrictions within the laboratory, it was scaled to 3.2 m high. The laboratory is 8 m high and for the whole experiment to fit the primary loop was limited to a height of less than 5m above the ground. Ideally, the riser diameter should increase with height as shown in Figure 2, resulting in a conical shape. However, the riser was simplified into a cylinder due to the difficulty and cost of manufacture.

The riser extends 200 mm into the steam drum above it. This ensures that the liquid condensed in the steam drum does not re-enter the riser but leaves through the downcomer and reduces the minor losses for fluid entering the steam drum 1. The steam drum has a condenser situated at the top of it, consisting of copper tube bundles. The bundles are sloped in such a way that condensate will run under the influence of gravity and drip away from the riser, ensuring most of it flows down the downcomer. The inclination of the tubes allows for more even heat transfer when compared to horizontal tubes. This is because a fluid film develops, allowing steady heat transfer compared to the accumulation and depletion of condensate associated with horizontal tube banks.

A downcomer connects to the bottom of the steam drum and provides the path for returning condensate to the reactor. It is made of a series of glass pipes conjoined with silicone fittings. Silicon was used because of its resistance to buckling under a vacuum. The last section is made of stainless steel to allow the placement of an orifice flow meter and three valves.

One ball valve is placed along the expansion line to isolate the system from the pressuriser. Initially, this valve is opened to fill the primary loop with water. The orifice flow meter is situated on the last length of the downcomer before the reactor. It measures the volumetric flow rate of the water through the primary loop. A second ball valve is placed between the flow meter and the reactor. Its purpose is to permit measurements of the void fraction within the riser section. The third ball valve is placed underneath the reactor at the lowest point of the primary loop. It serves as a water drain for the primary system. The pressuriser consists of an expansion tank at the end of a 21 m long hose. The hose is a heater hose chosen for its ability to work under high temperatures.

A frame is used to house the primary system. It is 5 m tall with a square section of sides 0.6 m. It holds the primary system 0.5 m above the ground and supports the air-cooled condensers of the tertiary system at its top. The frame is placed within a drip tray that is capable of holding all the liquid in the primary and secondary systems. This was added as a safety feature to avoid damage to any structures or components in the room and possible scalding to any persons in close proximity to the system, in the event of a severe leak.

At the highest point of the entire primary loop, a Schrader valve is placed which will be used to remove non-condensable gases from the primary system. There is also a pressure release valve (PRV) that will open should the pressure reach 2 bar absolute.

## 4.2 SECONDARY LOOP

The secondary loop is a gravity driven two-phase thermosyphon that transfers heat from the primary loop steam drum to the tertiary loop steam drum. It consists of an evaporator section, a condenser section and connecting flexible metal hose. This section discusses the existing evaporator and the design of the condenser. The design of the condenser involves specifying requirements, choosing the type of heat exchanger to use and calculating the heat transfer area.

The secondary loop is charged with 320 ml of methanol as suggested by Loubser (2014). Methanol was used as the working fluid for the secondary loop as it is cheap, easily attainable and is more volatile than water. The lower boiling temperature will allow heat transfer from the primary loop, even at saturated conditions, as the temperature gradient will always be favourable.

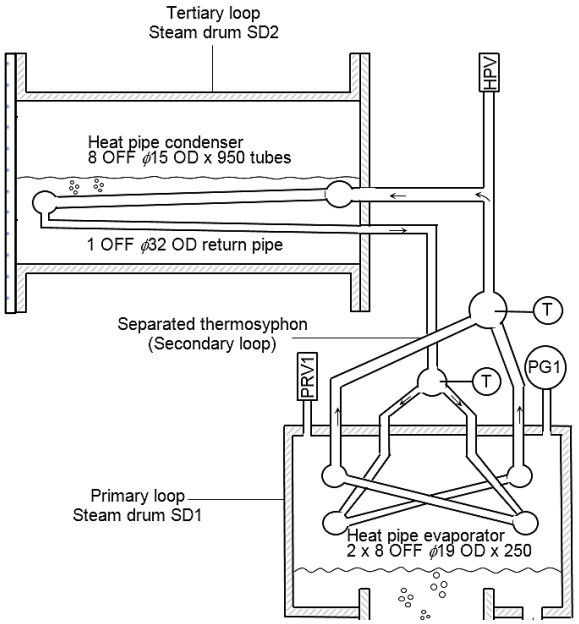


**Figure 27:** Secondary loop layout

### 4.2.1 Evaporator

The evaporator section of the secondary loop was designed by Loubser (2014). This consists of two sets of copper bundles chosen for their high conductivity. Each bundle has sixteen 0.25 m long pipes of diameter 19 mm. The sizing allows the transfer of 9 kW from the primary loop with methanol vapour flowing in the tubes and submerged in liquid water. This ensures that, no matter what phase the evaporator is exposed to, it is sufficiently large to remove the 9 kW input to the primary loop by the electrical elements (Loubser, 2014).

The tubes are interlocked to allow tight packing as shown in Figure 28. This ensures that a large enough heat transfer area is available while making the heat

exchanger small enough to fit in the primary loop steam drum. The tubes sit at an angle of 8° to the horizontal, which encourages the newly formed vapour to always go up through one side and the condensate to return through the other. This reduces the likelihood of entrainment (flooding). Entrainment occurs when the rising vapour and return condensate are flowing opposite to each other in the same pipe and the shear from the vapour stops the flow of the condensate back into the evaporator. This can lead to drying out of the evaporator and temperature spikes, which compromises the heat transfer ability of the heat pipe. Figure 28 shows the evaporator with connections made to join it to the flexible hose CF connections that form the riser and downcomer.

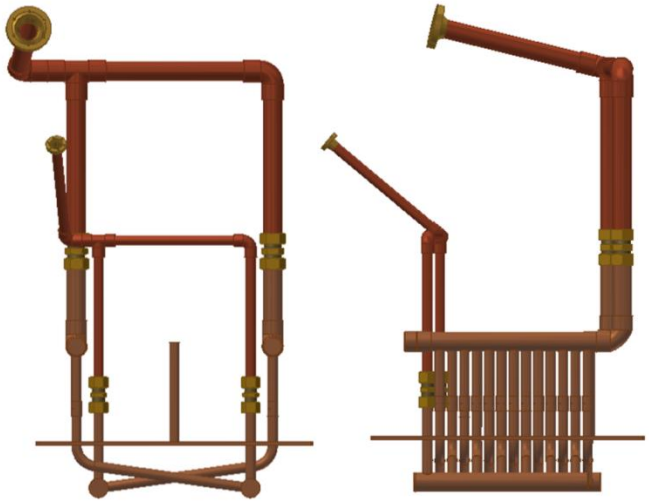

(a) (b)

**Figure 28:** Secondary loop Evaporator a) front view b) side view

### 4.2.2 Condenser design requirements

The design requirements are that the heat exchanger must:

- be able to transmit 9 kW of thermal energy.
- have no reliance on electricity or mechanical components for fluid flow.
- be made of materials capable of handling temperatures of 120 °C.
- be resistant to rust as it will be submerged in water.
- be inclined 3° from the horizontal as suggested by Loubser (2014).
- not put stress on the components of the evaporator.
- seal for both pressure and vacuum conditions.
- be inherently safe.

### 4.2.3 System boundaries

The secondary loop has three boundaries that need to be considered; the first is in the evaporator, which is in the primary loop's steam drum, the second is the section of the secondary loop exposed to the air and the third is the condenser that is inside of the tertiary loop steam drum. For the system to operate efficiently, it must lose minimal heat to the atmosphere. For this reason, all the piping connecting the evaporator to the condenser was covered in insulation.

### 4.2.4 Condenser design

The first step in the design process was choosing the type of heat exchanger. A shell and tube heat exchanger was chosen. It has methanol vapour condensing on the inside and the outside completely submerged in water in a state of nucleate pool boiling. The next step is to size the heat exchanger. The heat transfer area required to transfer 9 kW of thermal energy is 417 989 $mm^2$. Refer to Appendix D.1 for detailed calculations.

The manufactured condenser as shown in Figure 29 has a manifold, which divides into eight 0.95 m long, 15 mm diameter pipes. A manifold joins them back together so that there is only one exit through which the condensate leaves the condenser. Any remaining steam can condense in this 1 m long, 32 mm diameter pipe. The condenser then has an overall heat transfer area of 460 516 $mm^2$, which is 10% higher than required. Thus the design satisfies the design requirement of transferring 9 kW of thermal energy and will facilitate sub-cooling of the condensate. This will result in more stable flow within the secondary loop.

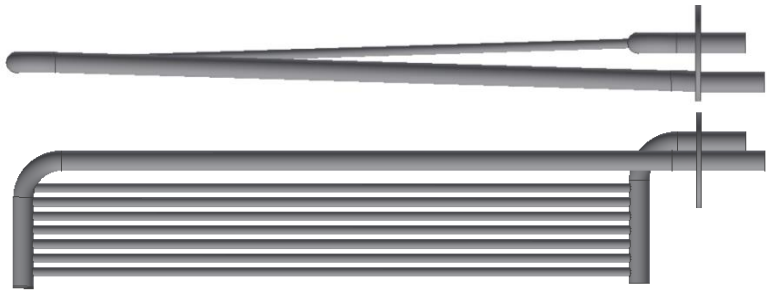

**Figure 29:** Secondary loop condenser a) side view b) bottom view

To avoid transferring thermal stresses to the evaporator, flexible hose was used to connect the fixed components to it. In the event that the condenser experiences thermal expansion, it will not affect the evaporator section, which is bolted to the primary loop. The flexible hose further allowed easy assembly and manoeuvrability of the individual parts. Due to the limited space available above the primary loop, the secondary and tertiary loops could not be stacked easily one on top of the other. The flexible connections allow them to be placed almost side by side.

To ensure that the system is sealed under high-pressure and vacuum conditions, welding of components was done as far as possible, limiting the use of other connection types. The flexible vacuum hose and fittings used are able to take 2 bar positive pressure and $1\times10^{-10}$ bar vacuum (Varian Inc., 2013). The coupling between CF flanges uses a copper gasket that is cut into by the knife-edges inside the flanges to create an airtight seal.

## 4.3 TERTIARY LOOP

In this section, the design of the tertiary loop is covered. This starts with determining the design requirements, system boundaries and choice of heat exchanger type. The steam drum is designed as a pressure vessel. The design of the air-cooled condenser involves choosing the size, which includes the fin spacing, diameter and length.

### 4.3.1 Design requirements

The design requirements of the tertiary loop are that it must:

- have minimal losses.
- be able to transmit 9 kW of thermal energy.
- have no reliance on electricity or mechanical components for fluid flow.
- be vacuum tight.
- be able to handle temperatures of 120 °C.
- minimise start up time.
- ensure inherent safety.
- minimise bifurcation of the circulation.

### 4.3.2 System boundaries

The tertiary system has a boundary with the secondary loop condenser through which heat is transferred. The working fluid within this loop is water, chosen because it needs to generate steam. The steam during normal operation is sent to the power conversion unit to expand over a turbine to generate electricity. To ensure that the temperature gradient is favourable for heat transfer, it is essential that the system can hold a vacuum to ensure that boiling can take place at any temperature.

The experimental set up is inside a closed two-story room with an average temperature of 15 °C and average air pressure of 101.2 kPa. The air temperature affects the amount of heat transferred from the air-cooled condenser, as the incoming air is unconditioned and may vary. This is not ideal but it is indicative of the system's reliability. A further problem arises as the longer the system runs, the warmer the air in the room becomes. This may skew results when compared to how the system may work in well-ventilated conditions.

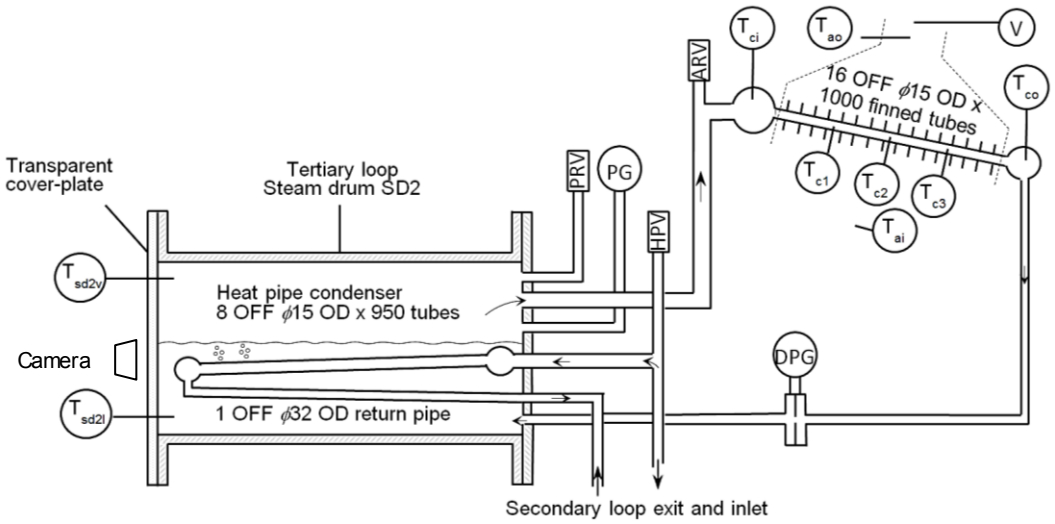


**Figure 30:** Tertiary loop system line drawing

### 4.3.3 Steam drum design

The steam drum for the tertiary system consists of a cylindrical vessel made from 4mm thick stainless steel 304, with an internal diameter of 400 mm, a 5 mm thick stainless steel cover plate and a 12 mm polycarbonate flange. For detailed calculation refer to Appendix D.2. Polycarbonate was used because of its ability to withstand high flexure and high temperatures, while allowing observations to be made within the steam drum. The rest of the steam drum was made of stainless steel to mitigate any corrosion. It houses the condenser from the secondary loop, which is the heat source for the tertiary loop. To allow testing of the tertiary loop independently of the rest of the system, two 3 kW resistance heating elements were placed in the steam drum as well.

The steam drum was made cyclindrical as is customary with pressure vessels, to ensure that the stress is evenly distributed. The diameter of the steam drum was chosen to ensure enough space for the heating elements and secondary loop condensor. This, however, has the disadvantage of requiring a large amount of water to be present in the steam drum. This will negatively influence the requirement for a short start up time.

The system will experience both vacuum conditions and positive pressure. The steam drum was designed as a pressure vessel to ensure that the system will not be vulnerable when pressurised. The front and back flanges are bolted to the steam drum. The front cover plate contains all the ports leading into and out of the boiler.This minimises the chances of leaking as all connections were welded to the flange. It also simplified the manufacturing of the components. These ports included the inlet and outlet of the methanol condenser and the paths through which the steam would leave the steam drum and its return. A pressure gauge (PG2) and a Bailey Birkett, Type 707 pressure release valve (PRV) are also fitted

to the front cover plate. The safety valve is set to open at 1 bar (200kPa) gauge. A ball valve (ARV) is placed at the top most point of the tertiary loop and is the point from which the vacuum will be drawn by a venturi vacuum pump.

An Agilent 34970A Data acquisition unit was used to record the measurements during experiments. Benchlink data Pro was installed on the computer where the measurements were recorded. The thermocouples were connected directly to the data acquisition unit, but the pressure transducers' signal needs to be amplified first using clip amplifiers.

### 4.3.4 Riser and downcomer

The riser connects the steam drum to the condensers. Due to of the limited space the steam drum and condensers were placed on different surfaces so flexible hosing was used to connect them together. This allowed for ease of assembly and flexibility in the layout of the sysytem. This also reduced the mass placed on the top of the frame discussed in Section 3.1. By placing the heaviest component, that is, the steam drum on the catwalk next to the frame, the chances of the frame buckling has been minimised.

The downcomer forms the path for condensate return and connects to the lowest point of the steam drum. This is done to fulfil the design requirement of minimising bifurcation. Steam from the steam space will only leave via the riser and not oppose the flow of condensate return, which could lead to flooding. An orifice plate meter as shown in Figure 31 is placed on the downcommer to determine the volumetric flow rate in the loop. It does this by measuring the pressure difference over the orifice with an HBM 5 kHz inductive differential pressure transducer (DPG). It was designed according to ASME standards (ASME, 2003) for small bore orifice meters with a ratio of orifice diameter over pipe diameter equal to 0.3.

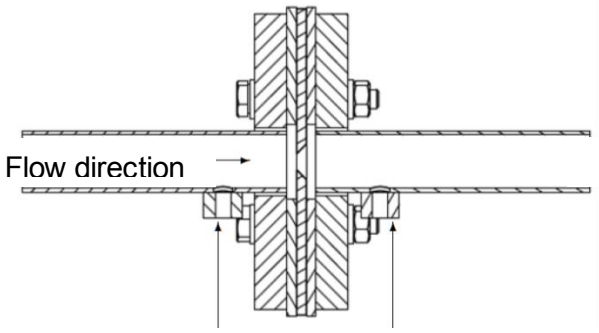


**Figure 31:** Orifice flow meter

Two tapping holes were placed on both sides of the flow meter facing downwards to ensure no bubbles get trapped in the pressure trapping lines. The calibration of the orifice flow meter is presented in Appendix F.

### 4.3.5 Condenser design

The first step in the design process was choosing the type of heat exchanger to be used. A cross-flow steam-to-air heat exchanger was chosen to use a natural draft system to adhere to the inherently safe requirement.

Air-cooled condensers transfer thermal energy from the working fluid to the environment. There are two condensers each of which has eight 1 m long tubes running their length.They consist of an inlet manifold, condenser tubes, condenser fins and the outlet manifold. The tubes are made of copper because of its high thermal conductivity, which increses the heat transfer capability. The brass fins as shown in Figure 32 are press fitted onto the tubes with 4 fins per inch of tube. The fins are are 35 mm high and 320 mm wide and encase the eight tubes along their width. For detailed calculation refer to Appendix D.3 and D.4.

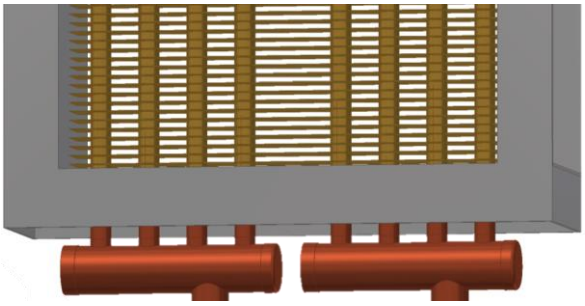

**Figure 32:** Fins on the air-cooled condensers

The tertiary loop system is shown in Figure 33 as it was built. A clear shroud was placed over the condensers to allow the measurement of the temperatures into and out of it, as well as the mass flow rate of the air going through the condensers. The stand was desiged to attch the the top of the existing frame supporting the primary loop. It was designed to allow the air-cooled condensers to be placed at the ideal angle of 15° from the horizontal. This encouraged flow of condensate back to the steam drum and not to gather in the condensers. A drip tray was placed under steam drum two to avoid damage to property and possible scalding to any people underneath the system, in the event of a burst or leak.

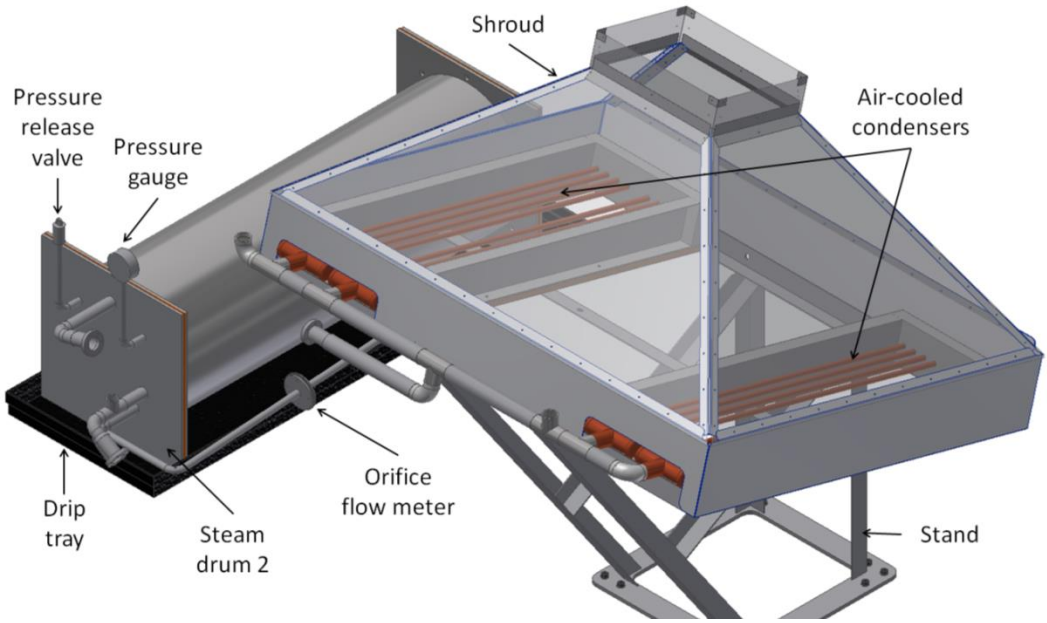


**Figure 33:** Tertiary loop system design

Numerous experiments were carried out on the tertiray loop experimental set up using the experimental procedure outlined in Appendix G. The results from these experiments are discussed in the next section and used in the validation process of the theoretical models developed in Section 3.

# 5 RESULTS

This chapter covers the results from the tertiary loop's experimental set-up, as discussed in Section 4.3, to meet objective 1. The theoretical model, presented in Section 3.2, to meet objective 2, is used build the tertiary loop's transient semi-explicit simulation as discussed in Appendix B. The results are presented, to meet objective 3 and compared to the experimental results, to meet objective 4. The mass flow rate of the primary loop's theoretical simulation is compared to the experimental results, to meet objective 5. Finally, a steady-state implicit numerical simulation of the three loops combined is then considered to meet objective 6.

## 5.1. TERTIARY LOOP RESULTS

The results of the tertiary loop are covered in this section, starting with a look at important observations. Next, a semi-empirical formula is developed for the heat lost from the tertiary loop, this is then used in an energy balance to establish confidence in the experimental results. A comparison is done between the theoretically and experimentally determined convection heat transfer coefficients for the outside of the air-cooled condenser. The temperature response in the steam drum and condensers is then analysed, by comparing the experimental and theoretical results. The experimental and theoretical mass flow rate response is then analysed and the x- and y-components of the condensate mass flow rate theoretical model observed. The thickness of the condensate film and the heat transfer rate at different points along the tube are investigated.

### 5.1.1. Observations

This section deals with the observations made during the tertiary loop experiments. The experimental set-up was run with power inputs of 0.35, 1.00, 1.15, 2.19, 2.95, 4.43, 4.66, 5.00 and 5.59 kW. The temperatures and pressure drop over the orifice flow meter were recorded at a rate of 0.1 Hz. The first three experiments did not reach a steady state condition despite fairly long run times. The experiments with a power input of 2.19 kW upward all had their temperatures and mass flow rates level off and approaching or reaching a steady-state condition. Thus, the first three experiments are used in the energy balance in Section 5.1.3 but they are not analysed further. Video recordings were made of the bubble development and propagation in the steam drum. The size and placement of the heat exchanger made it difficult to capture the entire steam drum on camera, therefore, the lower and the upper halves of the steam drum are presented separately.

Boiling could be clearly heard and seen through the polycarbonate cover plate as soon as the electrical heating elements were switched on. There was a delay between when boiling starts and activation of fluid flow occurs. Activation is the point at which the evaporator pressure of a heat pipe is sufficiently high for

natural circulation to start. The experiment starts with the tertiary loop at a decent vacuum, with the liquid and vapour in equilibrium. As energy is added to the liquid through the heating elements, there is an incremental increase in temperature. The saturation pressure is higher than the local pressure and vapour formation ensues. The newly formed vapour enters the steam space and increases the local pressure in the steam drum until the liquid and vapour are once again in equilibrium. Since this is a continuous process, it is considered to be in a state of quasi-equilibrium. The system temperature and consequently its pressure continue to increase until it reaches its fluid flow activation conditions. At activation, the pressure in the steam drum is sufficient to overcome the friction, allowing fluid to flow into the riser and the condensers. This activation pressure increases with the power input into the system. A detailed discussion of the activation temperatures of the different experiments is covered in Section 5.1.5. Figure 34 shows the bubble propagation for 2.19 kW power input at 30 frames per second sometime after the flow is activated. A solitary bubble is formed on the heating element and grows in size while rising through the water.

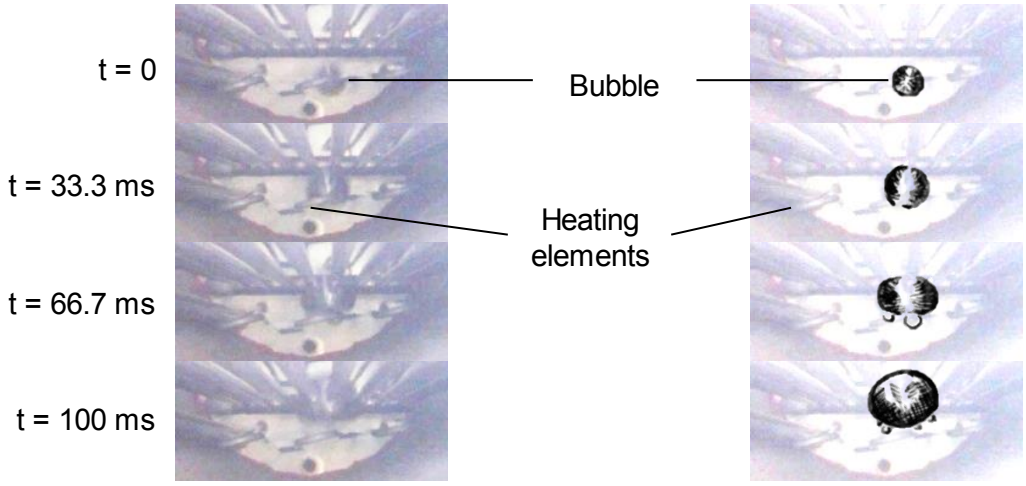


**Figure 34:** Bubble propagation at 2.19 kW

Figure 35 shows the bubble propagation above the secondary loop condenser for 2.19 kW power input at 15 frames per second. The frame rate is half of that from below the condenser in order to show its propagation in four frames. This implies that the bubble moves at a lower velocity. The liquid vapour interface is greatly agitated as each bubble breaks the surface and appears to be churning.

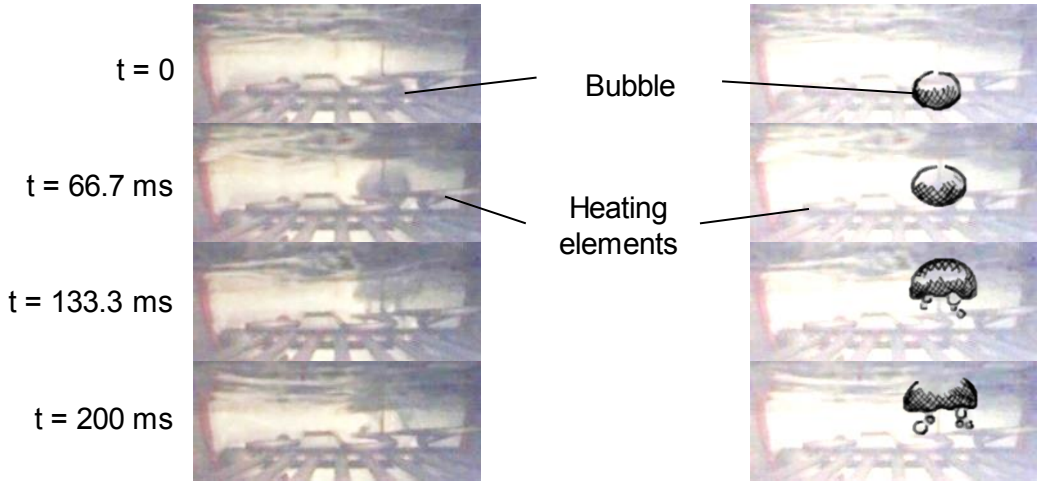


**Figure 35:** Bubble propagation at 2.19 kW

The bubble transforms from spherical to an oblate ellipsoidal cap shape due to shear force from the liquid. Smaller bubbles are caught in the eddy/vortex below the bubble and pulled upwards in its wake. The bubbles are large due to surface tension and low vapour velocity. As demonstrated by Mills and Ganesan (2009) the radius of the bubbles formed during nucleate boiling is directly proportional to the surface tension. At lower temperatures, such as those experienced at lower heat flux inputs, the surface tension is higher and larger bubbles are expected. Kirkpatrick (1974) demonstrates that bubble velocity is a significant factor in bubble coalescence, with lower velocities allowing rapid coalescence. Thus, the bubble velocity is sufficiently small at low heat fluxes to allow the small bubbles formed on the heating element to merge into a large bubble. This was found to be characteristic of the bubble formation at lower heat fluxes. At higher heat fluxes, the bubbles formed are smaller and more frequent as shown in Figure 36. It shows the bubble propagation for a power input of 4.43 kW at 30 frames per second. Constant streams of small bubbles rise from the heating elements.

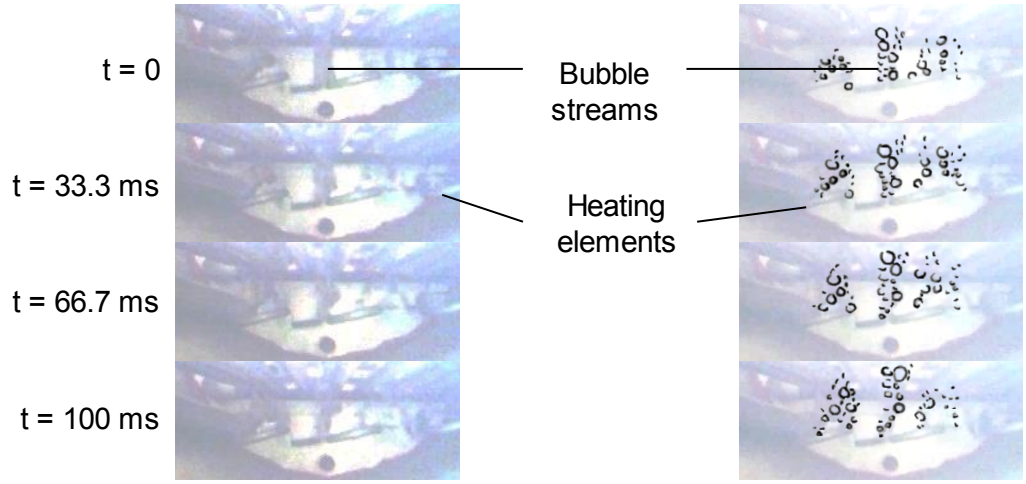


**Figure 36:** Bubble propagation at 4.43 kW

Figure 37 shows the bubble propagation above the condenser for a power input of 4.43 kW at 30 frames per second. The liquid vapour interface is relatively smooth with the small bubbles causing little agitation to it. The bubble sizes developed at 4.43 kW are much smaller than those developed at 2.19 kW. Due to the higher rate of heat transfer from the heating elements, higher bubble velocities were experienced, resulting in bubbles releasing from the heating element and rising to the surface with little to no coalescence. This is further ensured by the higher surface tension holding the bubble together.

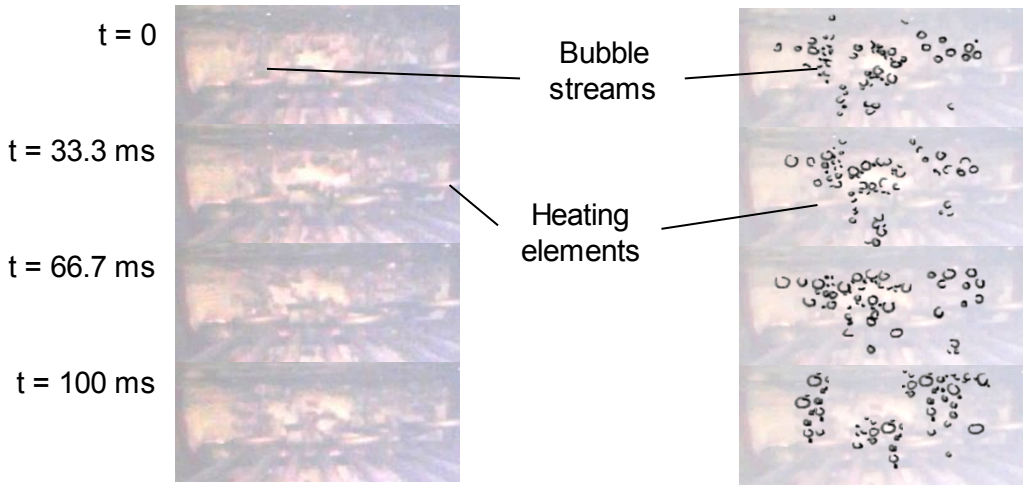


**Figure 37:** Bubble propagation at 4.43 kW

In order to carry out the energy balance a formula is needed for the heat lost from the tertiary loop.

### 5.1.2. Heat Loss semi-empirical characterisation

This section aims to develop a semi-empirical correlation for the heat lost from the tertiary loop to the environment, $\dot{Q}_{loss,T}$. The correlation was obtained by carrying out 'cool-down' experiments. The procedure involved recording the flow rate and temperature response of the tertiary loop after the power input was switched off once steady state conditions were reached. The steam drum has a sufficiently small height so it is assumed that stratification of the liquid will not affect the temperatures measured. Due to the passive nature of the tertiary loop, the air-cooled condensers would still be operational for some time after the heating elements were turned off. To ensure that the results would not be skewed by heat loss through the condensers, the data used was taken only once the flow rate had dropped to zero. This corresponds to no temperature rise in the air across the condensers. $\dot{Q}_{loss,T}$ is given in the form shown in Equation 5.1.1, where $U$ is the overall heat transfer coefficient.

$$\dot{Q}_{loss,T} = UA(\mathrm{T}_{sd2,v} - \mathrm{T}_{env}) \tag{5.1.1}$$

The formula for the conservation of energy for the tertiary loop is given in Equation 3.2.39. If $\dot{Q}_{elec} = 0, \dot{Q}_{out} = 0,$ and $\dot{m} = 0$ the energy conservation equation is reduced to Equation 5.1.2.

$$\frac{(mu)^{t+\Delta t} - (mu)^{t}}{\Delta t} = -\dot{Q}_{loss,T} \tag{5.1.2}$$

Applying Equation 5.1.2 to the steam drum and expressing the internal energy in terms of temperature and specific heat results in an equation for the heat lost to the environment, expressed in Equation 5.1.3.

$$\dot{Q}_{loss,T} = \frac{mC_v\left({T_{sd2}}^{t} - {T_{sd2}}^{t+\Delta t}\right)}{\Delta t} \tag{5.1.3}$$

The mass, $m$, and the specific heat, $Cv$, can be determined given the temperature and Equation 5.2.3 applied to the experimental data of the four 'cool-down' experiments. The results are plotted against $\mathrm{T}_{sd2,v} - \mathrm{T}_{env}$ in order to develop a correlation for $(UA)_{loss}$ as given in Equation 5.1.1. The results from the four experiments, having different starting and ambient temperatures are shown in Figure 38. The experimental results overlap each other and show similar relationships with the temperature difference.

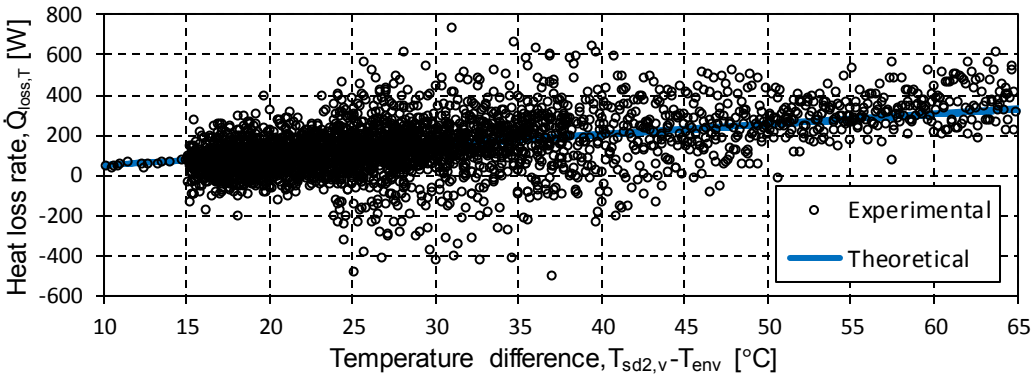


**Figure 38:** Energy loss characterisation curve

Placing a curve fit through the data using a linear profile and forcing the intercept through [0,0], results in the theoretical line plotted in Figure 38. Equation 5.1.1 can be rewritten in terms of the gradient as

$$\dot{Q}_{loss,T} = 5.06697\,(T_{sd2,v} - T_{env}) \tag{5.1.4}$$

An energy balance is done in the next section to validate the heat loss equation developed in Equation 5.1.4.

### 5.1.3. Energy balance

An energy account was done on the tertiary loop to establish confidence in the experimental results. Figure 39a shows $\dot{Q}_{out}$ vs $\dot{Q}_{in}$ at the steady state conditions of each of the experimental runs with error bands of 15%. There is a good correlation between the power in and power out with only three experiments outside the 15% bound shown by the dotted line. These three experiments did not achieve steady state conditions but after numerous hours of running were still mutable. These three experiments had power inputs below 1.3 kW.

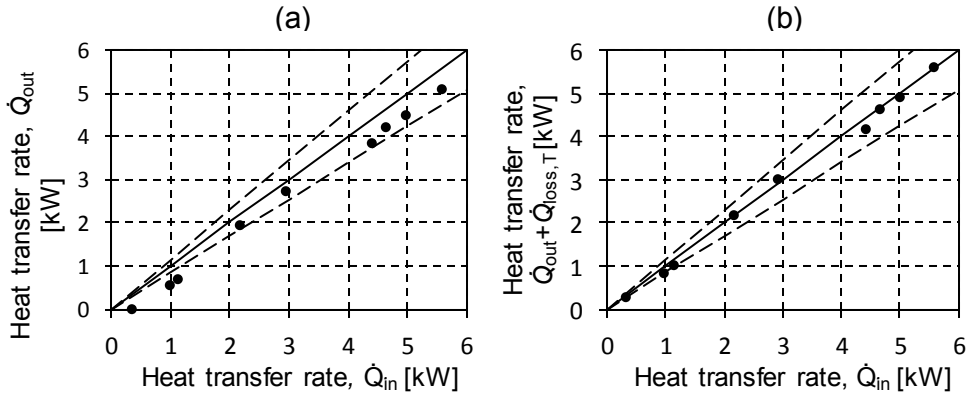


**Figure 39:** Heat transfer rate in vs. a) Heat transfer rate out b) Heat transfer rate out plus heat transfer rate lost

The rate of heat transfer loss to the environment, $\dot{Q}_{loss,T}$, was calculated at the experimental conditions using Equation 5.1.4 and is added to $\dot{Q}_{out}$ in Figure 39b. The results sit close to the diagonal line showing that $\dot{Q}_{out} + \dot{Q}_{loss,T}$ corresponds well to $\dot{Q}_{in}$. Confidence in the expression for heat lost to the environment and the experimental results is established. The heat transfer coefficient can now be investigated.

### 5.1.4. Air-cooled condenser heat transfer coefficient

The convection heat transfer coefficient, $h_{tco}$, on the outside of the air-cooled condenser is discussed in this section. When the experiments had reached steady state conditions a range of data was collected for each. From this data, the theoretical heat transfer coefficient is determined using Equation 3.2.46 with property functions determined at the experimental conditions. The experimental heat transfer coefficient is determined by making the heat transfer coefficient the subject of formula for Equation 3.2.41 as shown in Equation 5.1.5 below.

$$h_{tco} = 1 \Big/ \left( \frac{T_{sd2} - T_{env}}{\dot{Q}_{out}} - R_w - R_{film} \right) \times A_{fin} \eta_{fin} \tag{5.1.5}$$

The thermal resistance of the film, $R_{film}$ given in Equation 3.2.43 is determined at a film thickness of 30 μm. The thermal resistance of the copper tube wall, $R_w$, is calculated using Equation 3.2.44. Figure 40 shows the theoretical heat transfer coefficients plotted against the experimental values with error bands of 15%.

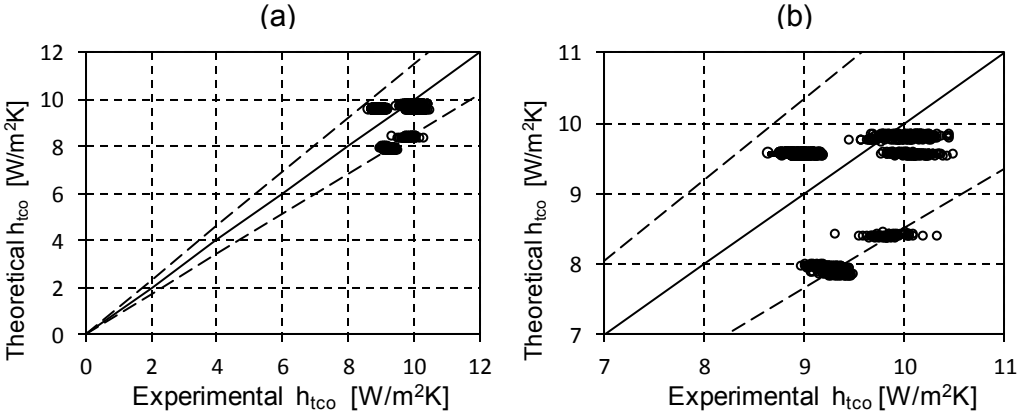


**Figure 40:** Comparison of experimental and theoretical heat transfer coefficient

The results in Figure 40 demonstrate a good correlation between the experimental and theoretical values. This instils confidence in the expression for the heat transfer coefficient on the outside of the air-cooled condenser. This expression is used in the numerical simulation, and its results are discussed in the remainder of this section.

### 5.1.5. Temperature response

In this section the temperature response of the experimental set-up and the theoretical simulations are discussed. The temperatures within the steam drum and the condensers are analysed and simulation and experimental results are compared.

The temperature response in the steam drum for different power inputs are shown in Figure 41. There is an increase in temperature with an almost constant gradient at the beginning of all of the experiments. This is as expected since the heat flux into the system is constant with only a small amount being lost to the environment. Activation then takes place and the gradient decreases with time. The temperatures then levels off which shows a balance between the thermal energy into and the thermal energy extracted from the system. The transition between these two regimes is more gradual for the profiles with lower power inputs and more pronounced at the higher power inputs. This is due to the differing activation temperatures seen during the experiments.

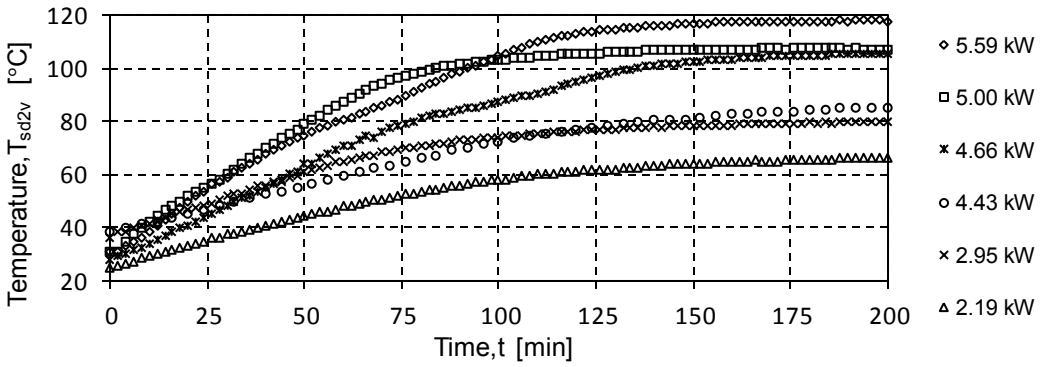


**Figure 41:** Steam drum temperatures for different power inputs

The temperature profiles from the numerical simulation are shown in Figure 42. They match the experimental curves well except for the sudden change in gradient at activation. This demonstrates the ability of the numerical simulation to determine the thermal behaviour within the steam drum.

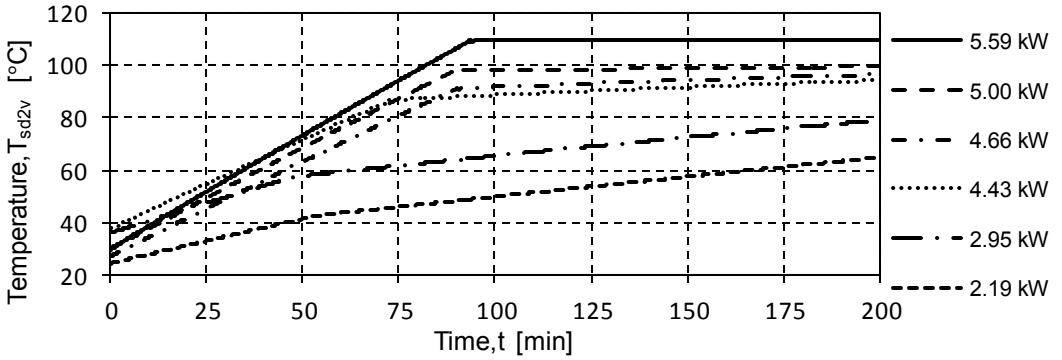


**Figure 42:** Steam drum temperatures for the numerical simulation

The experimental and theoretically determined steam drum temperatures at 200 minutes are shown in Figure 43. The theoretical values match the experimental values well at low power inputs but under-predict the temperature at higher power inputs. The average error between the theoretical and experimental values is determined to be 5.73% using the general Equation 5.1.6.

$$error = abs\left(\frac{x_{theo}-x_{exp}}{x_{exp}}\right)\times 100 \qquad (5.1.6)$$

The error is expressed in terms of the general theoretical and experimental values, $x_{theo}$ and $x_{exp}$, since it is going to be applied to all the results in the remainder of this section.

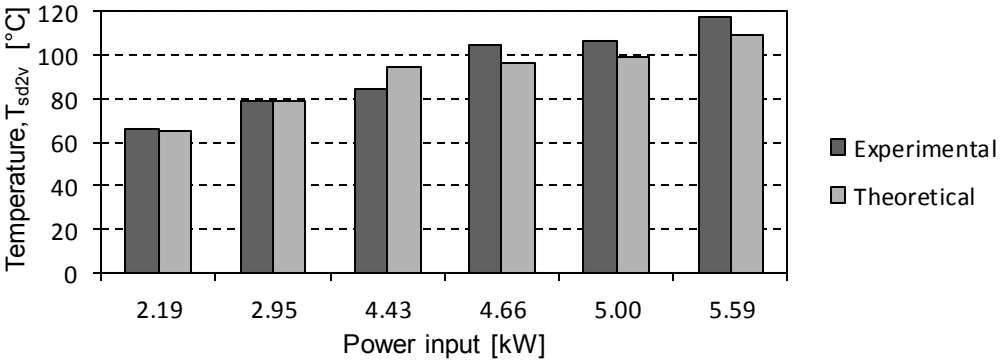


**Figure 43:** Steam drum temperatures at 200 min

The temperature within the condensers is measured at the inlet, $T_{ci}$, a quarter of the way along its length, $T_{c1}$, halfway along its length, $T_{c2}$, three quarters of the way along its length, $T_{c3}$, and at the outlet, $T_{co}$. The inlet and outlet thermocouples are placed within the condenser manifolds, whereas the three measurements along the condenser length are taken on the outside of the condenser tubes due to the small pipe diameter and small spaces between the fins. While the three measurements along the length are not an exact

measurement of the temperature inside the condensers, they give a decent indication of the behaviour within the condenser.

The temperature profiles within the condensers are shown in Figure 44, Figure 45 and Figure 46. Activation is indicated when the $T_{ci}$ approaches $T_{sd2v}$. This is more delayed and the activation temperature is higher with each increase in power.

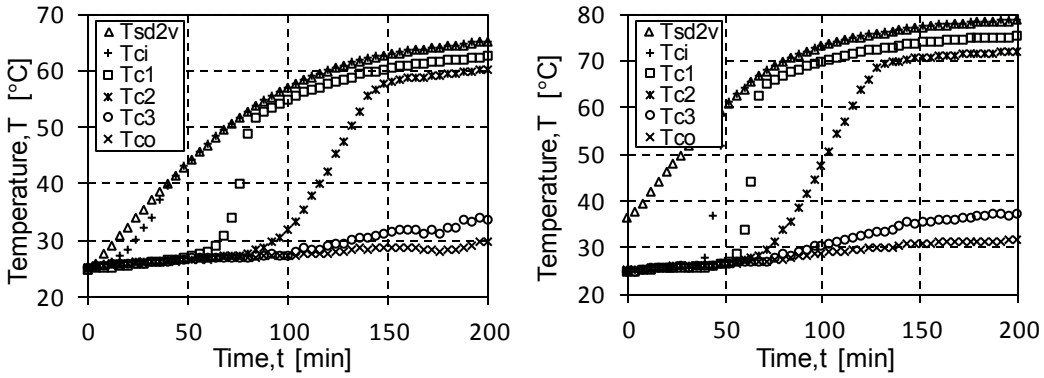


**Figure 44:** Condenser temperatures for a) 2.19 kW and b) 2.95 kW input

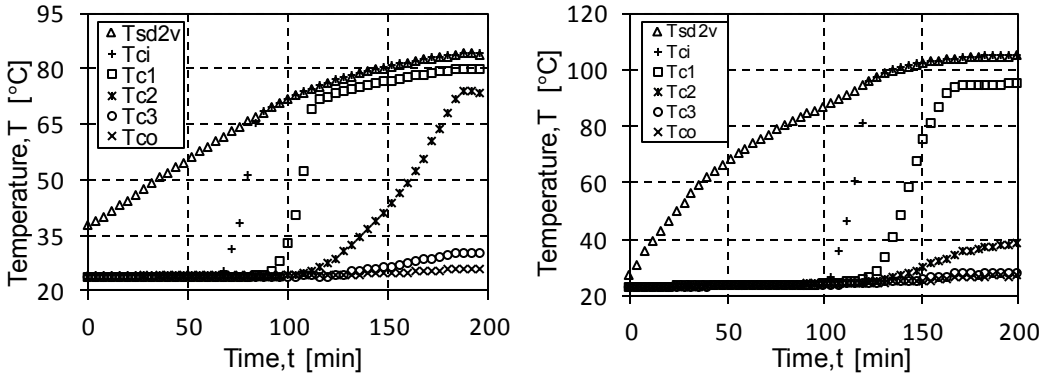


**Figure 45:** Condenser temperatures for a) 4.43 kW and b) 4.66 kW input

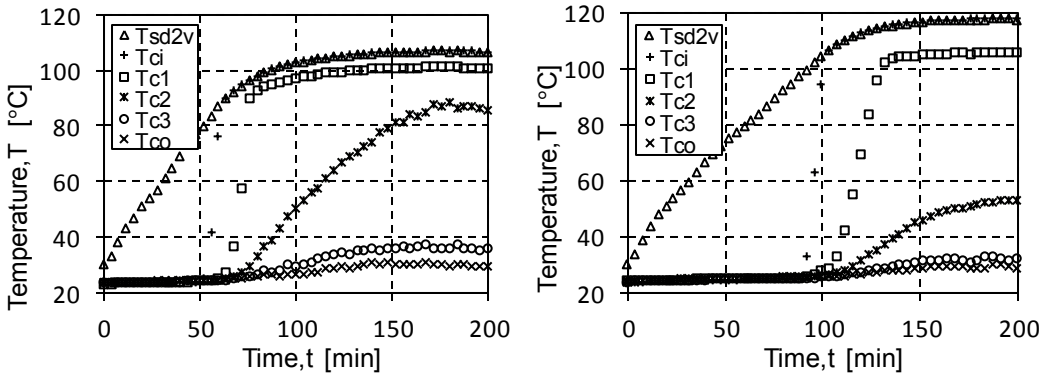


**Figure 46:** Condenser temperatures for a) 5.00 kW and b) 5.59 kW input

The numerical simulation of the condenser temperatures are shown in Figure 47, Figure 48 and Figure 49.

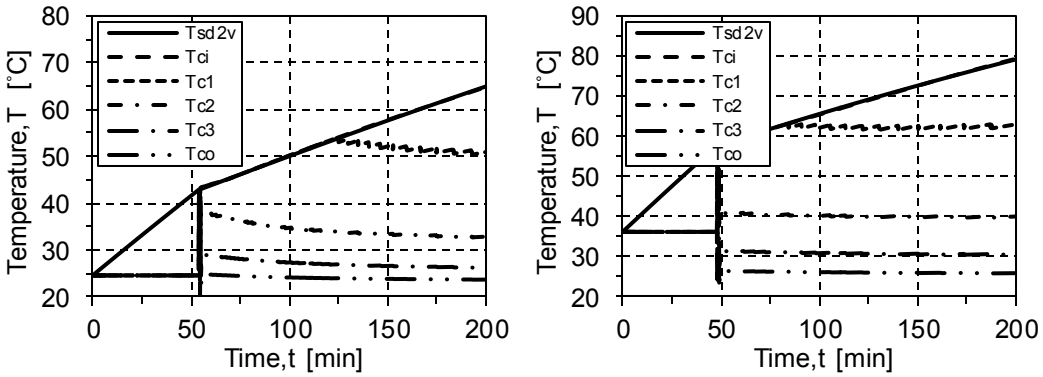


**Figure 47:** Condenser temperatures for a) 2.19 kW and b) 2.95 kW input

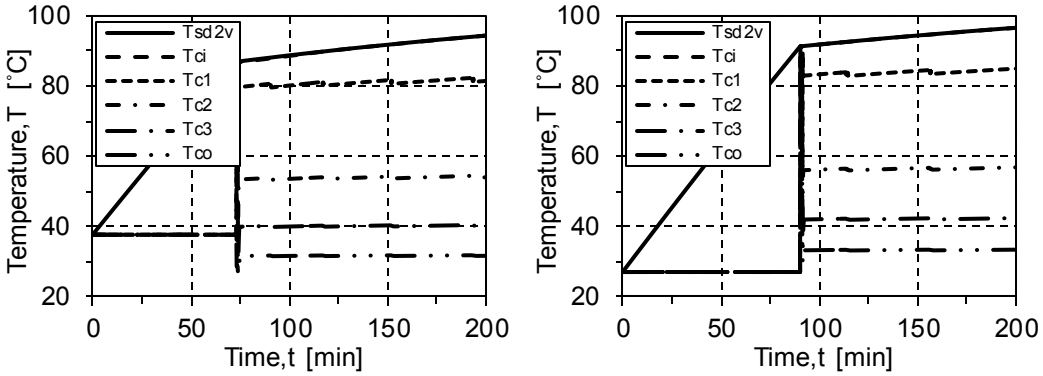


**Figure 48:** Condenser temperatures for a) 4.43 kW and b) 4.66 kW input

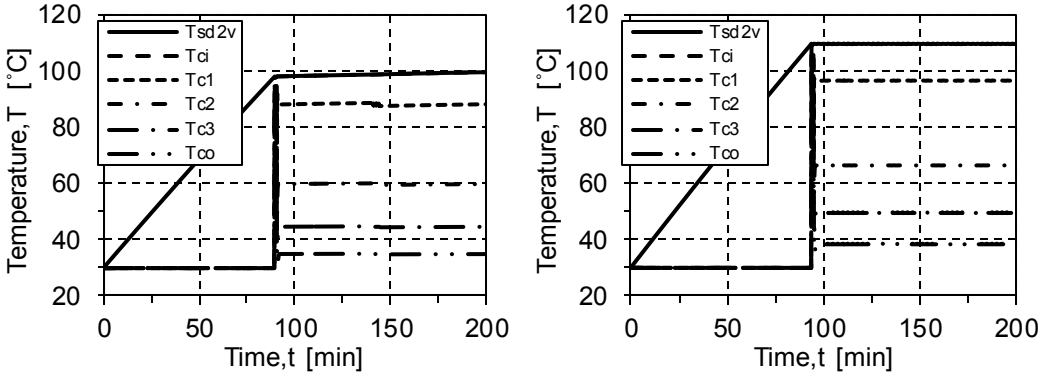


**Figure 49:** Condenser temperatures for a) 5.00 kW and b) 5.59 kW input

Looking at the graphs, the activation steam drum temperatures are approximately 40°C, 61°C, 65°C, 97°C, 90°C and 106°C. The activation of the tertiary loop is not constant and seems to be influenced by the power input. The activation temperatures and pressures are greater for higher power inputs. Theoretically,

this could be due to a slip-stick effect of the steam moving from the 400 mm diameter steam space to the 42 mm diameter riser. There is a further delay until $T_{c1}$ rises to its steady state value. This may be because it is attached to the outside of the condenser and it takes time for the heat to be registered by the thermocouple. As the steam rises it will lose heat to the metal riser and may condense before reaching the condensers. The condensers themselves will absorb heat from the steam resulting in the gradual increases seen in the graphs.

The simulation results match the experimental results adequately, but do not successfully capture the activation transition, which is more gradual. This is because the numerical simulation does not take the heat capacity of the metal components into account. They may be thin walled but the lengths of the riser and condensers are substantial. The mass flow rate driving the flow through the condensers is discussed in the next section.

### 5.1.6. Mass flow rate response

The mass flow rate response of the tertiary loop is discussed in this section. A comparative study is made between the different experimental results and then between them and the simulation results. Finally, observations are made of how the x- and y-components of the condensate mass flow rate change spatially.

The experimental mass flow rate responses of the tertiary loop, as measured by the orifice flow meter, for different power inputs are shown in Figure 50. There is a gradual increase in the flow rate at the start of the experiments for low power inputs, such as 2.19 and 2.95 kW. The gradient increases as the power input is increased, with an almost vertical start up for 5.59 kW.

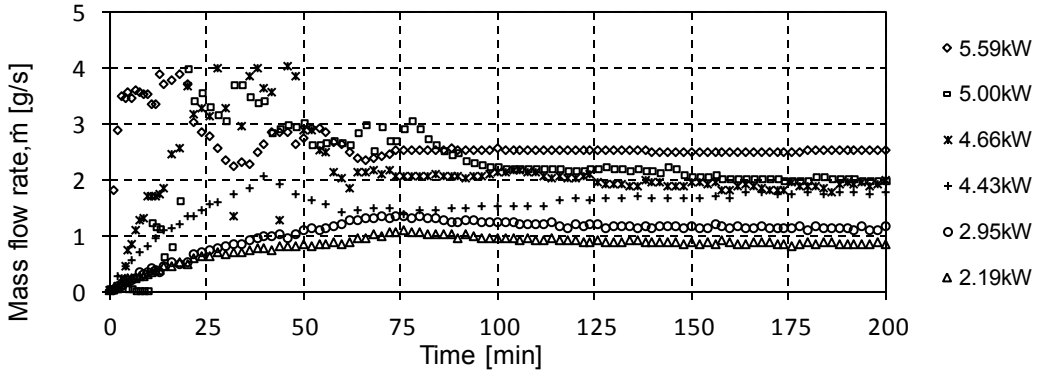


**Figure 50:** Mass flow rate responses for different power inputs

The flow rate response is sporadic in the beginning of the experiments before activation. The boiling is balanced by the condensation at that point as the flow is in thermodynamic equilibrium. This may be the instability related to density wave oscillations that is shown to precede stable two-phase flow in Figure 7. At 100 minutes, all the graphs have levelled off because the tertiary loop has activated. The stable operation during activation can be attributed to the high

level of sub-cooling that takes place in the condensers. The numerical simulation flow rate response for different heat inputs are shown in Figure 51. The simulation results match the experimental results adequately after activation, but fail to capture the behaviour at the start of the experiments. A better understanding is required of the quasi-equilibrium boiling and condensation phenomena in order to effectively simulate it.

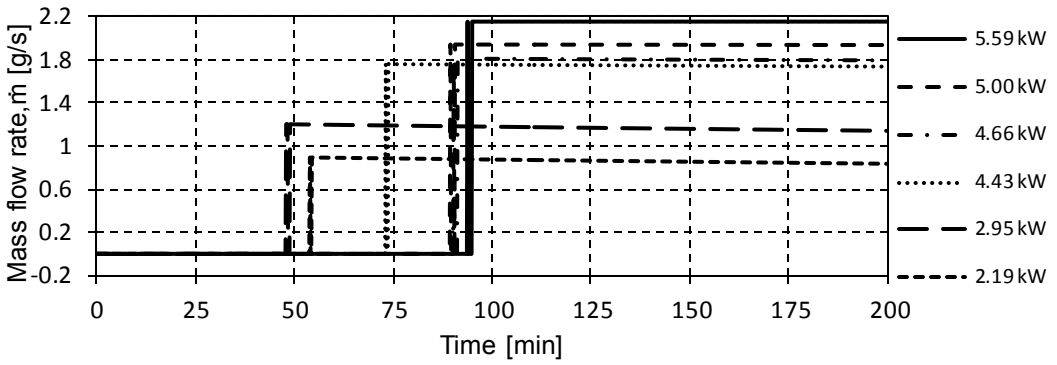


**Figure 51:** Numerical simulation mass flow responses

The experimental and theoretically determined mass flow rates at 200 minutes are shown in Figure 52. The theoretical values match the experimental values well at low power inputs but under-predict the temperature at higher power inputs, with an average error of 1.86%.

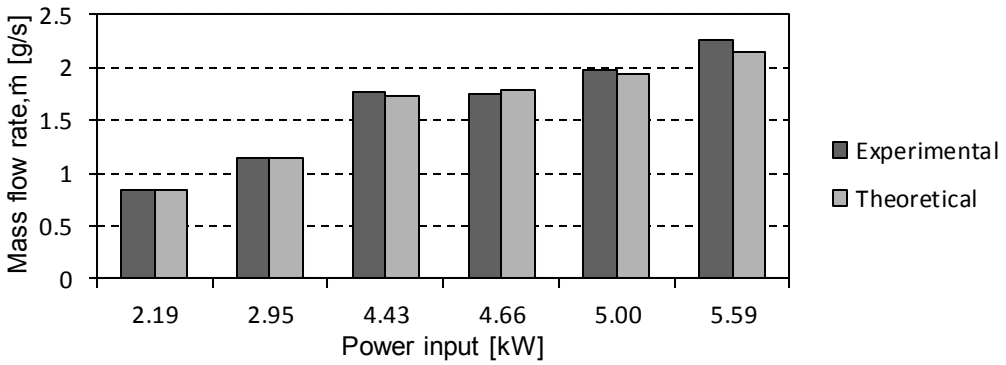


**Figure 52:** Mass flow rates at 200 min

The simulation in Figure 51 at first glance shows a step increase at activation but as shown in the zoomed in sections in Figure 53, this is not the case.

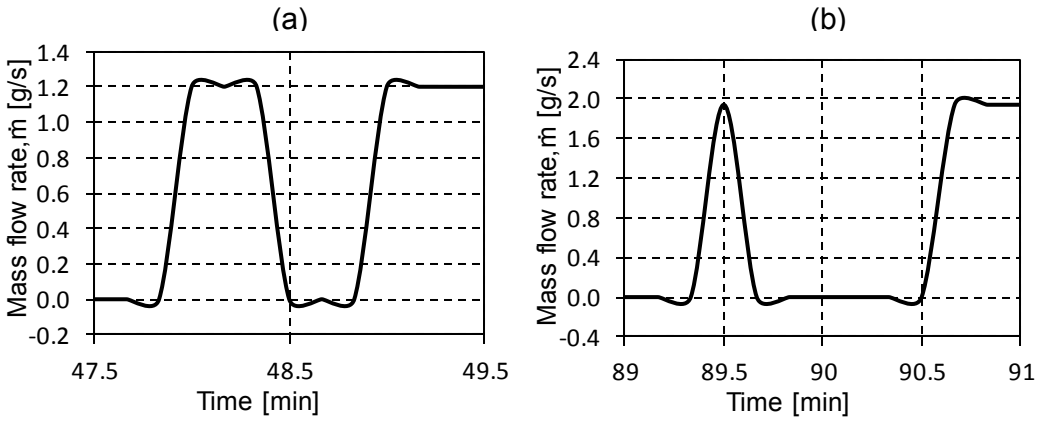


**Figure 53:** Flow rate response at activation for the a) 2.95 kW and b) 5.00 kW

The mass flow rate rises steeply in response to the increase in the condenser temperatures. It then falls to approximately zero as the air temperature increases in response to the heat transferred to it. The stabilisation of the condenser and air temperatures allows the flow rate to level off. After this, it decreases gradually until it reaches the steady-state value.

The pressure release valve opened during the final experiment with a power input of 5.59 kW, and may have affected the results recorded. For a more detailed look at what happens inside the condenser, we will use the numerical simulation results from 5.00 kW power input because it matches the experimental results sufficiently. The flow rate discussed so far is the overall flow rate circulating through the loop but the behaviour of the flow inside of the condenser tubes at steady-state is now discussed.

The x-component of flow rate, $\dot{m}_x$, is shown in Figure 54. High flow rates occur at high values of y, that is, at the lowest point in the pipe. This is where the condensate will accumulate and run in a rivulet. There is a clear decrease in flow rate along the length of the pipe. This is because the rate of condensation is highest in the beginning when the temperatures are the highest, as shown in Figure 57.

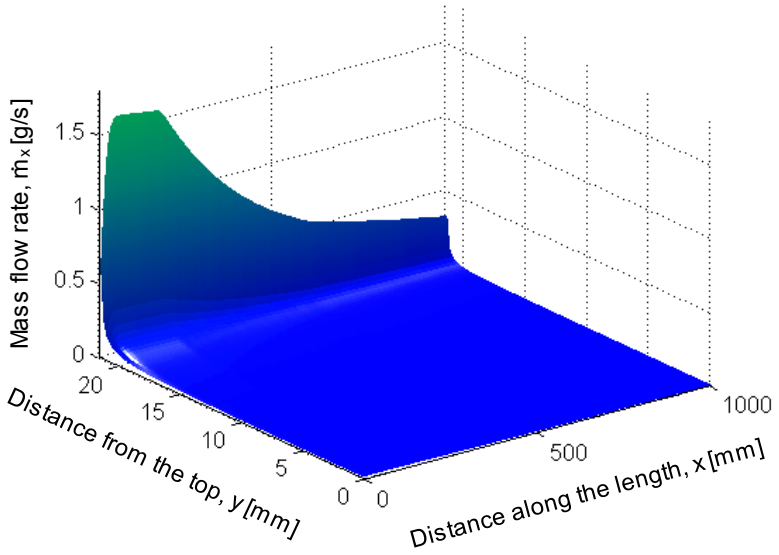


**Figure 54:** Mass flow rate x-component as a function of position in the tube for 5 kW

The y-component of flow rate, $\dot{m}_y$, is shown in Figure 55. It has a much different profile to that in the x- component. There is a similarity in that the highest values are evident towards the entrance to the tube where the flow is at saturated conditions and the condensation rate is the highest. The values grow quickly at the entrance of the tube as the condensate accumulates and forms a film. The y-component of gravity, $g_y = 9.476 \sin\theta$, is larger than the x-component, $g_x = 2.539$. This might explain why the values of $\dot{m}_y$ are much higher than those of $\dot{m}_x$. $\mathrm{Sin}\,\theta$ varies from zero at the top of the tube to a maximum of unity midway between the top and bottom and reduces back to zero at the bottom, as seen in the change in gradient.

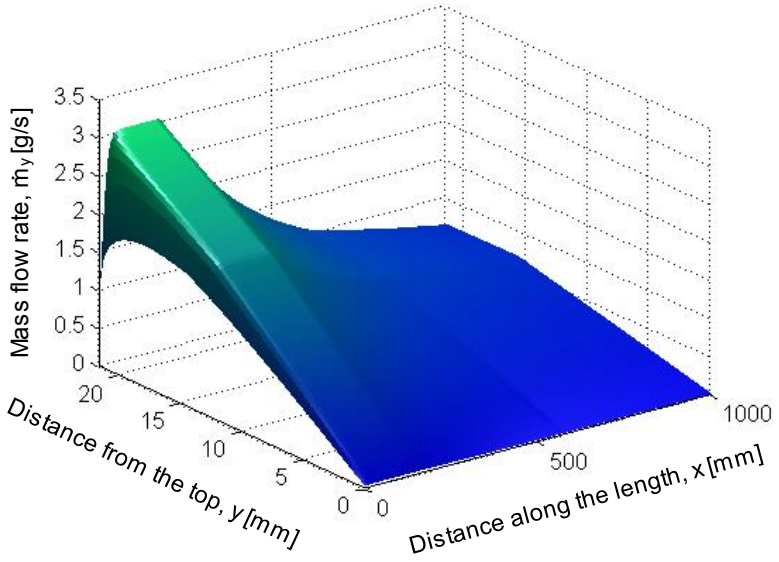


**Figure 55:** Mass flow rate y-component as a function of position in the tube for 5 kW

### 5.1.7. Heat transfer rate

The heat transfer at each control volume is shown in Figure 56, at steady state conditions with a 5 kW power input. This follows the temperature profile very closely, as shown in Figure 57, showing that the steam drum temperature has the most significant effect on the heat transfer rate through the condenser. However, there is a drop in heat transfer at the bottom of the tube. This is due to the steep increase in film thickness as seen in Figure 58, which also has a notable effect on the heat transfer. The heat transfer rate is decreased through an increase in the thermal resistance, due to conduction through the condensate film thickness.

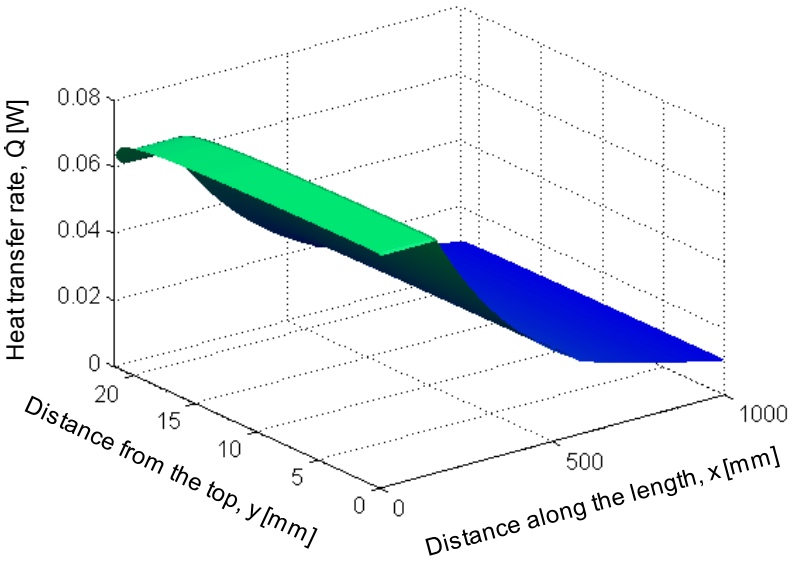


**Figure 56:** Heat transfer distribution at different positions in the tube for 5 kW

The temperature at each control volume is shown in Figure 57 and it changes only in the x-direction. The temperature remains very close to the steam drum temperature of 99.6 °C for a small section of the condenser length. From 165.4 mm along the condenser, sub-cooling takes place. The temperature falls with a decreasing gradient until the condensate leaves the condenser at 34.9 °C.

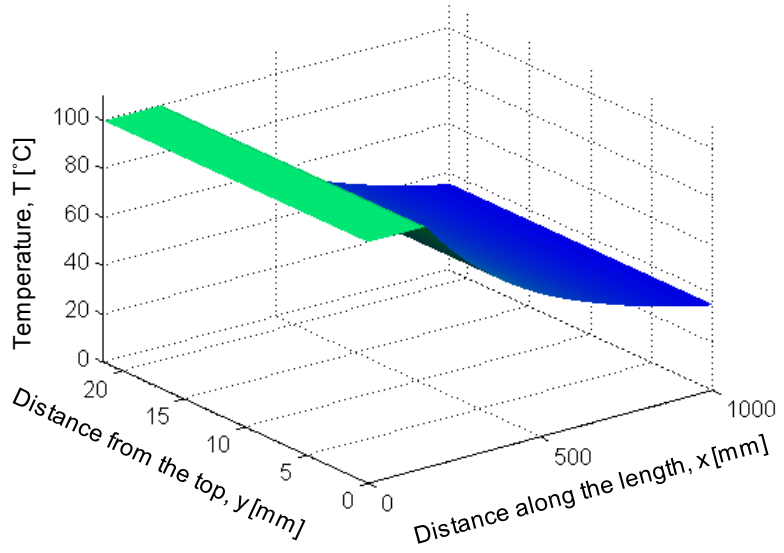


**Figure 57:** Temperature profile for 5 kW input

Figure 58 agrees with the conclusions from Section 5.1.6 that the condensate accumulates and runs in a rivulet at the lowest point in the pipe.

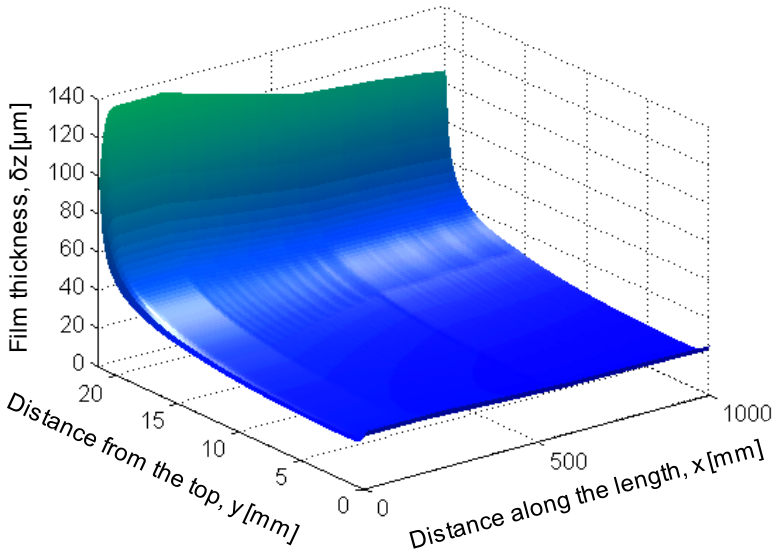


**Figure 58:** Film thickness of the condensate at different positions in the tube for 5 kW

Figure 59 gives an indication of how the film thickness would look in a section view of the condenser tube. The film is very thick at the bottom of the tube and thin along the sides. There is an increase at the top of the tube that is probably due to the gravitational force acting perpendicular to the surface. This would give the condensate formed there a tendency to drip rather than run along the sides.

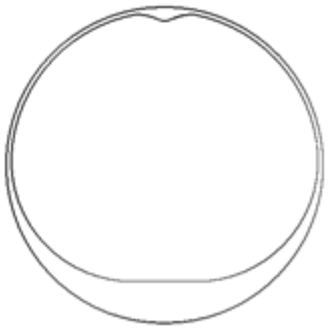

**Figure 59:** Film thickness represented inside the pipe

This is similar to the film thickness distribution for the other heat inputs with slight variations in the values. The average film thickness across the surface for the various experimental heat inputs is shown in Table 2. There is an increase in film thickness with an increase in the power input.

**Table 2:** Film thickness variation with heat input

| Input | 2.19 kW | 2.95 kW | 4.43 kW | 4.66 kW | 5.00 kW | 5.59 kW |
|---|---|---|---|---|---|---|
| $\delta z\ [\mu m]$ | 27.6181 | 28.6932 | 30.6682 | 30.7400 | 31.1878 | 31.9994 |

5.1.8. Air temperature and mass flow rate response

The temperature and mass flow rate response of the experimental set-up and the theoretical simulations for the air are discussed in this section. The laboratory in which the experiments were carried out has a door and windows that were left open to ensure the temperature would not rise excessively. This means that drafts may affect the flow rate through the condensers, which has a direct effect on the temperature.

The experimentally and theoretically determined air outlet temperatures at 200 minutes are shown in Figure 60. The theoretical values show an increase in value with increase in input power. The air temperatures measured at the outlet of the shroud during the experiments do not show a clear relationship with the power input. The average error between the experimental and theoretical results is 10.67%.

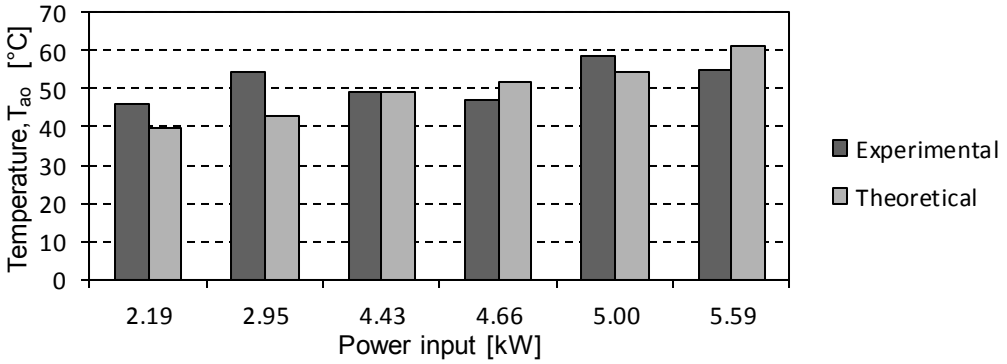


**Figure 60:** Air outlet temperatures at 200 min

Once again, the magnitude of the flow rate at 200 minutes does not correlate with the heat input as shown in Figure 61. The theoretical values show an increase with input power but the experimental results seem to be haphazard with an average error of 16.71%.

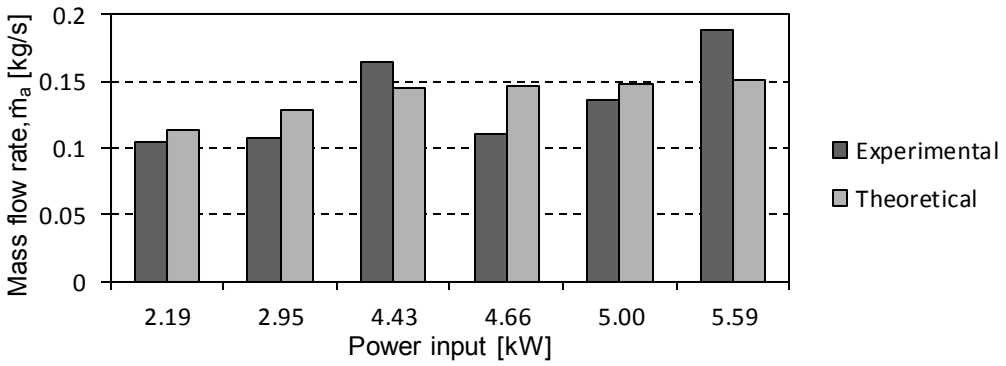


**Figure 61:** Air mass flow rate at 200 min

The irregularity in the air temperatures and mass flow rates highlights the sensitivity of the air-cooled condensers, but also shows a level of versatility. The temperatures and mass flow rates adjust so that the condensers still transfer the heat released through condensation to the air.

### 5.1.9. Numerical stability

The numerical stability of the tertiary loop numerical simulation model is determined in this section. This involves investigating the convergence of the solution with changes in mesh size, time step size and the convergence criteria. The discretisation and iteration independence investigations were performed with a constant power input of 5 kW.

The solution space was discretised into a structured mesh with quad cells. The grid size was systematically refined from 7.49 mm to 0.47 mm with a time step of 10 s and truncation criteria of $10^{-9}$. The results are shown in Table 3 where each value is expressed as a percentage of the value at 0.23 mm. The solution does indeed converge as the grid size is refined as each refinement takes the results closer to the results for 0.23 mm.

**Table 3:** Grid convergence data

| Grid size [mm] | 7.49 | 3.74 | 1.87 | 0.94 | 0.47 | 0.23 |
|---|---|---|---|---|---|---|
| Steam drum temperature | 104.47% | 103.92% | 103.24% | 102.36% | 101.28% | 100% |
| Steam mass flow rate | 99.29% | 99.38% | 99.49% | 99.63% | 99.80% | 100% |
| Heat transfer rate out | 95.79% | 95.95% | 96.97% | 97.97% | 98.98% | 100% |
| Air out temperature | 91.38% | 91.92% | 93.75% | 95.67% | 97.75% | 100% |

The number of control volumes was increased and the flow rate changed as shown in Figure 62. The average value does not change significantly with grid refinement, but the shape of the distribution does.

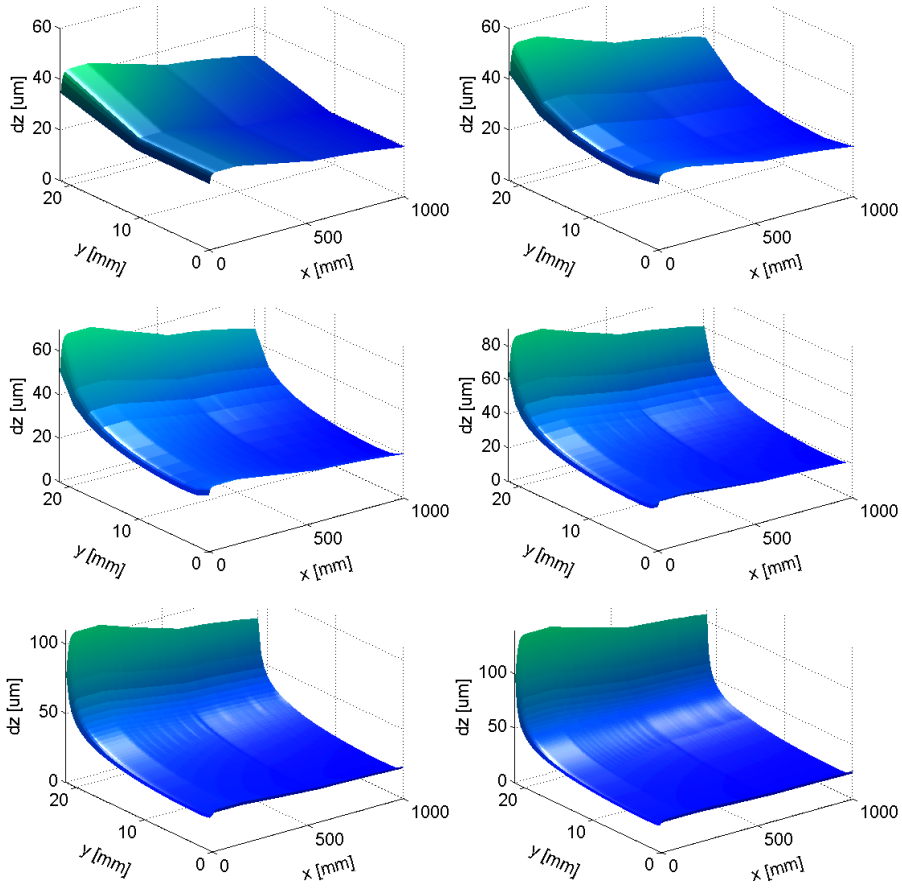


**Figure 62:** Film thickness distribution for different control volume sizes for 5 kW

Although further refinement may have resulted in slightly better results, the increase in computing time of the simulation would have been excessive. Discretisation convergence for time step involved systematically refining the size of the time step from 20 s down to 0.1 s with a grid size of 7.49 mm and truncation criteria of $10^{-9}$. The results are shown in Table 4 and the solution converges with declining time step size. The differences between using 0.5 s and 0.1 s was so small that a time step size of 0.5 s was used in the final simulations and should result in a miniscule discretisation error.

**Table 4:** Time step convergence data

| Time step [s] | 20 | 10 | 5 | 1 | 0.5 | 0.1 |
|---|---|---|---|---|---|---|
| Steam drum temperature | 100.06% | 95.76% | 100.61% | 100.60% | 100% | 100% |
| Steam mass flow rate | 99.99% | 100.70% | 100.30% | 100.30% | 100% | 100% |
| Heat transfer rate out | 100.04% | 105.36% | 99.62% | 99.61% | 100% | 100% |
| Air out temperature | 100.03% | 109.46% | 106.32% | 106.32% | 100% | 100% |

The film thickness is varied until a balance is established in the rate of condensation and the flow rates in and out of the control volume. Iterative convergence of the truncation criteria for the mass flow rate residual was systematically refined from $10^{-5}$ to $10^{-15}$, with a grid size of 7.49 mm and step from 10 s, and the results are shown in Table 5.

**Table 5:** Iterative residual convergence

| Convergence criteria | $10^{-5}$ | $10^{-7}$ | $10^{-9}$ | $10^{-11}$ | $10^{-13}$ | $10^{-15}$ |
|---|---|---|---|---|---|---|
| Steam drum temperature | 100.44% | 99.99% | 100.00% | 100% | 100% | 100% |
| Steam mass flow rate | 99.93% | 100.00% | 100.00% | 100% | 100% | 100% |
| Heat transfer rate out | 98.81% | 99.99% | 100.00% | 100% | 100% | 100% |
| Air out temperature | 98.23% | 99.98% | 99.99% | 100% | 100% | 100% |

Thus, the model is verified through quantification of the errors (Versteeg *et al*., 2007) and is shown to be numerically stable.

### 5.1.10 Sensitivty Analysis

A sensitivity analysis for the quantification of input uncertainty was carried out on the numerical simulation developed for the tertiary loop. The simulation was run multiple times while the following input data were varied by ±10% and ±20%:

- Mass of fluid in the tertiary loop, $m_t = 90.3$ kg
- Angle at which the condensers are placed, $\varphi = 15$ °
- Thermal conductivity of copper, $k_{copper} = 385$ W/mK
- Fin efficiency as used in the heat transfer calculations, $\eta_{fin} = 95\%$
- Temperature of the air around the loop, $T_{env} = 22$ °C

Table 6 shows how varying the inputs affected the steam drum temperature, Table 7 shows how varying the inputs affected the mass flow rate and Table 8 shows how varying the inputs affected the heat extracted through the air-cooled condensers. The values are given as a percentage of the base case.

**Table 6:** Sensitivity analysis with respect to steam drum temperature

| | 80% | 90% | 110% | 120% |
|---|---|---|---|---|
| $m_t$ [kg] | 102.035% | 100.892% | 99.192% | 98.387% |
| $\varphi$ [°] | 100.007% | 100.003% | 99.996% | 99.992% |
| $k_{copper}$ [W/mK] | 99.977% | 99.989% | 100.009% | 100.015% |
| $\eta_{fin}$ [%] | 94.605% | 97.365% | 110.464% | 124.817% |
| $T_{env}$ [°C] | 99.278% | 99.638% | 100.328% | 100.718% |

**Table 7:** Sensitivity analysis with respect to mass flow rate

| | 80% | 90% | 110% | 120% |
|---|---|---|---|---|
| $m_t$ [kg] | 99.662% | 99.852% | 100.134% | 100.268% |
| $\varphi$ [°] | 99.998% | 99.999% | 100.001% | 100.001% |
| $k_{copper}$ [W/mK] | 100.004% | 100.002% | 99.998% | 99.997% |
| $\eta_{fin}$ [%] | 100.900% | 100.438% | 98.283% | 95.990% |
| $T_{env}$ [°C] | 99.630% | 99.815% | 100.198% | 100.370% |

**Table 8:** Sensitivity analysis with respect to heat transfer out

| | 80% | 90% | 110% | 120% |
|---|---|---|---|---|
| $m_t$ [kg] | 100.336% | 100.234% | 99.466% | 98.928% |
| $\varphi$ [°] | 99.994% | 99.996% | 100.003% | 100.007% |
| $k_{copper}$ [W/mK] | 100.010% | 100.005% | 99.997% | 99.993% |
| $\eta_{fin}$ [%] | 106.940% | 103.413% | 85.210% | 64.790% |
| $T_{env}$ [°C] | 100.495% | 100.216% | 99.744% | 99.318% |

The mass of fluid in the tertiary loop, $m_{tertiary}$, significantly affects the steam drum temperature. This is because the mass would affect the amount of time that it would take the system to reach steady state. The mass flow rate and heat transfer rate out are only affected slightly. The steam drum was not filled to the exact same volume for all of the experiments. This could explain the deviations between the recorded and simulated results.

The angle at which the condensers are placed and the thermal conductivity of copper have minimal effect on the temperature, mass flow rate and the heat transfer rate within the tertiary loop, so it can be concluded that the system is not sensitive to them and slight errors in the input values won't be detrimental to the simulation.

Fin efficiency, as used in the heat transfer calculations, has a large effect on the steam drum temperature and heat transfer rate, especially when it is increased. The simulation is therefore very sensitive to the fin efficiency and care must be taken in its determination. The error in the temperature and mass flow rates were calculated as 5.73% and 1.86%, respectively which means that the selection of a fin efficiency of 95% is acceptable.

The temperature of the environment around the loop has a relatively small effect on the temperature, mass flow rate and the heat transfer rate within the tertiary loop. As expected, a lower room temperature results in higher heat transfer and lower steam drum temperature experienced in the tertiary loop.

The sensitivity analysis and physical model certainty are the basis for verification and validation of the numerical simulation. Physical model certainty is demonstrated by the low percentage errors determined in the preceding sections of the thesis. The next Section will briefly validate the simulation model developed for the primary loop.

## 5.2. PRIMARY LOOP RESULTS

In this section, important observations made during the primary loop experiments are noted. An energy balance is performed on the primary loop. The experimental and theoretical flow rates within the primary loop are compared.

### 5.2.1. Observations

The observations made during the experiments are the same as those recorded extensively by Loubser (2014) and are thus only briefly summarised. Flashing occurred in the riser section. However, it happened in bursts with the volume of bubbles formed nearly filling the entire diameter of the riser. The bubbles would coalesce into a slug of vapour and burst through the liquid vapour interface causing geysering instability. It was difficult to control the height at which flashing occurred. It took place mainly along the length of the sight glass due to the gasket around the sight glass providing nucleation sites for bubble formation.

### 5.2.2. Energy balance

An energy account on the primary loop is presented in Figure 63a. It shows $\dot{Q}_{out}$ vs $\dot{Q}_{in}$ at the steady state condition of each of the experimental runs. All of the experiments fall within the 15% bands. The heat loss rate, $\dot{Q}_{loss,P}$, is calculated at the experimental temperatures using Equation 3.1.44. $\dot{Q}_{loss,P}$ is added to $\dot{Q}_{out}$ and plotted against $\dot{Q}_{in}$; in Figure 63b. There is a good correlation, thus, confidence is established in the expression for heat lost to the environment.

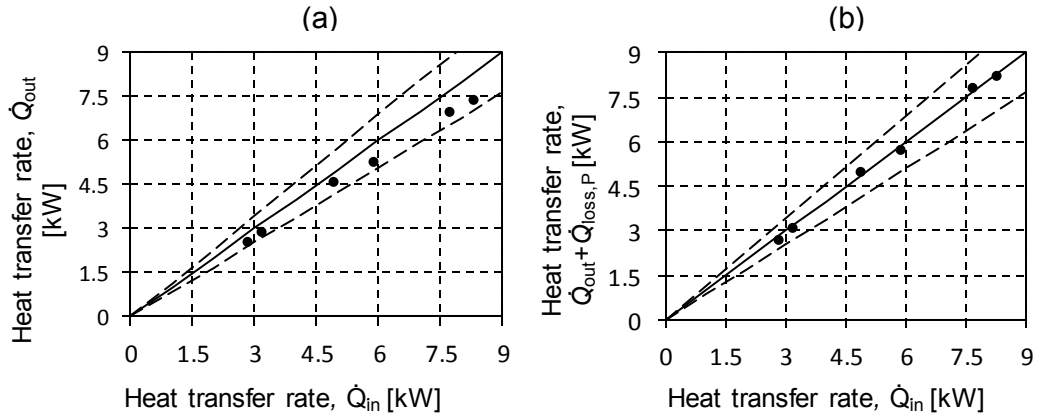


**Figure 63:** Heat transfer rate in vs. a) Heat transfer rate out b) Heat transfer rate out plus heat transfer rate lost

### 5.2.3. Mass flow rate response

The results from the primary loop experimental set-up as discussed in Section 3.1 for an input of 6.5kW to the electrical heating elements are shown in Figure 64. The experiment was run in heat pipe mode, which means that the primary loop was closed off from the expansion tank, and ran as a closed loop. There is a significant difference between the experimental and theoretical results at the start up (0 to 20 seconds). The theoretical simulation mass flow rate increases sooner than the experimental results as the heat capacity of the pipe walls are not taken into account and therefore the system responds faster.

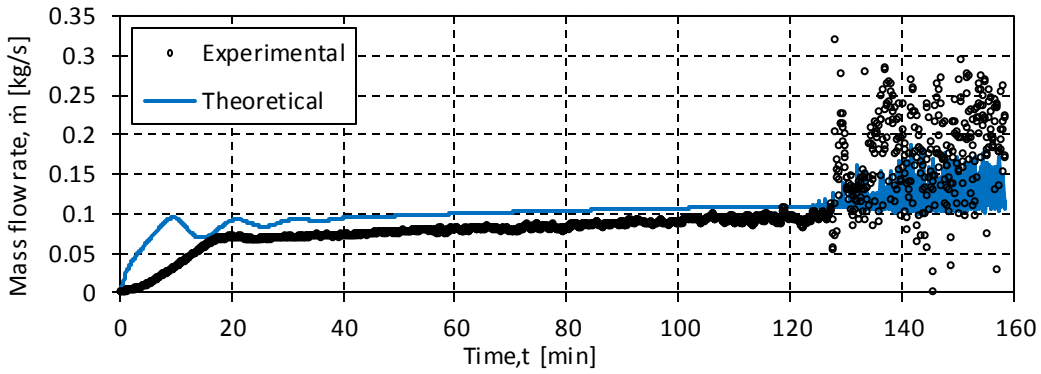


**Figure 64:** Primary loop mass flow rate response

Loubser (2014) was able to predict the behaviour of the flow before flashing but at the onset of the phase change, his homogenous numerical simulation violated the Courant-Friedrichs-Lewy (CFL) condition (Courant *et al*., 1928) and would no longer run. The use of the two-phase slip flow model developed in Section 3.1 was able to capture the flashing in the riser as shown in Figure 64.

A zoomed in section showing the levelling-off of the flow rate is given in Figure 65a. The theory over predicts the mass flow rate and has larger amplitude of oscillations than the experimental results. The onset of flashing in the riser is given in Figure 65b. The theoretical model shows spikes in flow rate upward from a value of approximately 0.11 kg/s, which under predicts the experimental results slightly.

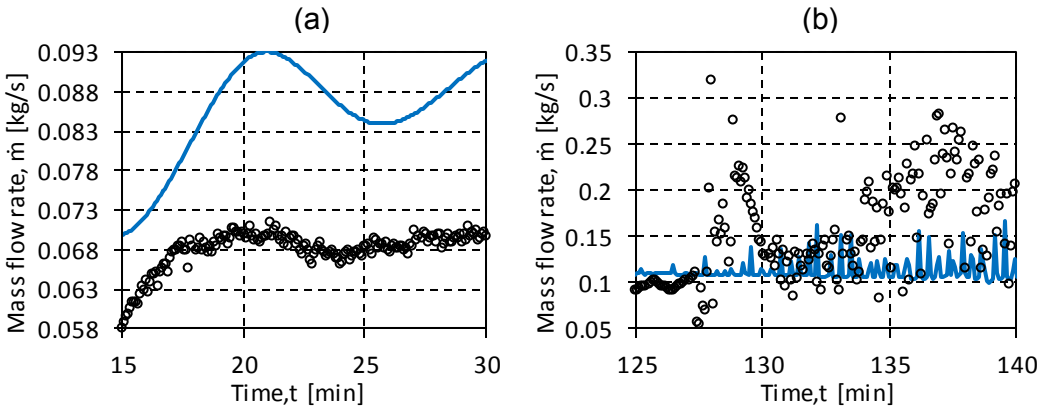


**Figure 65:** Mass flow rate zoomed to show a) flow rate levelling and b) flashing

The simulation results for the primary loop match the experimental results satisfactorily, and demonstrate the superiority of using the two-phase separated flow model over the homogenous model.

## 5.3. PASSIVE COOLING SYSTEM RESULTS

This chapter uses a steady-state implicit simulation for the entire passive cooling system to simulate combined operation of the three loops. The overall heat transfer coefficient for the secondary loop's evaporator as presented by Loubser (2014) is given in Figure 66.

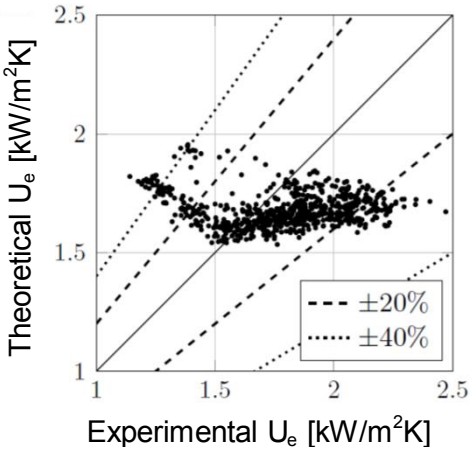


**Figure 66:** Comparison of experimental and theoretical heat transfer coefficient for the secondary loop's evaporator (adapted from Loubser, 2014)

Table 9 shows the minimum, maximum and average overall heat transfer coefficients for the evaporator and condenser. The average value for the evaporator corresponds well to the results shown in Figure 66.

**Table 9:** Overall theoretical heat transfer coefficients for the secondary loop's evaporator and condenser

| Overall heat transfer coefficient | Evaporator, $U_e$ [W/m$^2$K] | Condenser, $U_c$ [W/m$^2$K] |
|---|---|---|
| minimum | 1288.95 | 3854.99 |
| maximum | 2285.82 | 3934.99 |
| average | 1968.47 | 3904.60 |

The simulation was run for a range of $\dot{Q}_{elec}$ values. $\dot{Q}_{elec}$ was varied from 2 kW to 8 kW to ensure that the simulation does not exceed the limits of the property functions. The air temperature out, $T_{ao}$, and the mass flow of the air, $\dot{m}_a$, through the condensers are shown in Figure 67. The experimental temperatures vary around the theoretical values. Note that when the temperature is higher than predicted, the corresponding mass flow rate is lower than the predicted value. This illustrates that the system regulates itself to ensure that the heat is removed.

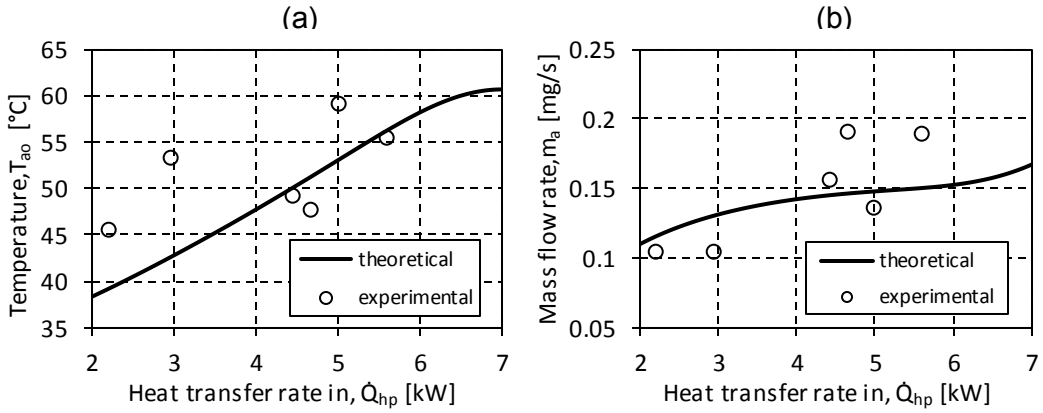


**Figure 67:** Passive cooling system a) air temperature leaving the shroud b) air mass flow rate

Figure 68a shows how the heat transferred by the secondary loop, $\dot{Q}_{hp}$, and the heat transfer rate out of the condenser, $\dot{Q}_{out}$, change with the electric power input through the electric heating elements. The heat lost from both the primary and tertiary loop are small in the beginning and increase with temperature. Approaching 8 kW, the heat loss rate from the primary loop is bigger than that of the tertiary loop due to the larger difference of temperature experienced at higher power inputs as shown in Figure 68b.

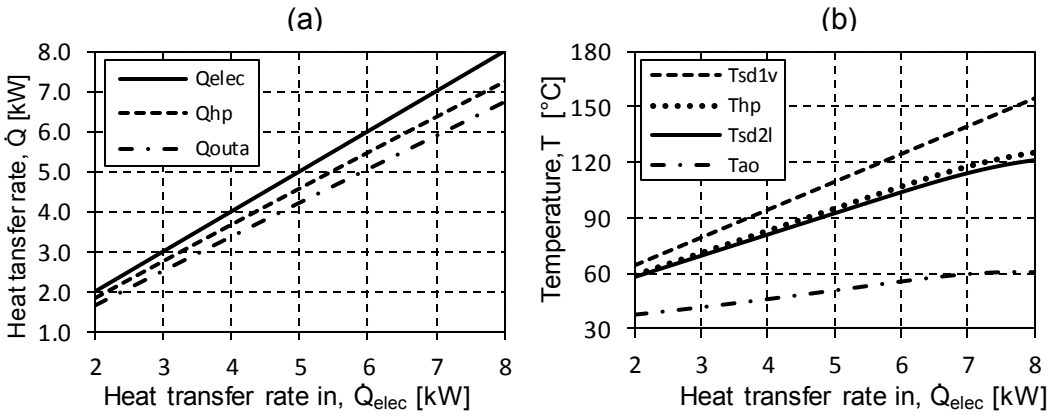


**Figure 68:** Passive cooling system a) heat transfer rate response and b) temperature response

The passive cooling system, including the primary, secondary and tertiary loops, is simulated to successfully transfer up to a heat transfer rate of 8 kW.

# 6 DISCUSSION, CONCLUSIONS AND RECOMMENDATIONS

Nuclear power sources are necessary in order to meet the electricity demands of a growing population, while limiting greenhouse-gas emissions. In an attempt to limit emissions, the South African government plans to shift the base load away from coal to nuclear power sources. This project developed an inherently safe concept with passive, transparent safety features that meet the Generation IV International Forum's objectives. This concept uses triple containment of the core TRISO® material with three integrated thermosyphon loops for a light water, 100 $MW_e$, modular nuclear reactor.

## 6.1. LITERATURE REVIEW

A literature survey was prepared to review the existing research in the relevant fields. It investigated the need for nuclear energy, analysed some of the reactors in use today and looked at how new generation nuclear reactors are incorporating natural circulation loops (NCLs). Simulations of NCLs have complex two-phase flow modelling and the different types of modelling techniques are discussed. The separated two-phase flow model is shown to be suitable for the purposes of this project. Various assumptions are necessary for successful modelling, because regenerative feedback is inherent in NCLs, where there is significant coupling between the flow and its driving force (Nayak and Vijayan, 2008). The types of instabilities expected in NCL flow are briefly covered, as well as the means with which to mitigate them, such as increasing the system pressure, lowering the heat flux and sub-cooling the return condensate.

## 6.2. EXPERIMENTAL SETUP

The tertiary loop was designed, built and commissioned, as discussed in Section 4.3, to meet objective 1. This covered the design of the secondary loop condenser, steam drum and the air-cooled condenser. The heat exchangers were designed with the objectives of using natural circulation to transfer heat at a rate of 9 kW. The secondary loop condenser is a shell and tube heat exchanger shown in Figure 29. It consists of eight 15 mm diameter pipes with a length of 0.95 m inclined at an angle of 3° and a 1 m long, 32 mm diameter return pipe. The secondary loop condenser was built with a 10% increase in the design area to accommodate sub-cooling of the return methanol condensate to improve stability of the secondary loop. Two cross-flow, steam-to-air, finned heat exchangers were commissioned. They have eight off, 1 m long finned tubes with an extra 40% heat transfer capability to ensure sub-cooling of the return condensate.

The tertiary loop was tested under low-pressure (less than 2 bar) experimental conditions to meet objective 3. The aim of the experiments was to analyse the behaviour of the thermosyphon loop and prove that the concept works. The temperature and flow rate in the tertiary loop and through the outside of the air

cooled condensers were measured. The tertiary loop functioned successfully with the average heat transfer rate out of the air-cooled condensers measured at 89.5% of the electrical power input into the system. The air temperatures along the condenser lengths in Figure 44, Figure 45 and Figure 46 show large levels of sub-cooling for power inputs ranging from 2.19 kW to 5.59 kW. The system should work effectively for higher power inputs as well, but adjustments would need to be made to the experimental setup to handle the higher pressures. The tertiary loop fulfils its desired application effectively. Being able to predict the behaviour of natural circulation loops, is imperative to their application, especially with nuclear applications.

## 6.3. RESULTS

The tertiary loop flow theory is developed as quasi-steady state, three-dimensional, separated flow in Section 3.2 to meet objective 2. A thermal-hydraulic performance numerical simulation of the tertiary loop system is built using the theory from Section 3.2, to meet objective 3. The results from the theoretical numerical simulation and the experiments are presented in Section 5.1. The temperature and mass flow rate experienced within the tertiary loop simulations match the experimental results well, with errors of 5.73% and 1.86% respectively. However, the air temperatures and air mass flow rates show larger deviation from the predicted values, with errors of 10.67% and 16.71% respectively. This highlights the sensitivity of the air-cooled condensers. The temperatures do seem to accommodate any acceleration or retardation of the mass flow rate to ensure that the heat is transferred as shown in Figure 67. The developed simulation is validated through its ability to capture the thermal-hydraulic behaviour of the tertiary loop natural circulation system. The simulation is verified through discretisation and iteration convergence and a sensitivity analysis is performed for quantification of input uncertainty.

A theoretical numerical simulation of the primary loop is developed in Section 3.1. The primary loop has flashing-driven flow and is modelled as a quasi-steady state, one-dimensional, two-phase, separated flow simulation. A simulation is developed and reflects the thermal-hydraulic behaviour of the primary loop as shown in Section 5.2 to meet objective 5. Figure 64 shows how the mass flow rate response of the primary loop theoretical model corresponds to that of the experimental results. Thus, the use of the two-phase slip flow model was able to adequately capture the flashing flow more effectively than the homogenous flow model previously used by Loubser (2014).

An implicit steady state numerical simulation model of the primary, secondary and tertiary loops operating together was developed to predict the behaviour of the complete passive cooling system and shows encouraging results, given in Figure 68. This is done in order to accomplish objective 6. The passive cooling concept can now be scaled to the dimensions of a full size, 100 $MW_e$ nuclear

reactor plant and its thermal-hydraulic behaviour confidently determined using the simulation models developed.

## 6.4. RECOMMENDATIONS

Recommendations for the continuation of this research are presented in this section. The system developed is novel and although the results were encouraging, it is recommended that the secondary loop be connected to the primary and tertiary loop and the entire passive cooling system be tested. The results from these experiments can be compared to the results of the overall passive implicit numerical simulation. This would allow confirmation of the overall heat transfer coefficient for the secondary loop's condenser and confirm that the secondary loop's heat exchangers are capable of transferring the heat as simulated.

To accommodate larger power inputs and the subsequent higher temperatures, the pressure release valve must be replaced with one that can handle higher pressures and the polycarbonate flange replaced with a stainless steel one. This would allow a larger range of results and allow for further assurance in the concept and simulation.

To improve the simulation further, the secondary loop could be modelled in more detail to fully capture the internal thermal-hydraulic behaviour, instead of the simple thermal resistance model used in this research. That is a full mass, momentum and energy conservation simulation to provide an in-depth understanding of internal operation.

The dimensions of the whole passive cooling system discussed can be scaled up to reflect the dimensions needed for this system to be applied to a full sized nuclear reactor power plant. The successful simulation model can be applied to the scaled concept to determine how a full scale model for a nuclear reactor plant would operate. This would allow prediction of its operation and material and cost estimates can then be drawn up and the economic viability of such a plant established, prior to the construction of a test reactor.

## 6.5. CLOSING STATEMENT

The development of this passive cooling system is important to the growth of local expertise and furthering the awareness of the advances being made in the safety of nuclear reactor systems. This is essential for the successful implementation of nuclear power in South Africa. The goal of an inherently safe nuclear reactor cooling and steam generation concept is viable. The theory developed was demonstrated to be sound and able to predict the operation of the concept. Recommendations are made on how to move forward in order to further this research.

# 7 REFERENCES

Barrett, A J, Marquino, W, 2013, Economic Simplified Boiling Water Reactor (ESBWR) Response To An Extended Station Blackout/Loss Of All AC Power, *Journal Of Nuclear And Related Technologies* 10, No. 2.

Beardmore, R, 2013, Roymech Mechanics: Loaded Flat Plates. Available at http://www.roymech.co.uk/Useful_Tables/Mechanics/Plates.html, [2014 June 12]

Blasius, P R H,1913, Das Aehnlichkeitsgesetz bei Rebungsvorganggen in Flussigkeiten, *Forschungsheft* 131: 1-41.

Cengel, Y A, Cimbala, J M, 2006, *Fluid Mechanics: Fundamentals and Applications*, McGraw-Hill, New York.

Cengel, Y A, Ghajar, A J, 2011, *Heat and Mass Transfer: Fundamentals and Applications*, Ed 4, McGraw-Hill, New York.

Courant, R, Friedrichs, K, Lewy, H ,1928, Über die partiellen differenzengleichungen der mathematischen physik. *Mathematische Annalen*, vol. 100, pp. 32–74.

Dobson, R T, 2016, Class notes, Mechanical and Mechatronic Department, University of Stellenbosch, Stellenbosch, South Africa.

Dobson, RT, Sittmann, I, *Use of Passive cooling systems in Generation IV nuclear reactors for core decay heat removal and containment cooling*, Mechanical and Mechatronic engineering Department, Faculty of Engineering, Stellenbosch University.

Duligal, R, 2015, *Two-phase flow simulation and characterisation in the large diameter flash tube of a natural circulation heat transfer system*, Mechanical and Mechatronic engineering Department, Faculty of Engineering, Stellenbosch University.

Fraco, A, Filippeschi, 2011, Closed Loop Two-Phase Thermosyphon of small dimensions: a Review of the experimental results, *Microgravity Science Technology* 24: 165-179.

Furuya, M, Inada, F, van der Hagen, T H J J, 2005, Flashing-induced density wave oscillations in a natural circulation BWR-mechanism of instability and stability map, *Nuclear Engineering and Design* 235: 1557-1569.

Generation IV International Forum and U.S. DOE Nuclear Energy Research Advisory Committee, 2002, *A Technology Roadmap for Generation IV Nuclear Energy systems*. Available at: https://www.gen-4.org/gif/jcms/c_40481/ technology-roadmap, [2014 July 19]

Gorenflo, D, 1993, Pool boiling, *VDI Heat Atlas*: Ha1- 25. Avaiable at: https://www.elearn.univ-ouargla.dz

Groenewald, A, 2001, *Thermal Management of Casting Moulds using Heat Pipes*, Mechanical and Mechatronic engineering Department, Faculty of Engineering, Stellenbosch University.

Hobson Technical, 2007, *Stainless Steel*, Available at: https://www.hobson.com.au [2015 July 15]

IAEA (International Atomic Energy Agency), 2015, Advanced Larger Water Cooled Reactors, A supplement to the IAEA's Advanced Reactor Information system.

IAEA, 2009, Passive Safety Systems and Natural Circulation in Water Cooled Nuclear Power Plants, IAEA-TECDOC-1624, Vienna.

Kandlikar, S G, 1999, *Handbook of phase change: Boiling and Condensation*, Taylor and Francis, Philadelphia.

Karakosta, C, Pappas, C, Marinakis, V, Psarras, J, 2013, Renewable energy and nuclear power towards sustainable development: Characteristics and prospects, Renewable and Sustainable Energy Reviews 22: 187-197.

Kirkpatrick, R D, Lockett, M J, 1974, The influence of approach velocity on bubble coalescence, *Chemical Engineering Science*, Volume 29, Issue 12, 2363-2373

Koki, H, Hitoi, O, Takashi, K, 2004, Integrated modular water reactor (IMR) design, *Nuclear Engineering and Design*, Volume 230: 253-266.

Lazarov, D , Manev, St., Ivanov, K, 1982, Oxidation of methanol on the surfaces of copper-silver alloys, *Materials Chemistry* 7.3: 331-346.

Lemmon, E W, McLinden, M O. Friend, D G, *Thermophysical Properties of Fluid Systems* in NIST Chemistry WebBook, NIST Standard Reference Database Number 69, Eds. P.J. Linstrom and W.G. Mallard, National Institute of Standards and Technology, Gaithersburg MD, 20899, http://webbook.nist.gov, [2014 November 18]

Li, C, Zhang, C, Chen, Y, Zou, J, Chen, J, 2012, The Study on Safety Goals and Public Acceptance of Nuclear Power, Asian Nuclear Prospects 2012, *Energy Procedia* 39: 415-422.

Li, C, Zhang, C, Chen, Y, Zuo, J, Chen, J, 2013, *The study on Safety Goal and Public Acceptance of Nuclear Power*, Available at www.sciencedirect.com [2014 July 24]

Loubser, K A, 2014, *An experimental study of an inherently-safe, natural circulating, flash-tube type system for a nuclear reactor steam supply concept*, Mechanical and Mechatronic engineering Department, Faculty of Engineering, Stellenbosch University.

Maizey Engineering Plastic Products, 2007, *Product Data Sheet: Polycarbonate PC1000*.

Manera, A, 2003, *Experimental and analytical investigations on flashing-induced instabilities in natural circulation two-phase systems*, PhD Thesis, Delft University of Technology, Delft, The Netherlands.

Mills, A F, Ganesan, V, 2009, Heat Transfer, Ed. 2, Pearson, India.

Mutsumi, V, Alberto, S, 2000, Carmen Project: Innovative small PWR, *Progress in Nuclear Energy*, Volume 37: 265-270.

Nuclear Energy Institute, 2016, *Nuclear Energy round the world*; Available at https://www.nei.org/Knowlege-Centre/Nuclear-Statistics/World-Statistics, [2016 July 24]

Nyak, A K, Vijayan, P K, 2008, Flow Instabilities in Boiling Two-Phase Natural Ciculation Systems: A Review, *Science and Technology of Nuclear Installations* 2008, Article 573192.

Prasad, G V D, Pandey, M, Kalra, M S, 2007, Review of research on flow instabilities in natural circulation boiling systems, *Progress in Nuclear Energy* 49: 429-451

Republic of South Africa Department of Energy, 2010, *Executive Summary of the Draft Integrated Electricity Resource Plan for South Africa - 2010 to 2030*, Available at www.doe-irp.co.za, [2015 July 07]

Rogner, H H, 2012, World outlook for nuclear power, *Energy Strategy Reviews* 1: 291-295.

Ruspini, LC, Marcel, C P, Clausse, A, 2013, Two-Phase flow instabilities: A review, *International Journal of Heat and Mass Transfer*.

Schultz, T L, 2006, Westinghouse AP1000 advanced passive plant, *Nuclear Engineering and Design* 236: 1547-1557

Seo, J T, 2013, *Small and Modular Reactor Development, Safety and Licensing in Korea*, IAEA (International Atomic Energy Agency) TWG-LWR (Technical Working Groups on Light Water Reactors).

Serth, R W, Lestina T, 2014, Process Heat transfer: Principles, Applications and Rules of Thumb, Academic Press,

Strupczewski, A, 2003, Accident risks in nuclear-power plants, *Applied Energy* 75: 79-86.

Taube, M, Lanfranchi, M, Von Weissenfluh, T H, Ligou, J, Yadigaroglu, G, Taube, P, 1986, The Inherently-Safe Power Reactor DYONISOS (DYnamic Nuclear Inherently-Safe Reactor Operating with Spheres), *Ann. Nucl. Energy* 13: 641-648

Thome, J R, 2010, *Engineering Data Book III*, Wolverine Tube Inc, Switzerland.

United States Nuclear Regulatory Commission, 2014, *Fact Sheet on dirty bombs*. Available at: www.nrc.gov, [2015 October 05]

van der Zwaan, B, 2013, The role of nuclear power in mitigating emissions from electricity generation, *Energy Strategy Reviews*(1): 296-301.

Varian Inc., 2013, *CF Flanges and Fittings*, California

Vécsey, G, Doroszlai, 1988, P G K, Geyser, A simple, new heating reactor of high inherent safety, *Nuclear Engineering and Design*: 141-145

Versteeg, H K, Malalasekera, W, 2007, *An Introduction to Computational Fluid Dynamics: The Finite Volume Method*, Ed. 2, Pearson, England.

Wahl, CVE, 2012, *Flashtube-type natural circulation system for a nuclear reactor*, Mechanical and Mechatronic engineering Department, Faculty of Engineering, Stellenbosch University.

Wallis, G. B., 1969, *One-Dimensional Two-Phase Flow*, McGraw-Hill Book Company, New York.

Weisser, D, 2007, A guide to life-cycle greenhouse gas (GHG) emissions from electric supply technologies, *Energy* 32: 1543-1559.

World Nuclear Association, 2016, Small Nuclear Power Reactors. Available at http://www.world-nuclear.org/information-library/nuclear-fuel-cycle/nuclear-power-reactors/small-nuclear-power-reactors.aspx, [2016 January 18]

Yadigaroglu, G, Lahey Jr R T, 1976, On the various forms of the conservation equations in two-phase flow, *International Journal of Multiphase Flow*(2): 477-494

Yadigaroglu, G, Zeller, M, 1994, Fluid-to-fluid scaling for a gravity- and flashing-driven natural circulation loop, *Nuclear Engineering and Design* 151: 49-64.

Zhang, D, Chong, D, Yan, J, Zhang, Y, 2012, Study on steam carrying effect in static flash evaporation, *International Journal of Heat and Mass Transfer*.

# **APPENDIX A:** PRIMARY LOOP SIMULATION ALGORITHM

This section covers the layout, dimensions and solution algorithm for the primary loop numerical simulation. The loop is discretised and the conservation equations discussed in Section 3.1 are applied to each control volume using a semi-explicit method with an upwind differencing scheme. The solution algorithm is implemented using C++ in Visual Studio and the results given in Section 5.2.

## A.1 PHYSICAL LAYOUT

The dimensions used in the simulation based on the experimental set up, with the main dimensions shown in Figure 69.

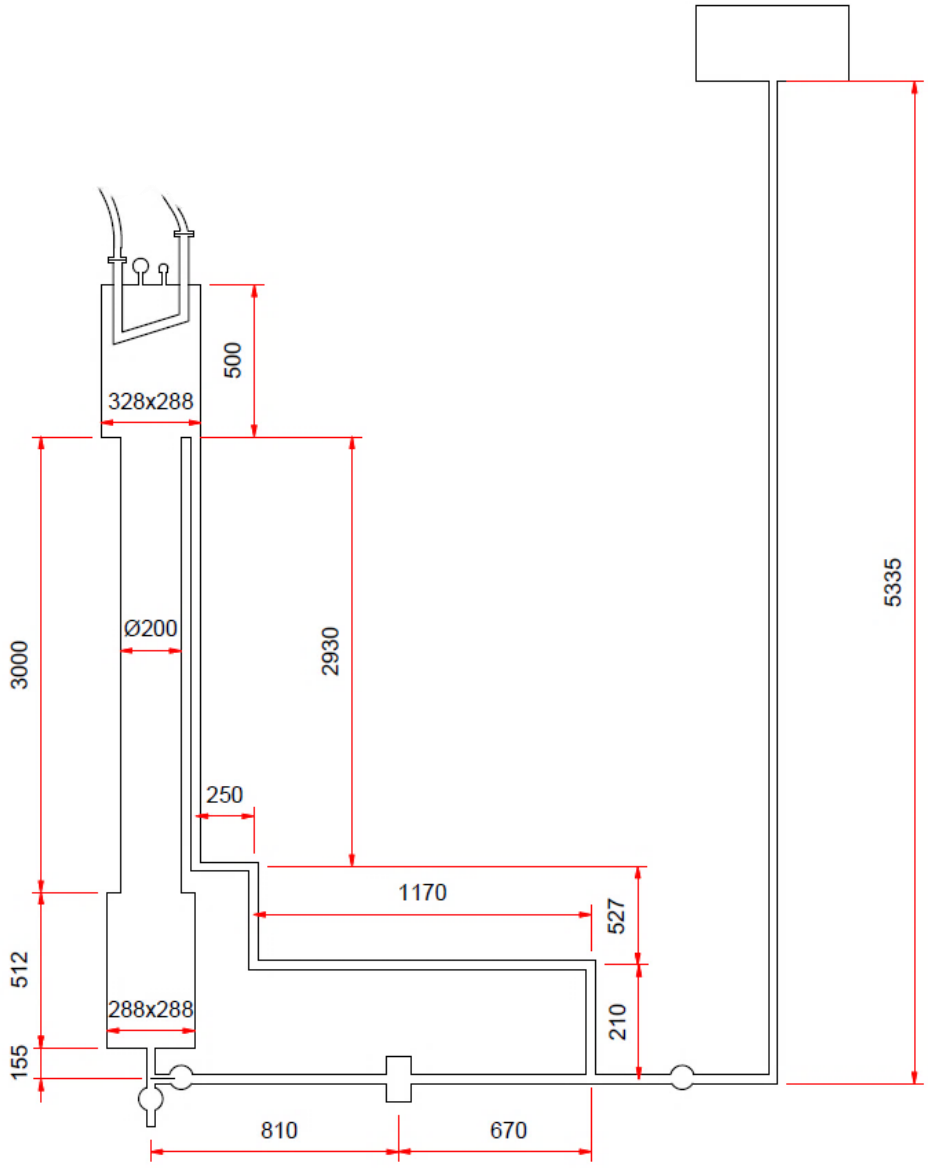


**Figure 69:** Primary loop with dimensions

The primary loop is discretised and divided into sections as shown in Figure 70. This allows for the different orientations and changes in geometry of each section to be dealt with separately.

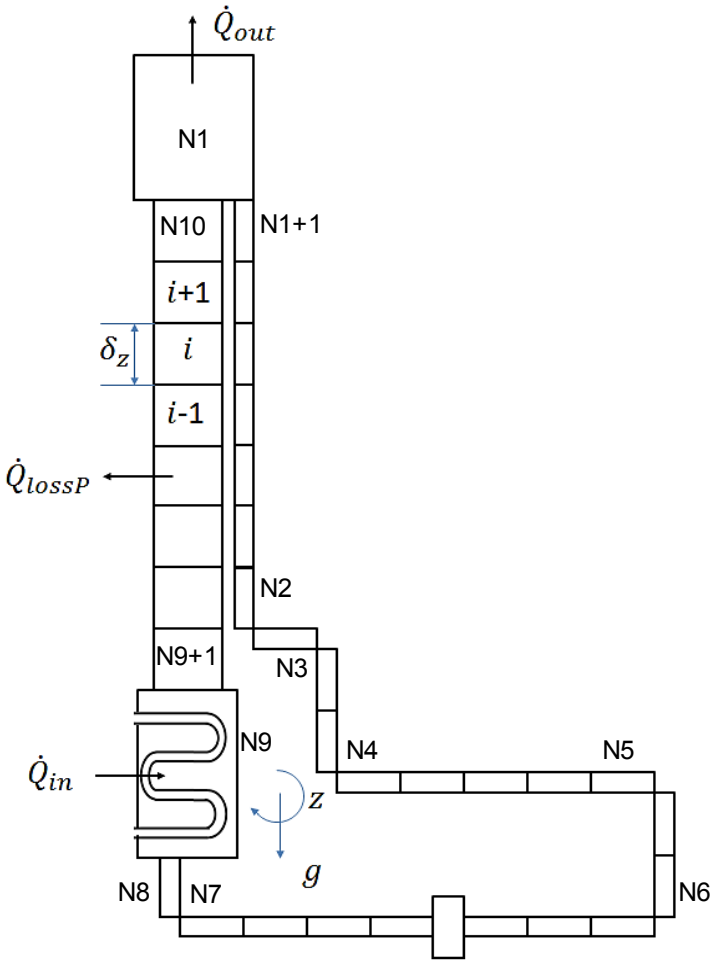


**Figure 70:** Primary loop discretisation scheme showing different zones

All the control volumes are Eularian in that they have a constant size and allow fluid to flow across their boundaries. For the numerical simulation the formula is specified spatially by $i$ and $i+1$ and in time by $t$ and $t+\Delta t$, where $\Delta t$ is the time step size.

## A.2 SOLUTION ALGORITHM

The flow chart below shows the solution algorithm for the primary loop.

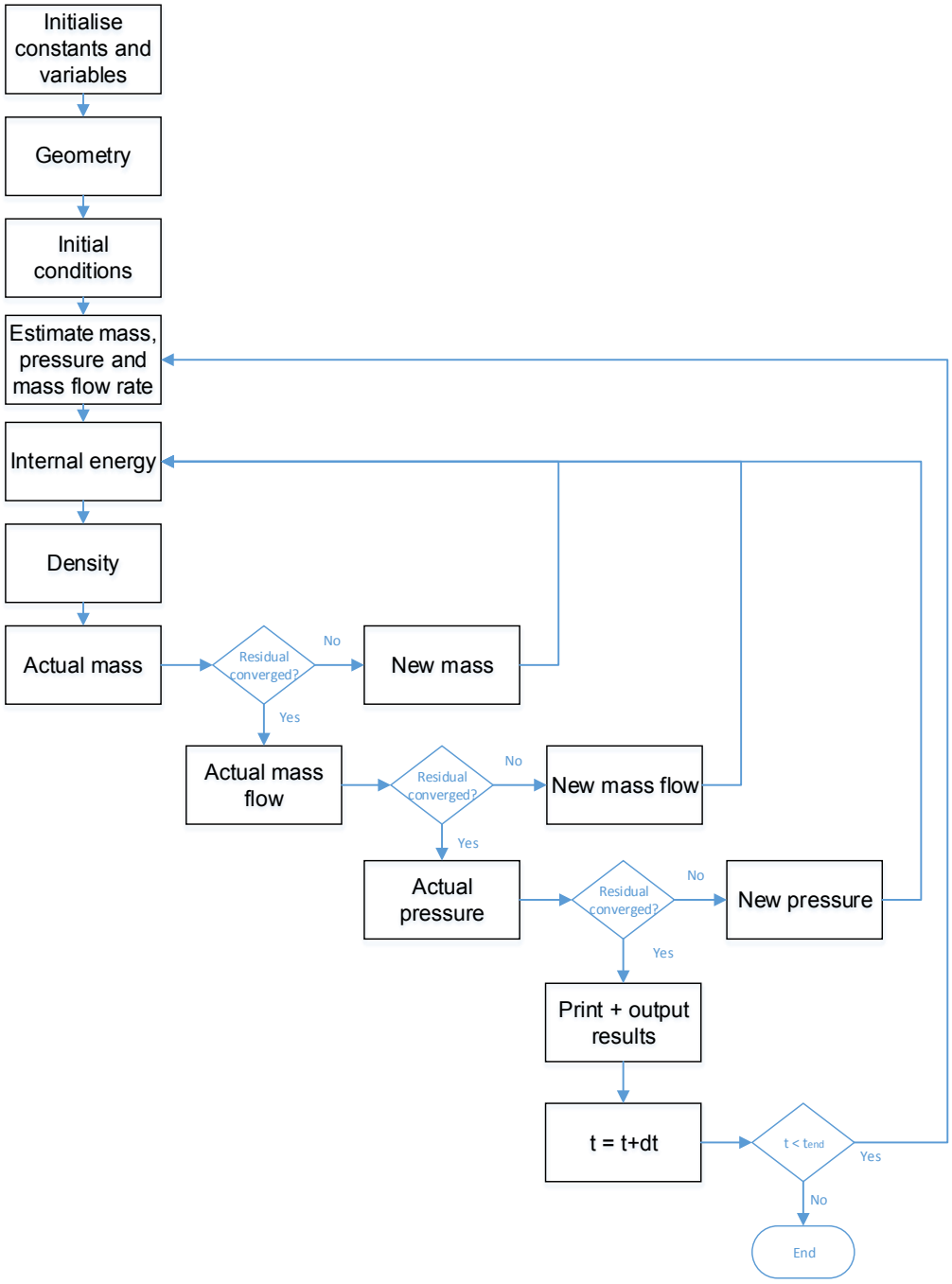


**Figure 71:** Primary loop solution algorithm

The model's inputs are the ambient conditions and the electrical power input into the resistance heating elements. The geometry of the loop and the number of control volumes will determine the size of the control volumes. The system is then set at the initial conditions chosen. The temperature in the reactor and riser

is set an 0.002 °C higher that the downcomer section. This ensures that the flow starts in the positive z-direction. The loops where there calculations are done are then entered.

Estimation of the new mass, mass flow rate and pressure is done using forecasting. The first order gradient from $t-\Delta t$ to $t$ is used to estimate the values at the new time, $t+\Delta t$.

$$m[i]^{t+\Delta t} = m[i]^{t} + \frac{dm}{dt}[i]^{t-\frac{\Delta t}{2}}\Delta t \tag{A.1}$$

The mass flow rate only needs to be determined at a single point, as it is the same throughout the system, therefore it is only calculated for the first control volume.

$$P[i]^{t+\Delta t} = P[i]^{t} + \frac{dP}{dt}[i]^{t-\frac{\Delta t}{2}}\Delta t \tag{A.2}$$

The conservation of energy equation is used to determine the internal energy at the new time step.

$$\frac{dU}{dt}[i] = \dot{m}\left(u[i]^{t} - u[i-1]^{t} + (\tau_z - P)\left(\frac{1}{\rho[i]} - \frac{1}{\rho[i-1]}\right)\right) + \dot{Q}_{elec} - \dot{Q}_{loss,P} - \dot{Q}_{ps} \tag{A.3}$$

$$u[i]^{t+\Delta t} = \frac{m[i]^{t}u[i]^{t} + \frac{dU}{dt}[i]}{m[i]^{t+\Delta t}} \tag{A.4}$$

This, along with the estimated pressure, allows the state of the fluid to be determined. Thus, the mass fraction and volume fraction can be determined.

$$x[i]^{t+\Delta t} = \frac{u[i]^{t+\Delta t} - u_f}{u_g - u_f} \tag{A.5}$$

$$\alpha[i]^{t+\Delta t} = 1 + \frac{1}{\frac{v_g}{v_l}\left(\frac{1-x[i]}{x[i]}\right)\left(\frac{\rho_g}{\rho_l}\right)} \tag{A.6}$$

Where the slip ratio, $^{v_g}/_{v_l}$, is given a constant value of 210. The density is calculated once the volume fraction is known using Equation A.7

$$\rho[i]^{t+\Delta t} = \alpha\rho_g + (1-\alpha)\rho_l \tag{A.7}$$

$$m[i]_{act}^{t+\Delta t} = \rho[i]^{t+\Delta t} \times V \tag{A.8}$$

A comparison is made between the estimated mass and the calculated mass and, once the two are sufficiently converged, the new mass is then assumed to be converged and the next step involves calculating the new mass flow rate. This requires the determination of $M[i]^{t+\Delta t}$ and $C[i]^{t+\Delta t}$.

$$M[i]^{t+\Delta t} = \frac{1}{A_x}\left[\frac{x[i]^2}{\alpha[i]\rho_g} + \frac{(1-x[i])^2}{(1-\alpha[i])\rho_l}\right] \tag{A.9}$$

$$C[i]^{t+\Delta t} = \left[\left(1 + \frac{\rho_l}{\rho_g}\frac{1-\alpha[i]}{\alpha[i]}\right)x[i]^2 + \left(1 + \frac{\rho_g}{\rho_l}\frac{\alpha[i]}{1-\alpha[i]}\right)(1-x[i])^2\right]\delta z \tag{A.10}$$

The mass flow rate is then given by:

$$\dot{m}[i]^{t+\Delta t} = \frac{\dot{m}[\iota]^t \sum_{i=1}^{Ntot} C[i]^t + \left[\dot{m}[\iota]^2 \sum_{i=1}^{Ntot} (M[i] - M[i-1]) - \sum_{i=1}^{Ntot} \tau \wp (\delta z + l_m) - \sum_{i=1}^{Ntot} \mathrm{m} g \sin\theta\right]^t}{\sum_{i=1}^{Ntot} C[i]^{t+\Delta t}} \Delta t \tag{A.11}$$

The sign of the gravity term in the above equations is accounted for by multiplying it by $\sin\theta$. $\theta$ is the angle that the control volume axis makes with the horizontal. Thus, $\theta = \pi/2$ for the riser and reactor, $\theta = -\pi/2$ for the vertical downcomer sections and $\theta = 0$ for the horizontally orientated sections of the loop. Conservation of mass is applied and the mass flow rate around the loop is applied to all the control volumes at the new time step.

$$\dot{m}[i]^{t+\Delta t} = \dot{m}[i-1]^{t+\Delta t} \tag{A.12}$$

The control volume pressure may now be determined using the conservation of momentum. The pressure in the steam drum is estimated by using a first order gradient.

$$P_{sd,v}[i] = P_{sat}(T[i]) \tag{A.13}$$

$$P_w[1] = P_{gp} + P_{sd,v}[i] + \rho_l[i] g \delta_z s dL \tag{A.14}$$

The pressures around the loop can now be calculated using

$$P_e[i] = \frac{(P[i]A)_w - \left[\frac{(\dot{m}\mathrm{C})^{t+\Delta t} - (\dot{m}\mathrm{C})^t}{\Delta t} - \left[\dot{m}^2(\mathrm{M}_w - \mathrm{M}_e)\right]^t + \tau^t \wp(\delta z + l_m) + m^t g \sin\theta\right]}{A_e} \tag{A.15}$$

$$P_w[i+1] = P_e[i] \tag{A.16}$$

Knowing the inlet and outlet pressure for the control volume using Equation A.15 and A.16, around the loop until the last control volume, N10 as shown in Figure 70, the average control volume pressure is given simply as

$$P[i] = (P_e[i] + P_w[i])/2 \tag{A.17}$$

The time is then iterated to the new time step and the loops are repeated until the end of the simulation is reached, at a time $t_{end}$.

# **APPENDIX B:** TERTIARY LOOP SIMULATION ALGORITHM

This section covers the layout, dimensions and solution algorithm for the tertiary loop. The loop is discretised into a structured mesh with quad cells. The conservation equations discussed in Section 3.2 are applied to each control volume using a semi-explicit method with an upwind differencing scheme. The solution algorithm is implemented using C++ in Visual Studio and the results given in Section 5.1.

## B.1. PHYSICAL LAYOUT

The dimensions used in the simulation based on the experimental set up, with the main dimensions shown in Figure 69.

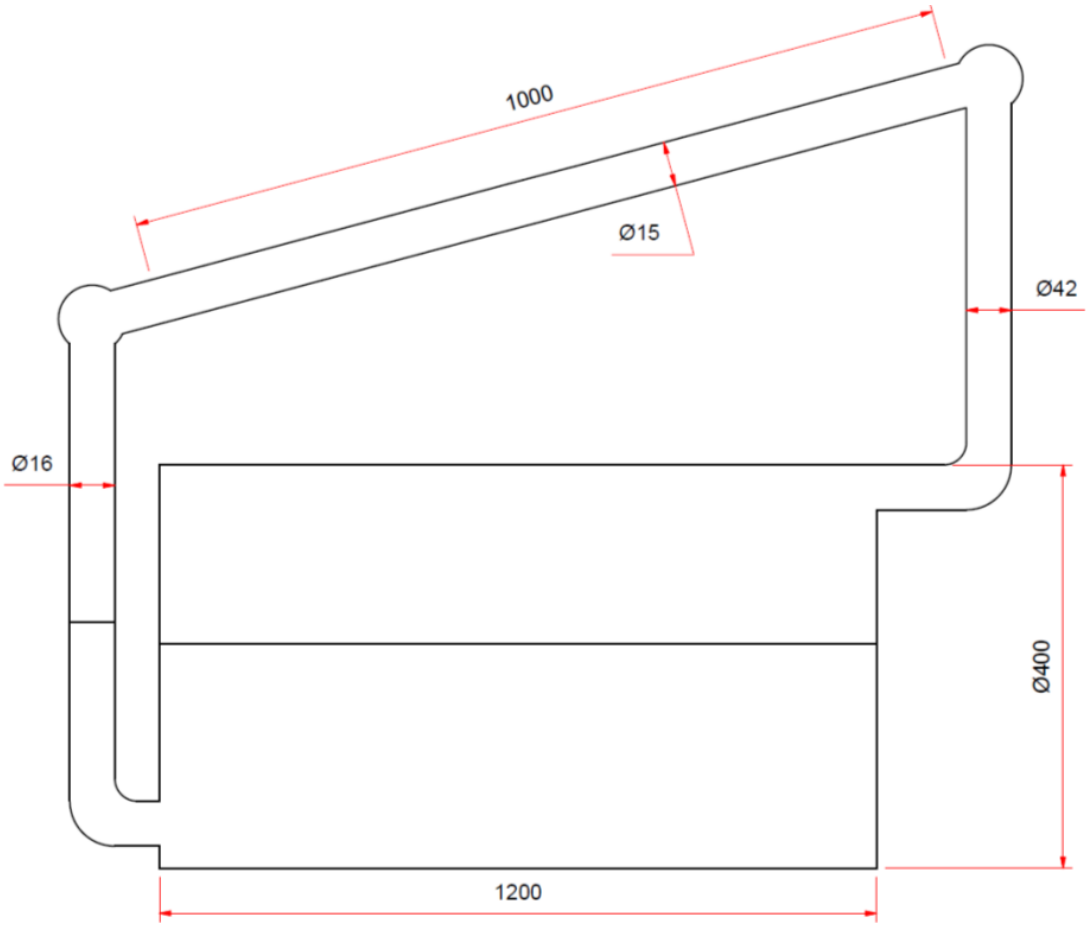


**Figure 72:** Tertiary loop with dimensions

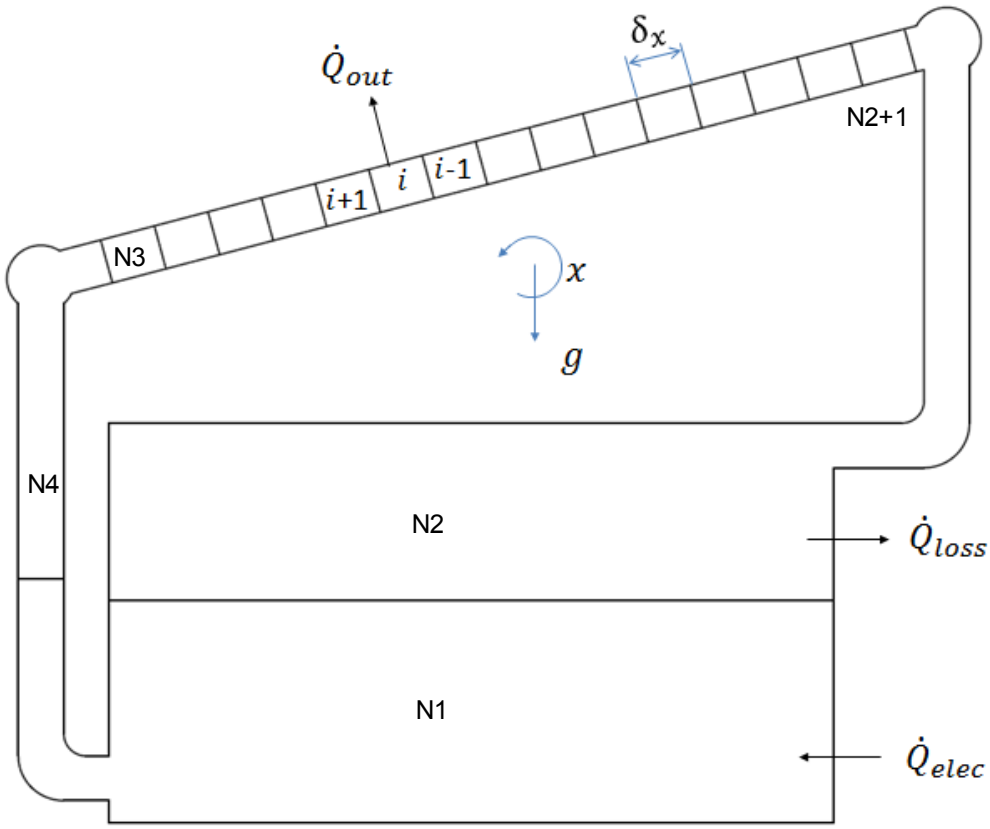


**Figure 73:** Discretised Tertiary loop

All the control volumes are Eularian in that they have a constant size and allow fluid to flow across their boundaries. For the numerical simulation the formula is specified spatially by $i$ and $i+1$ and in time by $t$ and $t+\Delta t$.

## B.2. SOLUTION ALGORITHM

The flow chart below shows the solution algorithm for the tertiary loop. The model's inputs are the ambient conditions and the electrical power input into the resistance heating elements. The geometry is input as well as the choices in control volume size to determine the number of control volumes. The size of the time step as well as the time at which the simulation must end are set. The criteria to which the mass residual must converge to are set and the calculations can be carried out for the control volumes.

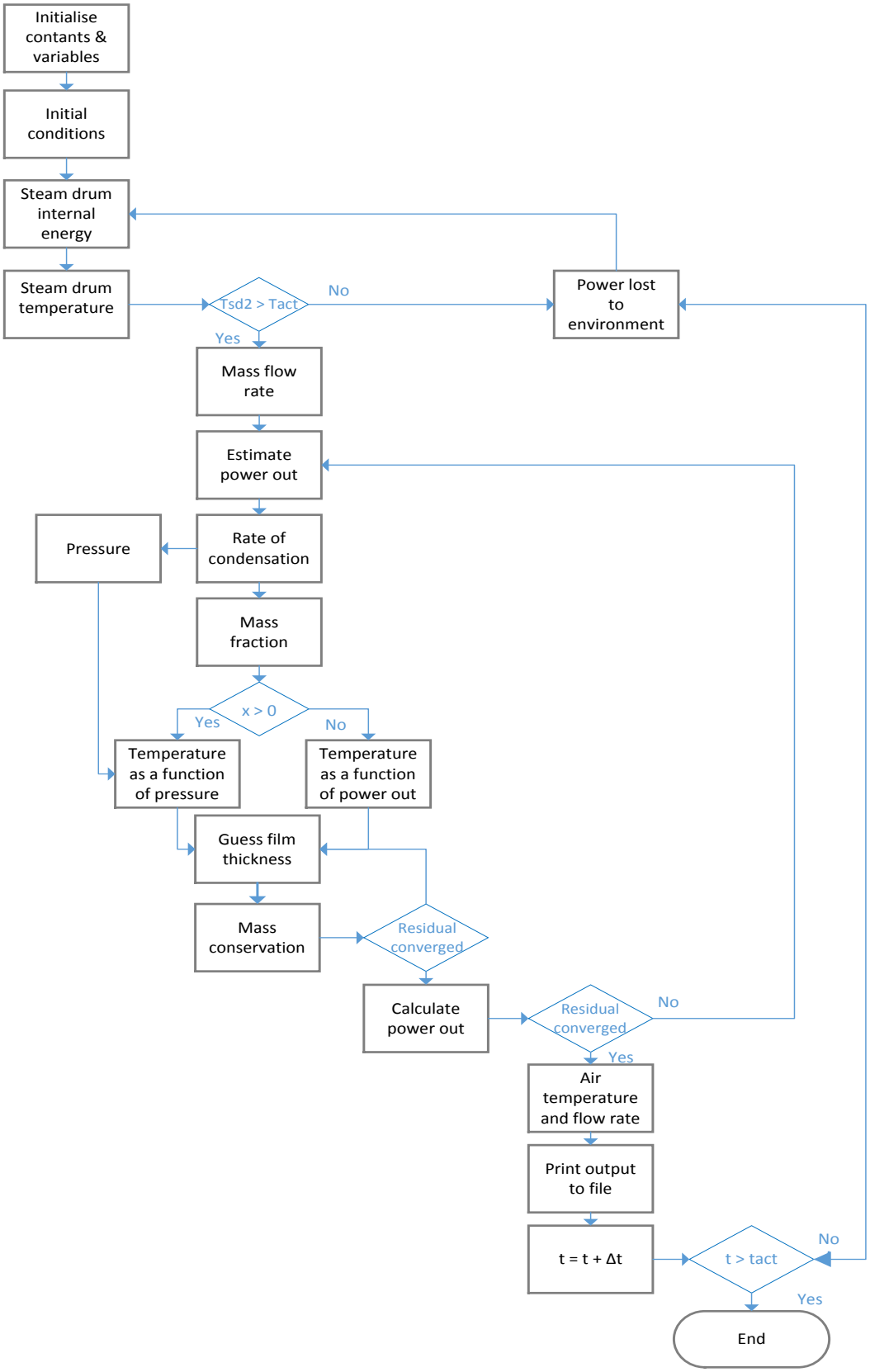


**Figure 74:** Tertiary loop solution algorithm

The internal energy of the liquid in the steam drum at the new time step is calculated based on the conservation of energy formula.

$$u^{t+\Delta t}[\mathrm{N1}] = u^{t} + \left[\dot{Q}_{elec} - \dot{Q}_{loss,T} - \dot{Q}_{out} + \dot{m}(\tau_z - P)\left(\frac{1}{\rho[N2]} - \frac{1}{\rho[N4]}\right)\right]\frac{\Delta t}{m} \tag{B.2.1}$$

From this, the temperature in the steam drum can be determined which is needed to calculate the rate of thermal energy loss from the tertiary loop.

$$T[N2]^{t+\Delta t}[= T_{sat}(u^{t+\Delta t}[\mathrm{N1}]) \tag{B.2.2}$$

$$\dot{Q}_{loss,T} = 5.06697\,(T[N2] - T_{env}) \tag{B.2.3}$$

The flow rate of steam entering the condensers is the first thing needed in the condensation model. Because the system starts at a vacuum vaporisation takes place at whatever temperature the fluid is at, at the time.

$$\dot{m} = \frac{\dot{Q}_{elec} - \dot{Q}_{loss,T} - \frac{d(mu)}{\Delta t} + \dot{m}(\tau_z - P)\left(\frac{1}{\rho[N2]} - \frac{1}{\rho[N4]}\right)}{(u[N2] - u[N4])} \tag{B.2.4}$$

The next thing to calculate is the heat transfer from the inside to the air outside of the condenser. Using the thermal resistance method, the resistances are determined as given in Equation B.5, B.6, B.10 and B.11.

$$R_{film}[i] = \frac{\delta_{film}}{k_{film} \times \pi d \delta x} \tag{B.2.5}$$

$$R_{w}[i] = \frac{t}{k_{copper} \times \pi d \delta x} \tag{B.2.6}$$

The Rayleigh number is given in terms of the fin spacing, S, as

$$Ra_s = \frac{g\beta(T_{co} - T_{env})S^3}{v^2_{air}}\,Pr \tag{B.2.7}$$

The Nusselt number is given in terms of the Rayleigh number and fin spacing as

$$Nu_s = \left[\frac{576}{\left(Ra_s S/_L\right)^2} + \frac{2.873}{\left(Ra_s S/_L\right)^{0.5}}\right]^{-0.5} \tag{B.2.8}$$

The air heat transfer coefficient based on the Nusselt number and fin spacing as

$$h_{air} = \frac{Nu_L k_{air}}{S} \tag{B.2.9}$$

$$R_{base}[i] = \frac{1}{h_{air} \times \pi d \delta x} \tag{B.2.10}$$

$$R_{fin}[i] = \frac{1}{h_{air} A_{fin}[i] \eta_{fin}} \tag{B.2.11}$$

The overall thermal resistance is calculated from Equation B.5, B.6, B.10 and B.11 as

$$R_{cond}[i] = R_{film}[i] + R_{w}[i] + \frac{1}{\frac{1}{R_{fin}[i]} + \frac{1}{R_{base}[i]}} \tag{B.2.12}$$

and is used to determine the heat transfer from each $i^{th}$ control volume

$$\dot{Q}_{cond}[i] = \frac{T[i] - T_{air}}{R_{cond[i]}} \tag{B.2.13}$$

The mass condensate formed at $i^{th}$ control volume can then be calculated

$$\dot{m}_{cond}[i] = \frac{\dot{Q}_{cond}[i]}{h_{fg}} \tag{B.2.14}$$

This allows the quality mass flow rate of the gas and hence the quality in each $i^{th}$ control volume to be determined.

$$\dot{m}_g[i] - \dot{m}_g[i-1] = -\dot{m}_{cond}[i] \tag{B.2.15}$$

$$x[i] = \frac{\dot{m}_g[i]}{\dot{m}} \tag{B.2.16}$$

$$Re = \frac{\rho_g v_g d_g}{\mu_g} \tag{B.2.17}$$

$$C_f = 16 \text{ for } Re < 1$$

$$C_f = \frac{16}{Re} \text{ for } Re < 1181$$

$$C_f = 0.0079 Re^{-0.25} \text{ for } Re > 1181 \tag{B.2.18}$$

The shear force can then be determined

$$\tau_g = C_f \frac{\rho_g {v_g}^2}{2} \tag{B.2.19}$$

And used to calculate the pressure drop along the x-direction

$$\frac{dP}{dx}[i] = \frac{\dot{m}_g[i-1]^2}{\rho_g{}^2 A_g{}^2 \delta x} - \frac{\dot{m}_g[i]^2}{\rho_g{}^2 A_g{}^2 \delta x} - \frac{\tau_g \wp_g}{A_g} \tag{B.2.20}$$

$$P[i] = P[i-1] - \frac{dP}{dx}[i] \tag{B.2.21}$$

The internal energy is then determined using

$$u[i] = u[i-1] - \frac{\dot{Q}_{cond}[i] - \dot{m}(\tau_z - P)\left(\frac{1}{\rho[i]} - \frac{1}{\rho[i-1]}\right)}{\dot{m}} \tag{B.2.22}$$

The temperature within the control volume can then be determined using $T[i] = T_{sat}(u[i])$ while bearing in mind the quality. Next, a film thickness is estimated and the heat transfer for each control volume is calculated similarly as shown in Equation B.23 to B.28.

$$R_{film}[i,j] = \frac{\delta_{film}}{k_{film} \times \delta y \delta x} \tag{B.2.23}$$

$$R_w[i,j] = \frac{t}{k_{copper} \times \delta y \delta x} \tag{B.2.24}$$

$$R_{base}[i,j] = \frac{1}{h_{air} \delta y \delta x} \tag{B.2.25}$$

$$R_{fin}[i,j] = \frac{1}{h_{air} A_{fin}[i,j] \eta_{fin}} \tag{B.2.26}$$

$$R_{cond}[i,j] = R_{film}[i,j] + R_w[i,j] + \frac{1}{\frac{1}{R_{fin}[i,j]} + \frac{1}{R_{base}[i,j]}} \quad \text{(B.2.27)}$$

$$\dot{Q}_{cond}[i,j] = \frac{T[i] - T_{air}}{R_{cond[i,j]}} \quad \text{(B.2.28)}$$

Calculate the mass condensate formed at each node along with the mass flow rate in the x- and y-directions.

$$\dot{m}_{cond}[i,j] = \frac{\dot{Q}_{cond}[i,j]}{h_{fg}} \quad \text{(B.2.29)}$$

$$\dot{m}_x[i,j] = \frac{\rho_l \delta_y}{\mu_l}\left[\frac{{\delta_z}^3}{3}\left(\rho_l g_x - \frac{dP}{dx}\right) + \frac{{\delta_z}^2}{2}\tau_{gas}\right] \quad \text{(B.2.30)}$$

$$\dot{m}_y[i,j] = \frac{{\rho_l}^2 \delta_x g_y {\delta_z}^3}{6\mu_l} \quad \text{(B.2.31)}$$

Equations B.29 to B.31 are then used to determine the residual. The film thickness is then adjusted until the value of the residual approaches zero and the solution is said to have converged on the convergence criteria analysed in Section 9.9.3.

$$Res[i,j] = \dot{m}_x[i,j] - \dot{m}_x[i-1,j] + \dot{m}_y[i,j] - \dot{m}_y[i,j-1] - \dot{m}_{cond}[i,j] \quad \text{(B.2.32)}$$

The mass flow ate and temperature of the air out of the condensers are then calculated.

$$Re_a = \frac{\rho_a v_a d_h}{\mu_a} \quad \text{(B.2.33)}$$

$$C_{fa} = 16 \text{ for } Re_a < 1$$

$$C_{fa} = \frac{16}{Re} \text{ for } Re_a < 1181$$

$$C_{fa} = 0.0079 Re^{-0.25} \text{ for } Re_a > 1181 \quad \text{(B.2.34)}$$

$$\tau_a = C_{fa}\frac{\rho_a {v_a}^2}{2} \quad \text{(B.2.35)}$$

$$\dot{m}_a = \sqrt{2\tau_a A_z A_x \left(\frac{1}{\rho_{ao}} - \frac{1}{\rho_{ai}}\right)^{-1}} \quad \text{(B.2.36)}$$

$$T_{a,o} = T_{a.i} + \frac{\dot{Q}_{cond}}{\dot{m}_a Cp_a} \quad \text{(B.2.35)}$$

The air mass flow rates and temperatures as used in the results in Section 5.1 are the volume-averaged values over the entire flow field. The time is then iterated to the new time step and the loops are repeated until the end of the simulation is reached, at a time $t_{end}$.

## B.3. BOUNDARY CONDITIONS

The boundary conditions incorporated in the simulation are as follows:

$$\dot{m}_x[0,j] = \frac{\dot{m}}{number\,of\,condenser\,tubes}$$

$$\dot{m}_y[i,0] = 0$$

$$P[1,j]^{t+\Delta t} = P_{sat}\left(u^{t+\Delta t}[1]\right)$$

$$T[1,j]^{t+\Delta t} = T_{sat}\left(P^{t+\Delta t}[1]\right)$$

# **APPENDIX C:** PROPERTY FUNCTIONS

The property functions for saturated water, methanol and air are discussed in this section. In order to simplify the functions while maintaining accuracy the data range is limited to that of the operation of the system; 0 to 120 °C. The order of polynomial chosen is based on minimising the error while ensuring that Runge's phenomenon is not introduced. Runge's phenomenon is the development of oscillations in high order polynomials. These oscillations may affect the results over certain ranges. The data used to develop the polynomial equations is taken from the NIST Standard Reference Database (Lemmon, 2014).

## C.1. PROPERTY FUNCTIONS FOR SATURATED WATER

The derivation of the polynomial equation for saturation pressure as a function of temperature was found through fitting polynomials of different orders, n, through data. An estimate of the standard deviation of the error, Δ, in predicting a future observation at X by the polynomial was calculated for each nth order polynomial using Matlab. The average (Δ/X) values are shown in Table 10.

**Table 10:** Scaled standard deviation of Saturation pressure

| n | 3 | 4 | 5 | 6 | 7 | 8 | 9 |
|---|---|---|---|---|---|---|---|
| $(\Delta/X)_{avg} \times 10^{-4}$ | 194.85 | 19.515 | 1.9716 | 3.0036 | 4.2229 | 19.862 | 58.901 |

An 5$^{th}$ order polynomial equation as chosen as it has the smallest Δ/X value. It is plotted in Figure 75 and shows a good correlation to the data.

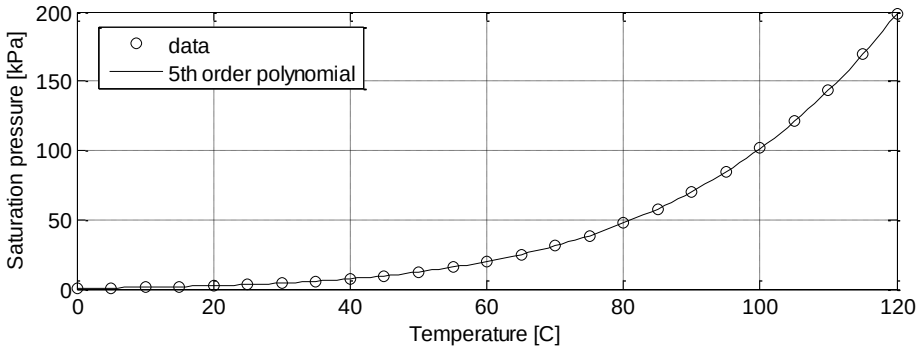


**Figure 75:** Saturation Pressure property function

Saturation pressure, $P_{sat}$

$P_1 = 2.456113471178394\text{e} - 09$
$P_2 = 3.531318320887487\text{e} - 07$
$P_3 = 2.007526194274382\text{e} - 05$
$P_4 = 1.670899551443239\text{e} - 03$
$P_5 = 4.143764697882565\text{e} - 02$
$P_6 = 6.170880479822074\text{e} - 01$

$$P_{sat} = P_1 T^5 + P_2 T^4 + P_3 T^3 + P_4 T^2 + P_5 T + P_6 \quad \text{(C.1.1)}$$

The same analysis is performed on the polynomials for the remainder of the property functions.

Liquid density

$$\rho_1 = 1.457290353608851\text{e} - 05$$
$$\rho_2 = -5.813478690556677\text{e} - 03$$
$$\rho_3 = 1.583777804889941\text{e} - 02$$
$$\rho_4 = 999.9778315212421$$
$$\rho_l = \rho_1 T^3 + \rho_2 T^2 + \rho_3 T + \rho_4 \quad \text{(C.1.2)}$$

Vapour density

$$\rho_1 = 2.808568012275708\text{e} - 17$$
$$\rho_2 = -2.770562545383586\text{e} - 14$$
$$\rho_3 = 1.543064064692267\text{e} - 11$$
$$\rho_4 = 1.469504934882544\text{e} - 09$$
$$\rho_5 = 1.834691743630455\text{e} - 07$$
$$\rho_6 = 9.991131172137864\text{e} - 06$$
$$\rho_7 = 3.357805947113105\text{e} - 04$$
$$\rho_8 = 4.850684659642411\text{e} - 03$$
$$\rho_g = \rho_1 T^7 + \rho_2 T^6 + \rho_3 T^5 + \rho_4 T^4 + \rho_5 T^3 + \rho_6 T^2 + \rho_7 \mathrm{T} + \rho_8 \quad \text{(C.1.3)}$$

Specific heat

$$Cp_1 = 2.100591458814033\text{e} - 10$$
$$Cp_2 = -9.704279018310131\text{e} - 08$$
$$Cp_3 = 1.849926857027517\text{e} - 05$$
$$Cp_4 = -1.840088561342332\text{e} - 03$$
$$Cp_5 = 1.080023048608681\text{e} - 01$$
$$Cp_6 = -3.336081551167364$$
$$Cp_7 = 4.219837565913114\text{e} + 03$$
$$Cp = Cp_1 T^6 + Cp_2 T^5 + Cp_3 T^4 + Cp_4 T^3 + Cp_5 T^2 + Cp_6 T + Cp_7 \quad \text{(C.1.4)}$$

Thermal conductivity

$$k_1 = -4.467343321157780e - 12$$
$$k_2 = 1.734946622358265e - 09$$
$$k_3 = -2.274959119938321e - 07$$
$$k_4 = 2.736119411858779e - 06$$
$$k_5 = 1.893899847699299e - 03$$
$$k_6 = 0.5610099343996854$$
$$k = k_1 T^5 + k_2 T^4 + k_3 T^3 + k_4 T^2 + k_5 T + k_6 \quad \text{(C.1.5)}$$

Prandtl number

$$Pr_1 = -3.534082826270343e-13$$
$$Pr_2 = 1.743910463148922e-10$$
$$Pr_3 = -3.611219075616487e-08$$
$$Pr_4 = 4.140733971084712e-06$$
$$Pr_5 - 2.964088673259154e-04$$
$$Pr_6 = 1.450767674549470e-02$$
$$Pr_7 = -5.242550446291073e-01$$
$$Pr_8 = 13.50131141619764$$
$$Pr = Pr_1T^7 + Pr_2T^6 + Pr_3T^5 + Pr_4T^4 + Pr_5T^3 + Pr_6T^2 + Pr_7T + Pr_8 \quad \text{(C.1.6)}$$

Surface tension

$$T_s = -2.584899360832327 \times 10^{-7}T^2 - 1.416103115635978 \times 10^{-4}T + 0.07566513097751165 \quad \text{(C.1.7)}$$

Liquid dynamic viscosity

$$\mu_{l1} = 2.716152563974858e-15$$
$$\mu_{l2} = -1.220573287820349e-12$$
$$\mu_{l3} = 2.263797680833324e-10$$
$$\mu_{l4} = -2.286476587206376e-08$$
$$\mu_{l5} = 1.425845118638751e-06$$
$$\mu_{l6} = -6.049852189337548e-05$$
$$\mu_{l7} = 1.790229415042568e-03$$
$$\mu_l = \mu_{l1}T^6 + \mu_{l2}T^5 + \mu_{l3}T^4 + \mu_{l4}T^3 + \mu_{l5}T^2 + \mu_{l6}T + \mu_{l7} \quad \text{(C.1.8)}$$

Vapour dynamic viscosity

$$\mu_{g1} = 1.138594339193785e-15$$
$$\mu_{g2} = -5.721143966819221e-13$$
$$\mu_{g3} = 1.163593974588878e-10$$
$$\mu_{g4} = 2.348100927082080e-08$$
$$\mu_{g5} = 9.215621719975428e-06$$
$$\mu_g = \mu_{g1}T^4 + \mu_{g2}T^3 + \mu_{g3}T^2 + \mu_{g4}T + \mu_{g5} \quad \text{(C.1.9)}$$

Liquid internal energy

$$u_{l1} = 3.540656953199730e-06$$
$$u_{l2} = -4.582562029878518e-04$$
$$u_{l3} = 4.200667726052153$$
$$u_{l4} = 2.173056226962013e-02$$
$$u_l = u_{l1}T^3 + u_{l2}T^2 + u_{l3}T + u_{l4} \quad \text{(C.1.10)}$$

Vapour Internal Energy

$$u_{g1} = -6.642100379485569e-06$$
$$u_{g2} = 8.496892552141312e-05$$
$$u_{g3} = 1.368428800828229$$
$$u_{g4} = 2.374946584035124e+03$$
$$u_g = u_{g1}T^3 + u_{g2}T^2 + u_{g3}T + u_{g4} \quad \text{(C.1.11)}$$

Enthalpy of vaporisation, $h_{fg}$

$$h_1 = -9.449547254526637\text{e}-09$$
$$h_2 = -1.057753480976275\text{e}-05$$
$$h_3 = 4.371605397017995\text{e}-04$$
$$h_4 = -2.373666083368314$$
$$h_5 = 2.500911674374097\text{e}+03$$
$$h_{fg} = h_1T^4 + h_2T^3 + h_3T^2 + h_4T + h_5 \quad \text{(C.1.12)}$$

## C.2. PROPERTY FUNCTIONS FOR METHANOL

The property functions for saturated methanol used in the numerical simulations are discussed in this appendix.

Liquid density is the 3rd order polynomial given in Equation C.6 and its coefficients are defined in Equation C.1 toC.5

$$\rho_1 = -9.424731020618199e-06$$
$$\rho_2 = 5.481157961654467e-04$$
$$\rho_3 = -9.482241031638675e-01$$
$$\rho_4 = 8.097514657978779e+02$$
$$\rho_l = \rho_1T^3 + \rho_2T^2 + \rho_3T + \rho_4 \quad \text{(C.2.1)}$$

Prandtl number

$$Pr_1 = 3.125000000004076e-08$$
$$Pr_2 = -9.875000000007450e-6$$
$$Pr_3 = 1.463125000000492e-03$$
$$Pr_4 = -1.356035714285853e-01$$
$$Pr_5 = 9.614785714285851$$
$$Pr = Pr_1T^4 + Pr_2T^3 + Pr_3T^2 + Pr_4T + Pr_5 \quad \text{(C.2.2)}$$

Volume expansion coefficient

$$\beta_1 = -4.629629629629438e-10$$
$$\beta_2 = 1.035714285714260e-07$$
$$\beta_3 = -2.417989417989310e-06$$
$$\beta_4 = 1.190952380952380e-03$$
$$\beta = \beta_1T^3 + \beta_2T^2 + \beta_3T + \beta_4 \quad \text{(C.2.3)}$$

### Kinematic viscosity

$$v_{l_1} = 3.125000000003515e - 15$$
$$v_{l_2} = -1.004166666667310e - 12$$
$$v_{l_3} = 1.538125000000428e - 10$$
$$v_{l_4} = -1.496369047619170e - 08$$
$$v_{l_5} = 9.881785714285839e - 07$$
$$v_l = v_{l_5}T^4 + v_{l_4}T^3 + v_{l_3}T^2 + v_{l_4}T + v_{l_5} \quad \text{(C.2.4)}$$

### Thermal conductivity

$$k_{l_1} = -1.552646949525354e - 19$$
$$k_{l_2} = -7.457142857141488e - 05$$
$$k_{l_3} = 2.002057142857140e - 01$$
$$k_l = k_{l_1}T^2 + k_{l_2}T + k_{l_3} \quad \text{(C.2.5)}$$

### Specific heat

$$C_{pl_1} = -5.466009720126957e - 06$$
$$C_{pl_2} = 3.117683013000063e - 02$$
$$C_{pl_3} = 4.616315870597821$$
$$C_{pl_4} = 2.399866510028836e + 03$$
$$C_{pl} = C_{pl_1}T^3 + C_{pl_2}T^2 + C_{pl_3}T + C_{pl_4} \quad \text{(C.2.6)}$$

### Surface tension

$$\sigma_{l_1} = -7.527082285906901e - 10$$
$$\sigma_{l_2} = 5.232266896503785e - 08$$
$$\sigma_{l_3} = -8.391051932653460e - 05$$
$$\sigma_{l_4} = 2.433684327562307e - 02$$
$$\sigma_l = \sigma_{l_1}T^3 + \sigma_{l_2}T^2 + \sigma_{l_3}T + \sigma_{l_4} \quad \text{(C.2.7)}$$

### Vapour Density

$$\rho_{g_1} = 2.330701656599282e - 08$$
$$\rho_{g_2} = -1.792071962194614e - 07$$
$$\rho_{g_3} = 1.642251374497417e - 04$$
$$\rho_{g_4} = 1.697669019365022e - 03$$
$$\rho_{g_5} = 7.338168348612466e - 02$$
$$\rho_g = \rho_{g_1}T^4 + \rho_{g_2}T^3 + \rho_{g_3}T^2 + \rho_{g_4}T + \rho_{g_5} \quad \text{(C.2.8)}$$

## C.3. PROPERTY FUNCTIONS FOR AIR

The property functions for air used in the numerical simulations are:

### Specific heat

$$Cp_1 = 7.609313596733326\text{e} - 06$$
$$Cp_2 = -9.275088252712303\text{e} - 04$$
$$Cp_3 = 4.389932294143124\text{e} - 02$$
$$Cp_4 = 1006.191707314273$$
$$Cp = Cp_1 T^3 + Cp_2 T^2 + Cp_3 T + Cp_4 \quad \text{(C.3.1)}$$

### Thermal conductivity

$$k_1 = -2.365535832499363e - 08$$
$$k_2 = 7.551497190341950e - 05$$
$$k_3 = 2.363665993345067e - 02$$
$$k = k_1 T^2 + k_2 T + k_3 \quad \text{(C.3.2)}$$

### Prandtl number

$$Pr_1 = 2.531859045308521e - 07$$
$$Pr_2 = -2.793164588880179e - 04$$
$$Pr_3 = 7.362487104346737e - 01$$
$$Pr = Pr_1 T^2 + Pr_2 T + Pr_3 \quad \text{(C.3.3)}$$

### Kinematic Viscosity

$$v_1 = 9.680428596775948e - 06$$
$$v_2 = 8.714557227564703e - 03$$
$$v_3 = 1.337954301874837$$
$$v = v_1 T^2 + v_2 T + v_3 \quad \text{(C.3.4)}$$

### Density

$$\rho_1 = -3.274786161955865e - 08$$
$$\rho_2 = 1.574787661740172e - 05$$
$$\rho_3 = -4.710802749210436e - 03$$
$$\rho_4 = 1.292111755858499$$
$$\rho = \rho_1 T^3 + \rho_2 T^2 + \rho_3 T + \rho_4 \quad \text{(C.3.5)}$$

# **APPENDIX D:** HEAT EXCHANGER DESIGN

## D.1. SECONDARY LOOP CONDENSER DESIGN

The first step in the design process was selecting the appropriate type of heat exchanger. A shell in tube heat exchanger was selected, using methanol vapour on the inside with the outside completely submerged in water.

The next step is to size the heat exchanger. To determine the heat transfer area required to transfer 9 kW, the heat transfer coefficients and temperatures at steady state conditions needed to be estimated. However, there are a number of unknowns so some assumptions must be made.

The methanol was said to boil at approximately 85 °C by Loubser (2014). The temperature of the water will vary from room temperature to that of the methanol, i.e. From 15 °C to 85 °C. The average temperature is then going to be 50 °C. It was deemed appropriate to use this in the calculations because the maximum temperature would result in an infinite heat transfer area.

Based on Franco *et al.* (2011) the minimum and maximum critical diameters are calculated using Equation D.1 and Equation D.2.

$$d_{crit,min} \cong 2\sqrt{\frac{\sigma}{g(\rho_l - \rho_g)}} = 2\sqrt{\frac{20.21}{9.81(730.133-271.5)}} = 13mm \qquad (D.1.1)$$

$$d_{crit,max} \cong 19\sqrt{\frac{\sigma}{g(\rho_l - \rho_g)}} = 19\sqrt{\frac{20.21}{9.81(730.133-271.5)}} = 127mm \qquad (D.1.2)$$

where $\sigma$ is the surface tension, $g$ is gravitational acceleration, and $\rho_l$and $\rho_g$ are the densities at saturated conditions.The inside diameter chosen was 15 mm as it is the smallest standard pipe size within the range, with a wall thickness of 2mm. This is to ensure that two-phase flow will occur. To minimize corrosion and reactivity stainless steel was selected for heat exchanger. Although copper has a higher thermal conductivity, it is known for acting as a catalyst for the oxidation of methanol (Lazarov, Manev and Ivanov, 1982).

The thermal resistance method is used to calculate the heat transfer area. The flow is assumed to be stratified, as shown in Figure 76. The heat transferred through the heat exchanger is calculated as given in Equation D.3.

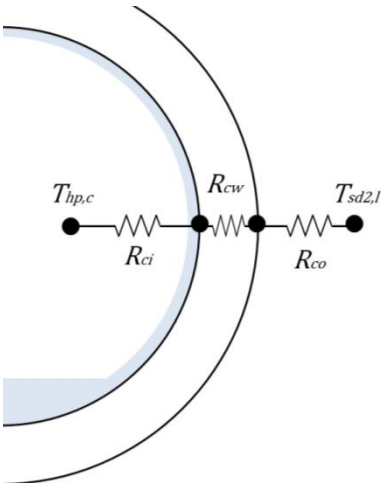


**Figure 76:** Resistance diagram for the condenser

$$\dot{Q} = \frac{T_{hp,c} - T_{sd2,l}}{R_{ci} + R_{cw} + R_{co}} \tag{D.1.3}$$

Stratified flow consists of a condensate film on the inside of the tube and a draining condensate stream collecting at the bottom of the tube, the heat transfer coefficient can be calculated using the following equation from Stephan (1992).

$$h_{ci} = 0.728x \left[ \frac{\rho_l{}^2 g h_{fg} k_l{}^3}{\mu_l (T_s - T_w)} \frac{1}{d_i} \right]^{1/4} \tag{D.1.4}$$

The fluid properties are that of methanol at a saturation temperature of 85 °C.

$$h_{ci} = 0.728 \times 1 \left[ \frac{725^2 \times 9.81 \times 1\,098\,938.826 \times 0.194^3}{25 \times 10^{-3} \times (85 - 67.5)} \frac{1}{0.015} \right]^{1/4}$$

Which gives a heat transfer coefficient of

$$h_{ci} = 3\,647.92$$

And a thermal resistance of

$$R_{ci} = \frac{1}{A_z h_{ci}} \tag{D.1.5}$$

$$R_{ci} = \frac{1}{\pi \times 0.015 \times L \times 3\,647.92}$$

The thermal resistance through the stainless steel wall is found using Equation D.6 from Cengel and Ghajar (2011).

$$R_{cw} = \frac{ln(r_o / r_i)}{2\pi L k} \tag{D.1.6}$$

$$R_{cw} = \frac{ln(15.2/15)}{2\pi \times L \times 16.6}$$

To determine the outside heat transfer coefficient the Raleigh number and Nusselt number need to be calculated. This is done using Equation D.7 and D.8 respectively from Cengel and Ghajar (2011).

$$Ra = \frac{g\beta(T_{cw} - T_{sd2,l}){d_o}^3}{v^2} Pr \quad \text{(D.1.7)}$$

$$Ra = \frac{9.81 \times 0.451 \times 10^{-3} \times (67.5 - 50) \times 0.0152^3}{5.11571 \times 10^{-7^2}} \times 4.31$$

$$Ra = 1\,038\,968$$

The Nusselt number was then found to be

$$Nu = \left\{0.6 + \frac{0.387 Ra^{1/6}}{\left[1 + (0.559/Pr)^{9/16}\right]^{8/27}}\right\}^2 \quad \text{(D.1.8)}$$

$$Nu = \left\{0.6 + \frac{0.387 \times 1\,038\,968^{1/6}}{\left[1 + (0.559/3.55)^{9/16}\right]^{8/27}}\right\}^2$$

$$Nu = 17.31074$$

From these a heat transfer coefficient and thermal resistance are determined for the outside surface of the condenser.

$$h_{co} = \frac{Nuk}{d_o} \quad \text{(D.1.9)}$$

$$h_{co} = \frac{17.31074 \times 0.644}{0.0152}$$

$$h_{co} = 733.429$$

$$R_{co} = \frac{1}{A_z h_{co}} \quad \text{(D.1.10)}$$

$$R_{co} = \frac{1}{\pi \times 0.0152 \times L \times 733.429}$$

The overall heat transfer is then calculated using Equation D.1.3 where the three thermal resistances are expressed in terms of the length of condenser, $L$.

$$\dot{Q} = \frac{T_{hp,c} - T_{sd2,l}}{R_{ci} + R_{cw} + R_{co}}$$

$$9000 = \frac{85 - 50}{\frac{1}{\pi \times 0.015 \times L \times 3\,647.92} + \frac{ln(15.2/15)}{2\pi \times L \times 16.6} + \frac{1}{\pi \times 0.0152 \times L \times 733.429}}$$

$$L = 8.87065m$$

To meet the requirement of 9 kW thermal energy transfer a length of 8.87m is needed if 15mm pipes are employed. Thus the heat transfer area necessary is 417 989 mm$^2$.

## D.2. STEAM DRUM 2 DESIGN

The maximum pressure experienced in the system is going to be 200 kPa because of the safety valve.

The axial stress at this point is determined to be

$$\sigma_a = \frac{Pr}{2t} \tag{D.2.1}$$

$$\sigma_a = \frac{200 \times 0.2}{2 \times 0.004}$$

$$\sigma_a = 5\ MPa$$

The hoop stress is determined to be

$$\sigma_h = \frac{Pr}{t} \tag{D.2.2}$$

$$\sigma_h = \frac{200 \times 0.2}{0.004}$$

$$\sigma_h = 10\ MPa$$

Budyas and Nisbitt (2008) state that the maximum normal stess that stainless steel can withstand is 276 MPa which gives a safety factor of 27.6 using the hoop stress which is higher then the axial stress. How ever to ensure that yielding will not take place in the axial direction the yield stress of the bolts is needed. Hobson Technical (2007) states that the minimum yield stress for a M14 Hex bolt made of stainless steel is 210 MPa. This gives a safety factor of 42. The transparent polycarbonate cover plate needs to also beable to withstand the pressure inside the steam drum.

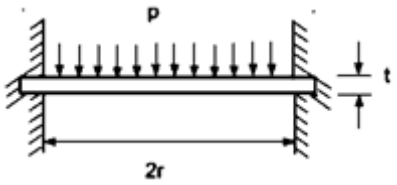


**Figure 77:** Bending stress due to pressure on a round plate with clamped edges

The maximum stress within the plate is determined using Equation D.2.3 from Beardmore (2013).

$$\sigma = \frac{3Pr^2}{4t^2} \tag{D.2.3}$$

$$\sigma = \frac{3 \times 200\,000 \times 0.2^2}{4 \times 0.012^2}$$

$$\sigma = 41.67\ \text{MPa}$$

The polycarbonate PC1000 has a yield strength of 62 MPa (Maizey, 2007) and therefor a safety factor of 1.488 and is therefore the component most likely to be damaged in the event of excessive pressure in the steam drum. This is beneficial as it is the cheapest component to replace.

## D.3. AIR-COOLED CONDENSER DESIGN

The surface temperature $T_s = 95°C$, and the fluid properties are that of air at a temperature of 60 °C. To determine the outside heat transfer coefficient the Raleigh number and Nusselt number need to be calculated. Assuming a constant heat flux over the surface of the fins, the theory from Cengel and Ghajar (2011) is used

$$Ra = \frac{g\beta(Ts-Tenv)h^3Pr}{v^2} \tag{D. 3.1}$$

$$Ra = \frac{9.81\times3.00165e-3\times(95-22)\times0.035^3\times0.7202}{1.896e-5^2}$$

$$Ra = 184642.8533$$

The optimal fin spacing can be determined from the Raleigh number as

$$s = 2.714\frac{L}{Ra_L^{0.25}} \tag{D.3.2}$$

$$s = 2.714\frac{0.035}{184642.8533^{0.25}}$$

$$s = 4.5824\,mm$$

The modified Nusselt number was then found to be

$$Nu = \left\{0.6 + \frac{0.387Ra^{1/6}}{\left[1+(0.559/Pr)^{9/16}\right]^{8/27}}\right\}^2 \tag{D.3.3}$$

$$Nu = \left\{0.6 + \frac{0.387\times184642.8533^{1/6}}{\left[1+(0.559/0.7202)^{9/16}\right]^{8/27}}\right\}^2 \tag{D.3.4}$$

$$Nu = 9.101$$

From these a heat transfer coefficient is determined for the outside surface of the condenser.

$$h_{co} = \frac{Nuk}{S} \tag{D.3.5}$$

$$h_{co} = \frac{9.101\times0.02808}{0.006}$$

$$h_{co} = 42.595$$

The heat transfer rate due to natural convection of the finned tubes of one condenser is then calculated as

$$\dot{Q} = A_z h_{co}(Ts - Tenv) \tag{D.3.6}$$

$$\dot{Q} = 2.028 \times 42.595(95 - 22)$$

$$\dot{Q} = 6305.934\ \text{W}$$

The length of the air-cooled condenser was determined by the manufacturer's specifications. The condensers were manufactured and sponsored by Colcab. Each condenser has 15 mm diameter pipes that are 1m long with 8 tubes and 4

fins per inch of tube. A fin spacing of 6 mm was the closest they could do to the calculated optimal value of 4.58 mm. Two air-cooled condensers were purchased from Colcab to ensure the system was capable of transfering the specified requirement of 9 kW. Although this is over-sized by appoximately 40%, it will have positive implications. As discussed in Section 2.5 sub-cooling of the working fluid improves the stability of natural circulation systems, thus improving the system behavior. This also allows for a larger range of operating coditions.

## D.4. FIN EFFECIENCY

The fin does not have a uniform temperature over its entire surface but the heat transfer rate is proportional to the temperature difference between the finned surface and the ambient air. Cengel and Ghajar (2011) use a fin efficiency, $\eta_{fin}$, to account for the drop in temperature in the radial direction of the fin. To determine an equivalent radius for the rectangular fin the areas are equated:

$$\pi {r_2}^2 = h_{fin} w_{fin}$$

$$r_2 = \sqrt{\frac{h_{fin} w_{fin}}{\pi}}$$

The formula for an equivalent radius is given by:

$$r_2 = \sqrt{\frac{40 \times 35}{\pi}} \tag{D.4.1}$$

$$r_2 = 21.11$$

The corrected length of the fin radius is:

$$L_c = \mathrm{L} + \frac{t}{2} \tag{D.4.2}$$

$$L_c = (r_2 - r_1) + \frac{t}{2}$$

$$L_c = (21.11 - 7.5) + \frac{0.35}{2}$$

$$L_c = 13.785$$

The corrected fin radius is:

$$r_{2c} = r_2 + \frac{t}{2} \tag{D.4.3}$$

$$r_{2c} = 21.11 + \frac{0.35}{2}$$

$$r_{2c} = 21.285$$

The area, $A_p$, as defined in Figure 78 is

$$A_p = L_c t \tag{D.4.4}$$

$$A_p = 13.785 \times 0.35$$

$$A_p = 4.825$$

The heat transfer coefficient was calculated in Appendix D.3 and the thermal conductivity is that of copper at 385 W/mK.

$$\zeta = {L_c}^{3/2}\left(\frac{h_{tco}}{k\,A_p}\right)^{1/2} \tag{D.4.5}$$

$$\zeta = 13.785^{3/2}\left(\frac{42.595}{385\times 4.825}\right)^{1/2}$$

$$\zeta = 0.245$$

The radius ratio is then calculated as:

$$\frac{r_{2c}}{r_1} = \frac{21.285}{7.5} = 2.838 \tag{D.4.6}$$

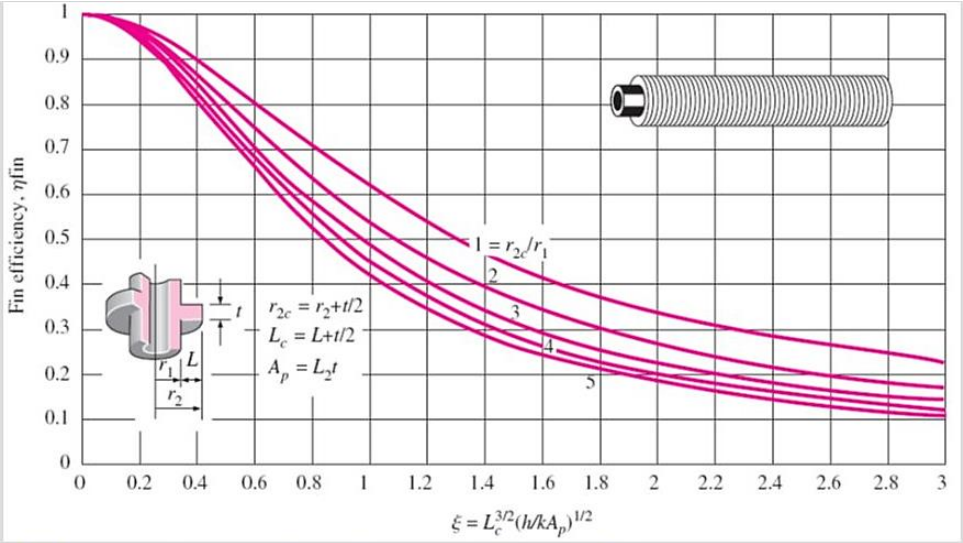


**Figure 78:** Efficiency of annular fins (Cengel and Ghajar, 2011)

The fin efficiency can be read off from the graph for the calculated values of $\zeta$ and $r_{2c}/r_1$ as 95%.

# **APPENDIX E:** THERMOCOUPLE CALIBRATION

## E.1. INSTRUMENTATION

- Fluke
- Metal equalising block with drilled thermowells
- Data Acquisition Unit
- Reference thermocouple

## E.2. METHOD

1. Place thermocouples along with reference thermocouple in Fluke
2. Ensure that they are well immersed and have good contact with the thermal source
3. Vary the temperature for the fluke from 10 °C to 120 °C in 10 °C increments and then decreasing it by 20 °C increments
4. Record the resistance of the reference thermocouple and convert it to a temperature
5. Record temperature readings for the remaining thermocouples

## E.3. RESULTS

From the measured results the errors for each thermocouple at each temperature were calculated using

$$\delta T_n = T_{ref} - T_n \tag{E.1}$$

Equations were developed for the incremental data and the decremented data. To final equations made use of the average of these two equations. The error plots for each thermocouple are presented in this section

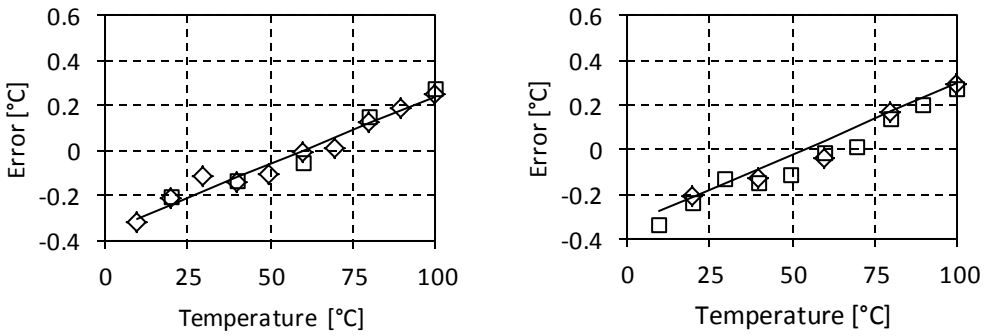


**Figure 79:** Error plots for thermocouples a) 1 and b) 2

The final equations used for thermocouples T1 and T2 are given as:

$$\delta T_1 = 0.0061T - 0.3645 \tag{E.2}$$

$$\delta T_2 = 0.00645T - 0.3411 \tag{E.3}$$

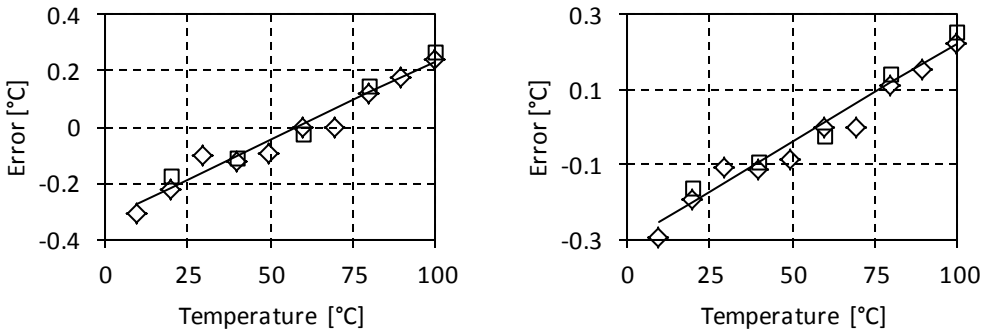


**Figure 80:** Error plots for thermocouples a) 3 and b) 4

The final equations used for thermocouples T3 and T4 are given as:

$$\delta T_3 = 0.0057T - 0.33235 \quad \text{(E.4)}$$

$$\delta T_4 = 0.00535T - 0.3082 \quad \text{(E.5)}$$

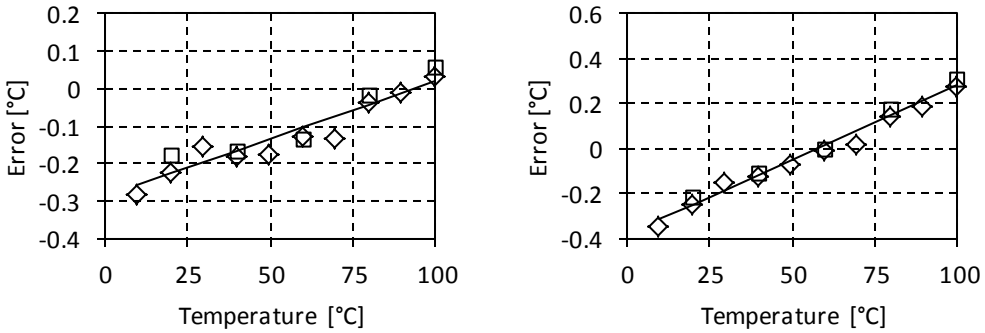


**Figure 81:** Error plots for thermocouples a) 5 and b) 6

The final equations used for thermocouples T5 and T6 are given as:

$$\delta T_5 = 0.0031T - 0.2884 \quad \text{(E.6)}$$

$$\delta T_6 = 0.0066T - 0.3785 \quad \text{(E.7)}$$

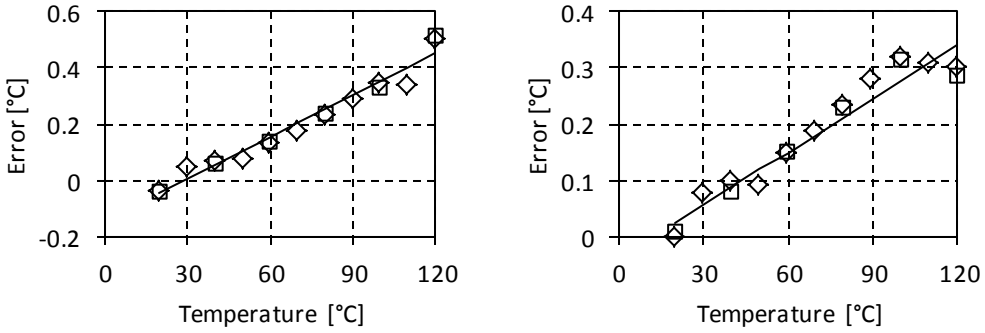


**Figure 82:** Error plots for thermocouples a) 7 and b) 8

The final equations used for thermocouples T7 and T8 are given as:

$$\delta T_7 = 0.005T - 0.14735 \quad \text{(E.8)}$$

$$\delta T_8 = 0.00315T - 0.0387 \quad \text{(E.9)}$$

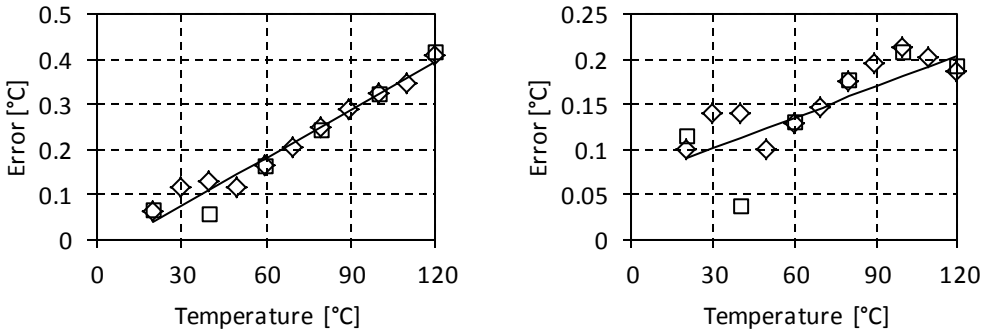


**Figure 83:** Error plots for thermocouples a) 9 and b) 10

The final equations used for thermocouples T9 and T10 are given as:

$$\delta T_9 = 0.00355T - 0.03295 \quad \text{(E.10)}$$

$$\delta T_{10} = 0.00115T - 0.06665 \quad \text{(E.11)}$$

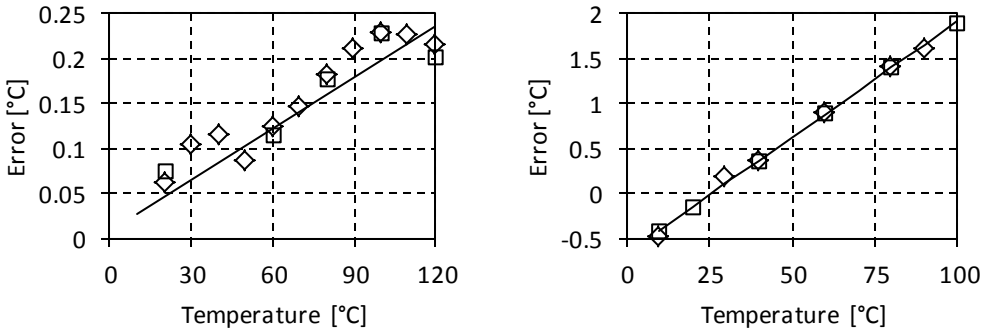


**Figure 84:** Error plots for thermocouples a) 11 and b) 12

The final equations used for thermocouples T11 and T12 are given as:

$$T_{11} = 0.0019T + 0.00825 \quad \text{(E.12)}$$

$$\delta T_{12} = 0.0258T - 0.6671 \quad \text{(E.13)}$$

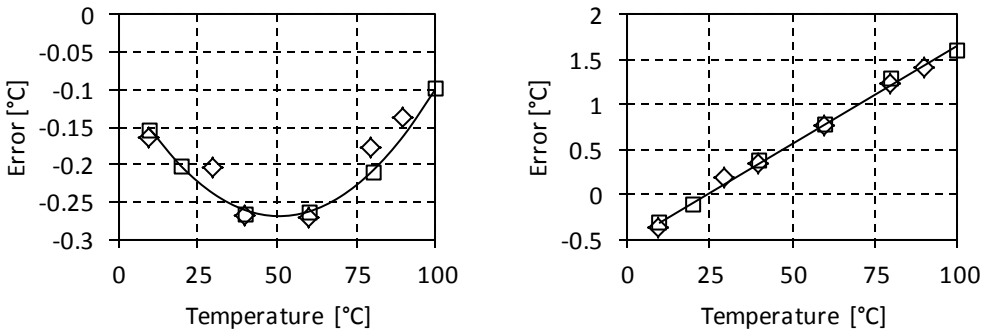


**Figure 85:** Error plots for thermocouples a) 13 and b) 14

The final equations used for thermocouples T13 and T14 are given as:

$$\delta T_{13} = 7 \times 10^{-5} T^2 - 0.0071T - 0.0888 \quad \text{(E.14)}$$

$$\delta T_{14} = 0.0219T - 0.5332 \quad \text{(E.15)}$$

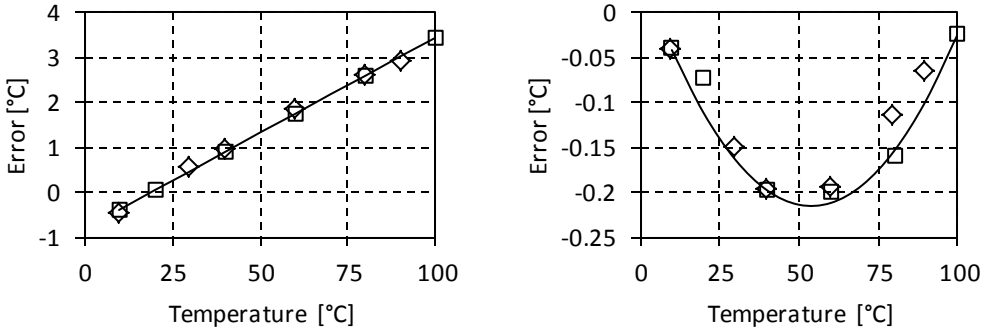


**Figure 86:** Error plots for thermocouples a) 15 and b) 16

The final equations used for thermocouples T15 and T16 are given as:

$$\delta T_{15} = 0.0425T - 0.8008 \quad \text{(E.16)}$$

$$\delta T_{16} = 9 \times 10^{-5} T^2 - 0.0097T + 0.0464 \quad \text{(E.17)}$$

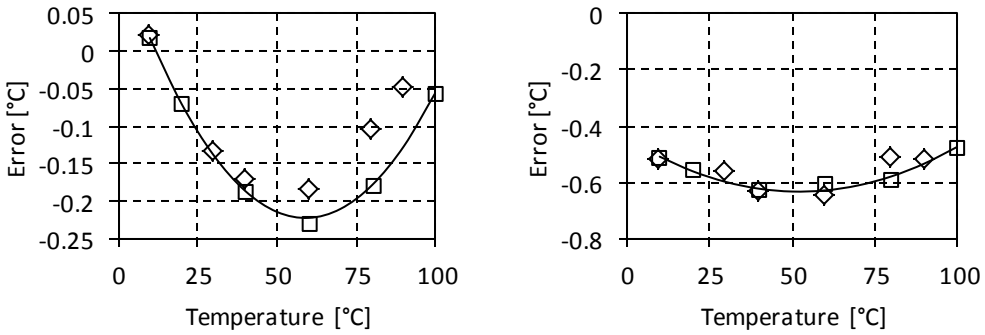


**Figure 87:** Error plots for thermocouples a) 17 and b) 18

The final equations used for thermocouples T17 and T18 are given as:

$$\delta T_{17} = 1 \times 10^{-4} T^2 - 0.0118T + 0.1255 \quad \text{(E.18)}$$

$$\delta T_{18} = 7 \times 10^{-5} T^2 - 0.0073T - 0.4429 \quad \text{(E.19)}$$

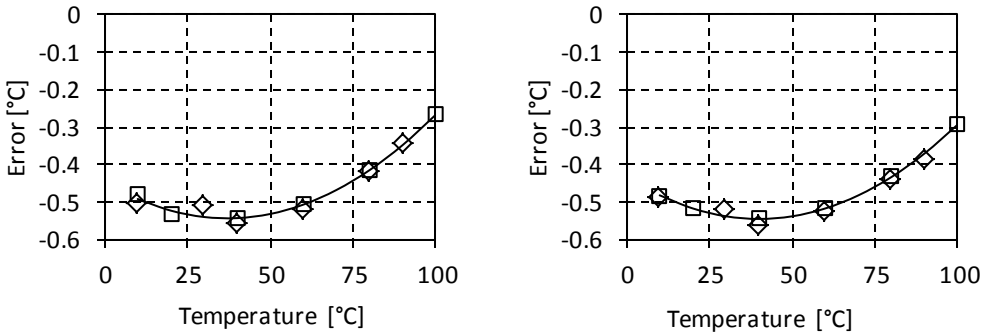


**Figure 88:** Error plots for thermocouples a) 19 and b) 20

The final equations used for thermocouples T19 and T20 are given as:

$$\delta T_{19} = 7 \times 10^{-5} T^2 - 0.0052T - 0.4469 \quad \text{(E.20)}$$

$$\delta T_{20} = 7 \times 10^{-5} T^2 - 0.0056T - 0.4331 \quad \text{(E.21)}$$

The thermocouple's discussed in this section correspond to the identified temperature measurements as shown in Table 11.

**Table 11:** Temperature measurements corresponding to thermocouples

| Thermocouple | Temperature measurement |
|---|---|
| 1 | $T_{c1i}$ |
| 2 | $T_{c2i}$ |
| 3 | $T_{c3i}$ |
| 4 | $T_{c4i}$ |
| 5 | $T_{c4o}$ |
| 6 | $T_{c3o}$ |
| 7 | $T_{c2o}$ |
| 8 | $T_{c1o}$ |
| 9 | $T_{sd2v}$ |
| 10 | $T_{sd2l}$ |
| 11 | $T_{c1a}$ |
| 12 | $T_{c2a}$ |
| 13 | $T_{c3a}$ |
| 14 | $T_{c1b}$ |
| 15 | $T_{c2b}$ |
| 16 | $T_{c3b}$ |
| 17 | $T_{ai}$ |
| 18 | $T_{ao}$ |
| 19 | $T_{sci}$ |
| 20 | $T_{sco}$ |

# **APPENDIX F:** ORIFICE FLOW METER CALIBRATION

## F.1. INSTRUMENTATION

- Constant head tank
- Pressure transducers
- Orifice plate as specified in Section 4.3.4
- Data Acquisition Unit
- Scale
- Timer

## F.2. METHOD

1. Run water through flow meter at constant flow rate using the head tank
2. Use the scale and timer to calculate the flow rate
3. Increase the flow rate and repeat 2 for seven different readings
4. Record the voltage difference measured by the data acquisition unit

## F.3. RESULTS

The mass flow rate at these conditions was converted to a volumetric flow rate using a density of 0.999001 $g/ml$. The density was evaluated at the average temperature of the tap water in the laboratory, approximately 15 $°C$. Figure 89 shows a plot of the results and from them Equation H.1 was formulated to correlate the voltage difference, $dV$, to the volumetric flow rate, $\dot{V}$.

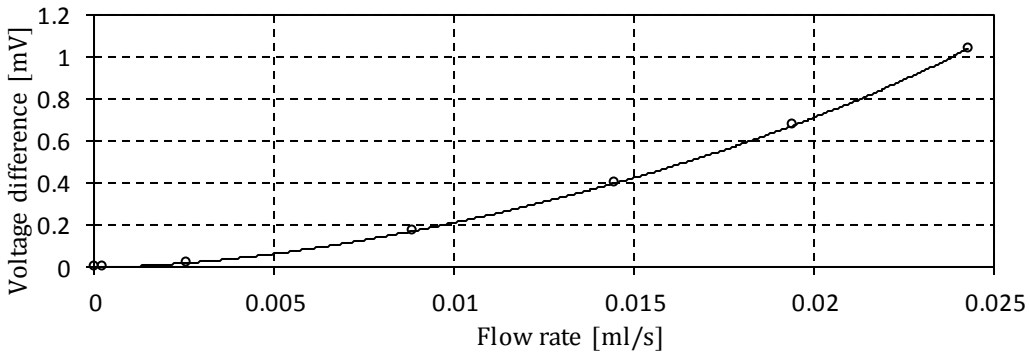


**Figure 89:** Voltage difference versus flow rate

$$dV = 1.605 \times 10^6 \dot{V}^4 - 7.086 \times 10^4 \dot{V}^3 + 2.432 \times 10^3 \dot{V}^2 + 2.421 \dot{V} \quad \text{(F.1)}$$

From Equation H.1 a set of data was developed expressing $\dot{V}$ for various values of $dV_0$. The results are plotted in Figure 90. This was done to ensure that there would be numerous data points at the lower end of the graph and the equation derived fitted these points well. Relatively low flow rates are expected so it was important that the curve be accurate at low voltages.

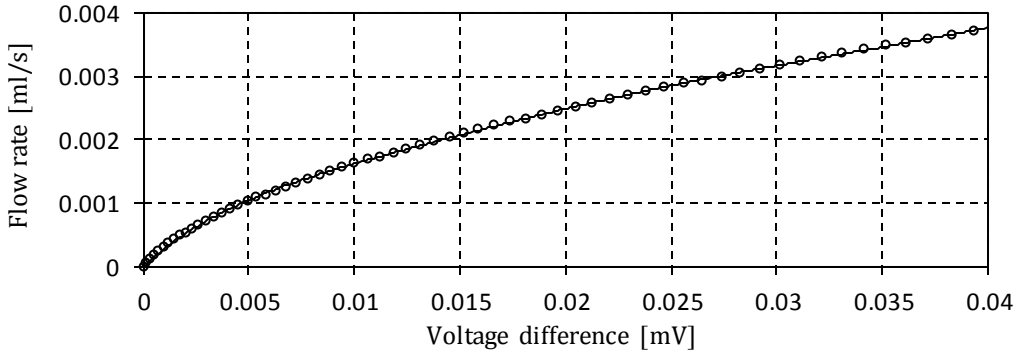


**Figure 90:** Flow rate versus voltage difference

It was found that a higher order polynomial was needed to best fit the data, especially at relatively low flow rates

$$\dot{V} = -6329370dV^6 + 939231dV^5 - 54704.8dV^4 + 1598.11dV^3 - 25.5351dV^2 + 0.303389dV \quad \text{(F.2)}$$

# **APPENDIX G:** EXPERIMENTAL PROCEDURE

Experiments were carried out on the tertiary loop as discussed in Section 4.3.

## G.1. PREPERATION

Prior to running an experiment, the following procedure must be carried out:

1. Ensure all people in the lab are wearing appropriate safety clothes. This includes closed shoes, long pants and if working below the tertiary loop a hard hat must be worn.
2. Ensure that the door and windows are open to allow ventilation and avoid the room temperature rising excessively. This further allows a means for any escaped steam to be dispersed.
3. Earth the rheostats to protect from electrical shock and ensure that they are set to zero before putting the switch on at the wall socket.
4. Ensure that a vacuum is drawn by checking that the pressure shown on the pressure gauge (PG2) matches the saturation pressure corresponding to the temperature inside the steam drum.
5. Set the thermocouple calibration corrections to the data acquisition unit and chose a sampling frequency.

## G.2. OPERATING PROCEDURE

In order to carry out an experiment the following steps must be carried out:

1. Set the computer, data logger, clip amplifiers to start recording.
2. Connect the rheostats to a power source and slowly adjust the voltage until the required power input is reached.
3. The pressure and temperature measurements are recorded by the data acquisition unit but the air flow rate needs to be recorded manually. This involves taking six measurements at the top of the shroud at the points shown in Figure 91. The hot wire anemometer must be rotated at each point until a maximum value is found. These values were recorded every 15 minutes and an average used in the calculations.

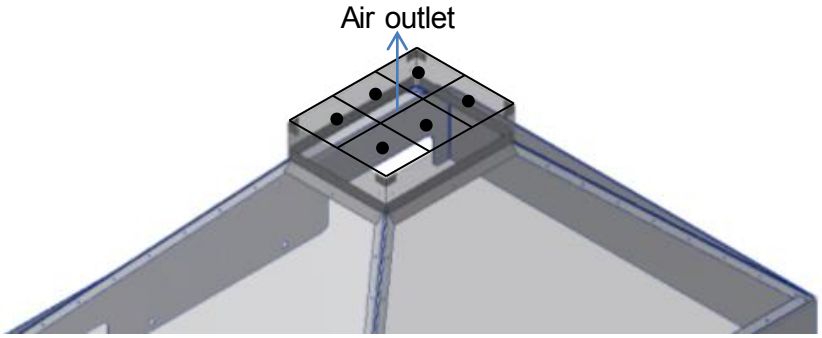


**Figure 91:** Air mass flow measurement points

4. Carefully monitor the readings measured by the data acquisition unit and when the temperatures and flow rates have levelled off sufficiently the system is assumed to have reached steady state conditions and the computer can stop recording the experiment and the data be saved. The rheostats can be set to zero and the power shut off at the wall socket.
5. The system must be monitored for at least an hour after the power is turned off to ensure that the system is cooling itself.

## G.3. EXPERIMENTS

First, the tertiary loop system was assembled on the ground and repeatability tests were run. This involved heating the system for four different power inputs, twice each. The results from these tests showed that the experiments run with the same input power gave similar results and the system was then disassembled and placed on the catwalk and stand above the primary loop where it can be connected to the remained of the passive cooling system. The system was then reassembled and tested once again. It should be noted that the experiments on the catwalk showed greater flow rates. This is probably due to the improved circulation of flow as there is sufficient space below the shroud for the air to flow freely.

The final set of experiments carried out on the tertiary loop experimental procedure is discussed in detail within Section 5.1.